FLUXES, REMINERALIZATION RATES, AND SPATIAL DISTRIBUTION OF

DISSOLVED CARBON AND NUTRIENTS IN NEARSHORE HAWAIIAN

PERMEABLE SEDIMENTS

A DISSERTATION SUBMITTED TO THE GRADUATE DIVISION OF THE
UNIVERSITY OF HAWAIʻI AT MĀNOA IN PARTIAL FULFILLMENT OF
THE REQUIREMENT FOR THE DEGREE OF

DOCTOR OF PHILOSOPHY

IN

OCEANOGRAPHY

DECEMBER 2017

By

Kristen E. Fogaren

Dissertation Committee:

Francis Sansone, Chairperson
Mark Merrifield
Brian Glazer
Eric De Carlo
Henrietta Dulai

We certify that we have read this dissertation and that, in our opinion, it is satisfactory in scope and quality as a dissertation for the degree of Doctor of Philosophy in Oceanography.

DISSERTATION COMMITTEE

_____
Chairperson

_____

_____

_____

_____

TABLE OF CONTENTS

ACKNOWLEDGEMENTS

ABSTRACT

Unlike fine-grained, diffusively dominated sediments, permeable sediments are subject to advective flows that can support high rates of organic matter remineralization through enhanced solute and particle exchange between the overlying water column and the sediment. While the importance of this enhanced exchange in marine permeable sediments has now been recognized, the effects of hydrodynamics on solute spatial distributions, sediment remineralization rates, and solute fluxes are not well constrained in these environments. This dissertation used a combination of *in-situ* experiments and modeling approaches in three studies to explore dissolved carbon, nutrient, and oxygen dynamics at three sites dominated by carbonate permeable sediments on Oahu, Hawaii.

1.) The fine-scale spatial variability of dissolved nutrients in fine-sand and coarse-sand permeable sediments was investigated using two field-based methodological approaches. These *in-situ* studies found greater spatial variability in the coarse sand than in the fine sand. Results of these experiments suggest that the dominant nutrient-regulating process in the upper sediment of the coarse sand was advective porewater circulation; however, other nutrient-regulating processes (e.g., organic matter deposition, bioturbation, oscillating redox conditions, benthic photosynthesis/respiration) control fine-scale spatial variability of nutrients in the fine sand.

2.) The rates of porewater transport in permeable sediments were estimated using transient ambient heat as a natural tracer. A statistical solution to the 1-D heat transport equation was used to estimate vertical front velocities and effective thermal diffusivities in the sediment from unfiltered temperature time-series measured using an array of buried thermistors. The method was successfully assessed using synthetic temperature datasets, freshwater streambed datasets from New York, and marine datasets from a nearshore sandy sediment in Hawaii. These

field-constrained transport rates, and data from simultaneously collected discrete porewater samples, were then used in 1-D steady-state diagenetic models to calculate depth-dependent vertical fluxes and remineralization rates for dissolved nutrients and carbon in nearshore permeable sediment environments.

3.) Results from diagenetic models indicated that dissolved nutrient and carbon distributions in the upper sediment at the fine-sand and medium-sand sites were driven by organic matter remineralization. Stochiometric models were used to investigate potential geochemical processes responsible for the alteration of porewater nutrient inventories following organic matter remineralization. These models revealed that the majority of the regenerated dissolved nitrogen at the medium-sand site is removed, likely due to denitrification. Conversely, denitrification did not appear to be a significant nutrient-regulating process at the fine-sand site. Weak or non-existent relationships between hydrodynamic parameters measured in the overlying water column and calculated porewater transport indicate that we do not fully understand the mechanisms driving advective flows in these environments.

Results in this dissertation highlight the complicated dynamics of permeable sediments in which distributions of dissolved carbon and nutrients are driven by advective flows and altered by biogeochemical processes post-remineralization. These results also suggest that these poorly understood environments may play a significant role in the coastal and global cycles of organic matter.

LIST OF TABLES

LIST OF FIGURES

Chapter 1: Introduction

1.1   Background, rationale and justification

Continental shelf ecosystems are an important component in global marine biogeochemical systems. These ecosystems are often areas of economic significance due to the diversity of flora and fauna, the abundance of fish and shellfish stocks, critical spawning habitats, tourism, and their the connection between the ocean and terrestrial, human-occupied areas (Jahnke et al. 2005a). Although ~44% of the world's continental shelves are covered by sandy, highly permeable sediment cover (Riedl et al. 1972), the role of permeable (sandy) sediments in coastal biogeochemical cycles has historically been neglected (Boudreau et al. 2001). Compounding this problem of undersampling, conventional methods for sampling fine-grained sediments (e.g., coring, porewater extraction, benthic chambers) typically either do not work in permeable sediments, disrupt the structure of sandy sediments, or interfere with the hydrodynamics that make permeable sediments so reactive (Boudreau et al. 2001; Jahnke 2004).

Permeable sediments typically have lower organic matter content than do fine-grained sediments (Meyer-Reil 1986; Boudreau et al. 2001), resulting in the misperception that permeable sediments have relatively low biogeochemical activity (Boudreau et al. 2001; Rocha 2008). However, high oxygen consumption rates in permeable sediments, coupled with low organic matter content, indicate that these sediments may be sites of high biogeochemical activity and efficient organic matter remineralization (Webb and Theodor 1968; Huettel et al. 1998a; Rocha 2008), even matching metabolic rates found in organic-rich, fine-grained sediments (Jahnke et al. 2000, 2005a).

Permeable sediments can support high metabolic rates because of enhanced fluid and particle transport between the water column and porewater, the result of several possible

1

mechanisms. First, enhanced porewater flow can result from pressure gradients created by bottom currents flowing over small topographic features such as sediment ripples, infaunal mounds, and benthic fauna (Huettel and Gust 1992; Huettel et al. 1996; Boudreau et al. 2001). Second, surface gravity waves are important drivers of enhanced transport in permeable sediments in wave-impacted environments (Falter and Sansone 2000a). As surface gravity waves pass over permeable sediment, they cause a dynamic pressure field that can induce porewater movement and thereby impact chemical zonation in sands (Boudreau et al. 2001). Also, enhanced porewater flow can force degradable particles like bacteria, algae, diatoms and detritus into the sediment where they can be retained (Huettel et al. 1996; Huettel and Rusch 2000a), thereby increasing the transfer rate of particulate matter across the sediment-water interface (SWI). Furthermore, enhanced porewater flow can result in particles penetrating deeper into the sediment than would typically be expected through simple gravitational settling (Huettel et al. 1996). For example, Rusch and Huettel (2000) demonstrated that bottom currents can physically force diatoms 2-3 cm into a permeable sediment. Dissolved oxygen (DO) and other electron acceptors are also flushed through the sediments, enhancing particle decay and resulting in the high metabolic rates found in permeable sediments (Boudreau et al. 2001).

Flume experiments designed to mimic the hydrodynamic conditions and enhanced porewater flows of permeable sediment environments have demonstrated strong sediment spatial patterns in porewater nutrient and DO concentrations when water flows over permeable sediment ripples: lower nutrient and higher DO concentrations are systematically found under ripple troughs, while higher nutrient and lower DO concentrations are observed under ripple crests (Precht et al. 2004; Huettel et al. 2014). This has been attributed to physically induced porewater circulation and particulate deposition in the upper sediment, with overlying bottom water and its

associated particles preferentially entering at ripple troughs, and porewater constituents undergoing remineralization before the porewater exits at ripple crests.

The remineralization end products from the recycling of organic matter in permeable sediments can thus be transferred to the overlying water column at greater rates than in fine-grained sediments (Huettel et al. 1998a). In oligotrophic waters, inorganic nutrients produced by remineralization within sediments may be an important source of nutrients to the water column. For example, in a year-long study of coral reefs on the southern shore of Oahu, Hawaii, water-column concentrations of dissolved nitrate and ammonium were seen to increase during three ocean swell events (Grigg 1995), the latter arguably from increasing sedimentary nutrient fluxes. Therefore, the connection between sediment organic matter remineralization and inorganic nutrient production, resulting in water-column productivity, may be of enhanced importance in coastal systems with permeable sediments, and may be regulated by physical forcing. It is this interplay of physics, geochemistry, and biology that is the focus of this dissertation.

1.2   Field Sites

Field experiments were conducted at three different sites on Oahu, Hawaii, which are dominated by permeable carbonate sediments (Figure 1.1, Table 1.1). Carbonate sands, like those at the study sites, are commonly found globally in tropical and subtropical regions, and cover ~10% of continental shelves worldwide (Rasheed et al. 2004). The selected sites were chosen to cover a range of natural sediment permeabilities. Coastal Hawaii regularly experiences enhanced surface wave conditions (swells) from various directions that are generally well predicted by local meteorologists and water-sport enthusiasts, which enables advance planning of sampling operations that target specific hydrodynamic conditions. Therefore, Oahu is an excellent place to study wave-influenced permeable sediments.

The Fine Site is located ~115 m from shore at Makai Research Pier (MRP), in a back-reef lagoon on the eastern shore of Oahu at a water depth of 3.1 m. The east side of Oahu is exposed to ocean swells generated from the northeasterly Trade Winds. These swells persist most of the year and have typical wave heights of 0.3-1.3 m, with periods of 5-8 s (Fletcher et al. 2002). Because the back-reef lagoon is sheltered from the majority of the wave energy, sediment at MRP consists of very fine to fine sand.

Located in Mamala Bay on the south shore of Oahu, the Medium Site is located at the Kilo Nalu Nearshore Reef Observatory (Kilo Nalu, KN) ~385 m offshore at a water depth of ~12 m. Trade wind swell, because it can wrap around the southern flank of Diamond Head and impact the south shore of Oahu, is also common at the Medium Site. The Medium Site is also impacted by southern swells that are generated in the southern hemisphere by austral winter storms (Fletcher et al. 2002; Fogaren et al. 2013). The southern swell typically occurs from April to October, and results in waves of 0.3-1.2 m in height with 14- to 22-s periods (Moberly and Chamberlain 1964; Fletcher et al. 2002). The sediment at Kilo Nalu is characterized as a fine to medium well-sorted sand.

The Coarse Site is located off the south shore of Oahu in the Kapua Channel, a small channel in the reef used by swimmers and human-powered watercraft. This site is ~110 m from shore at a water depth of 3.0 m. Like the Medium Site, the Coarse Site is also subject to southern swells, but given the more energetic conditions at this shallower site, the sediment is dominated by coarse to very coarse sand.

1.3   Dissertation Objectives

There is a global need to quantify the role of permeable sediments in nearshore nutrient budgets. Thus, this dissertation uses a combination of *in-situ* experiments and modeling exercises

to explore carbon, nutrient and DO dynamics in nearshore permeable sediments. I first investigated the fine-scale spatial distribution of DO and nutrients in rippled sediments. I also developed a relatively non-invasive technique to estimate *in-situ* porewater transport rates, and used these *in-situ* porewater transport rates to constrain diagenetic models that allowed me to estimate nutrient and carbon porewater fluxes and depth-dependent remineralization rates. Although these studies focus on carbonate reef sediments in Hawaiian waters, the field and modeling techniques can be applied to all permeable sediments.

The main goals of my research were:

1) To evaluate the degree of fine-scale nutrient variability in rippled permeable sediments, and to determine if spatial nutrient distributions in sand ripples measured in the field follow similar patterns to those observed in laboratory flume studies;

2) To develop a method for estimating porewater transport rates in marine environments using temperature time-series data from an array of buried thermistors; and,

3) To compare nutrient fluxes and remineralization rates at two sites characterized by permeable sediments.

These research goals are addressed in Chapters 2-4 of this dissertation. In Chapter 2, two approaches are used at the Fine and Coarse Sites to examine the *in-situ* spatial variability of dissolved nutrients in permeable sediments. The results show significant spatial variability in dissolved nutrient concentrations in both sediments, with less variation in the fine-sand sediment. The fine-scale structure of dissolved nutrients across sand ripples at the two sites is then used to highlight nutrient-regulating process in the two sediments.

5

In Chapter 3, a novel technique is developed that uses a statistical solution to the one-dimensional heat transport equation to estimate values for vertical thermal front velocity and effective thermal diffusivity using unfiltered temperature time-series from an array of buried thermistors. Vertical porewater velocities are then obtained after applying known sediment thermal parameters. The method is assessed statistically, comparatively, and theoretically using streambed and nearshore permeable sediment temperature profiles.

In Chapter 4, field-constrained porewater transport rates are used with discrete porewater samples to estimate nutrient and carbon fluxes at the Fine and Medium Sites. Multidimensional porewater flows are simplified in a one-dimensional diagenetic model using enhanced diffusion coefficients. Depth-dependent remineralization rates are then estimated using inverse porewater models.

A summary is provided of my dissertation findings in Chapter 5. Results highlight the complexities of permeable sediment environments, and emphasize the strength of a multi-faceted research approach that combines field-based measurements and diagenetic modeling. Lastly, statistics for the crest-trough ripple experiments in Chapter 2 can be found in Appendix A, while the freshwater data sets used in the validation of our model in Chapter 3 can be found in Appendix B.

1.4   References

Boudreau, B. P., M. Huettel, S. Forster, and others. 2001. Permeable marine sediments: Overturning an old paradigm. Eos (Washington. DC). **82**: 133–136. doi:10.1029/EO082i011p00133-01

Falter, J. L., and F. J. Sansone. 2000. Hydraulic control of pore water geochemistry within the oxic-suboxic zone of a permeable sediment. Limnol. Oceanogr. **45**: 550–557.

Fletcher, C. H., E. E. Grossman, B. M. Richmond, and A. E. Gibbs. 2002. Atlas of Natural Hazards in the Hawaii Coastal Zone. I-2761. U.S. Geological Survey.

Fogaren, K. E., F. J. Sansone, and E. H. De Carlo. 2013. Porewater temporal variability in a wave-impacted permeable nearshore sediment. Mar. Chem. **149**: 74–84. doi:10.1016/j.marchem.2012.12.005

Grigg, R. W. 1995. Coral reefs in an urban embayment in Hawaii: a complex case history controlled by natural and anthropogenic stress. Coral Reefs **14**: 253–266.

Huettel, M., P. Berg, and J. E. Kostka. 2014. Benthic exchange and biogeochemical cycling in permeable sediments. Ann. Rev. Mar. Sci. **6**: 23–51. doi:10.1146/annurev-marine-051413-012706

Huettel, M., and G. Gust. 1992. Impact of bioroughness on interfacial solute exchange in permeable sediments. Mar. Ecol. Prog. Ser. **89**: 253–267. doi:10.3354/meps089253

Huettel, M., and A. Rusch. 2000. Transport and degradation of phytoplankton in permeable sediment. Limnol. Oceanogr. **45**: 534–549.

Huettel, M., W. Ziebis, S. Forester, and G. W. Luther III. 1998. Advective transport affecting metal and nutrient distributions and interfacial fluxes in permeable sediments. Geochim. Cosmochim. Acta **62**: 613–631.

Huettel, M., W. Ziebis, and S. Forster. 1996. Flow-induced uptake of particulate matter in permeable sediments. Limnol. Oceanogr. **41**: 309–322.

Jahnke, R. A. A. 2004. Transport processes and organic matter in coastal sediments, p. 163–192. *In* A.R. Robinson and K. Brink [eds.], The Sea, Volume 13: The Global Coastal Ocean. Harvard University Press.

Jahnke, R. A. A., J. Nelson, R. L. Marinelli, and J. E. Eckman. 2000. Benthic flux of biogenic elements on the Southeastern US continental shelf: influence of pore water advective transport and benthic microalgae. Cont. Shelf Res. **20**: 109–127.

Jahnke, R. A. R., M. Richards, J. Nelson, C. Robertson, A. Rao, and D. Jahnke. 2005. Organic matter remineralization and porewater exchange rates in permeable South Atlantic Bight continental shelf sediments. Cont. Shelf Res. **25**: 1433–1453. doi:10.1016/j.csr.2005.04.002

Meyer-Reil, L. A. 1986. Spatial and temporal distribution of bacterial populations in marine shallow water surface sediments , p. 141–160. *In* P. Lasserre and J.M. Martin [eds.], Biogeochemical processes at the land-sea boundry. Elsevier/North-Holland Publishing Co.

Moberly, R. J., and T. Chamberlain. 1964. Hawaiian beach systems. Hawaii Inst. Geophys. Rep. HIG **64**.

Precht, E., U. Franke, L. Polerecky, and M. Huettel. 2004. Oxygen dynamics in permeable sediments with wave-driven pore water exchange. Limnol. Oceanogr. **49**: 693–705. doi:10.4319/lo.2004.49.3.0693

Rasheed, M., C. Wild, U. Franke, and M. Huettel. 2004. Benthic photosynthesis and oxygen consumption in permeable carbonate sediments at Heron Island, Great Barrier Reef, Australia. Estuar. Coast. Shelf Sci. **59**: 139–150. doi:10.1016/j.ecss.2003.08.013

Riedl, R. J., N. Huang, and R. Maohan. 1972. The subtidal pump: a mechanism of interstitial water exchange by wave action. Mar. Biol. **13**: 210–221.

Rocha, C. 2008. Sandy sediments as active biogeochemical reactors: compound cycling in the fast lane. Aquat. Microb. Ecol. **53**: 119–127.

Rusch, and M. Huettel. 2000. Advective particle transport into permeable sediments--evidence from experiments in an intertidal sandflat. Limnol. Oceanogr. **45**: 523–533.

Webb, J. E., and J. Theodor. 1968. Irrigation of submerged marine sands through wave action. Nature **220**: 682–683.

Table 1.1: Summary of water-column and sediment characteristics for study sites.

	PARAMETER	STUDY SITE		
		Fine Site	Medium Site	Coarse Site
	Location	Makai Research Pier	Kilo Nalu Observatory	Kapua Channel
	Latitude	21°19'9.16" N	21°17'18.96" N	21°15'44.47" N
	Longitude	157°40'8.23" W	157°51'53.90" W	157°49'21.27" W
	Water column depth (m)	3.1	12	3
	Distance from shore (m)	115	385	110
Sediment	Sand size (Wentworth)	very fine – fine	fine - medium	coarse - very coarse
	Mean grain size (μm)	187 ± 0.03*	223 ± 0.02	768 ± 0.003
	Fines (< 63 μm; wt. %)	10%	< 1%	<5 %
	Sorting	poorly sorted	well sorted	moderately well sorted
	Permeability (m^2)	$2.3 \pm 1.6 \times 10^{-12}$*	$4.7 \pm 1.1 \times 10^{-11}$**	$1.6 \pm 0.0 \times 10^{-10}$*
	Porosity	0.59 ± 0.01*	0.49***	0.49 ± 0.01
	CaCO$_3$ content (wt. %)	90.6 ± 0.4	93.7 ± 0.004	95.5 ± 0.3
	OM content (wt. % C)	0.55 ± 0.20	0.36 ± 0.20	0.32 ± 0.20

* Data from Angelos Hannides, personal communication
** Hannides (2008)
*** Hebert et al. (2007)
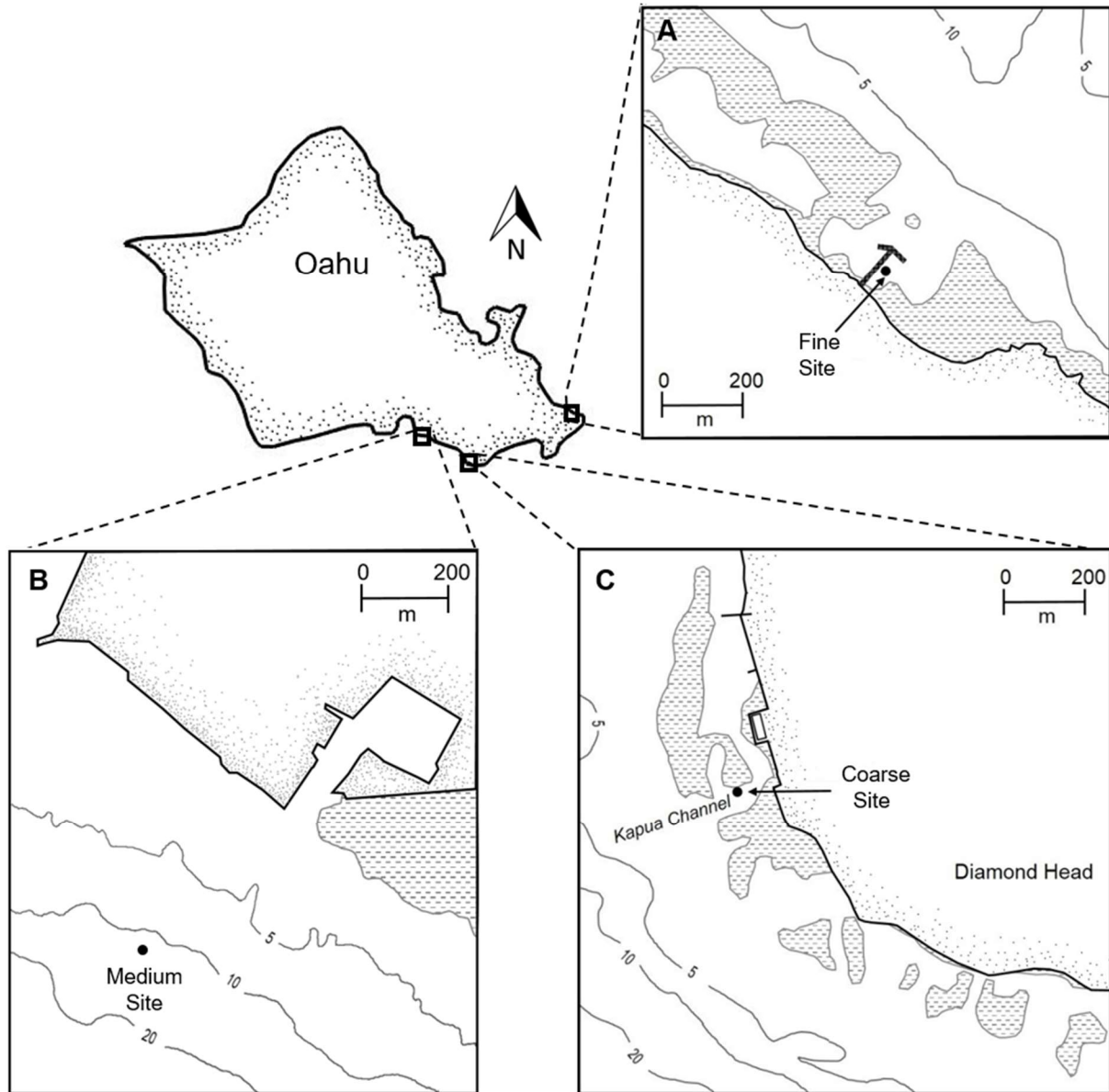
Figure 1.1 Overview of study site locations off Oahu, Hawaii. Dashed areas represent reef and filled circles indicate study sites. Contours are depth in meters. A) Makai Research Pier and the breakwall (indicated by black lines) adjacent to the Fine Site. B) Medium Site at Kilo Nalu Nearshore Observatory, C) Coarse Site in the Kapua Channel. Data from NOAA National Ocean Service Office of Coast Survey.

Chapter 2: Fine-scale spatial variability of nutrients in nearshore rippled permeable sediments

2.1 Abstract

Distinct spatial patterns have been observed in the structure of sediment porewater gradients in laboratory flume studies using permeable (sandy) sediments: higher nutrient concentrations are systematically found under ripple crests, while lower nutrient concentrations are observed under ripple troughs. However, this spatial variability has not been previously observed in the field. We used two different approaches at two nearshore sites to examine the spatial variability of dissolved nutrients in fine and coarse permeable sediment. First, small-scale lateral heterogeneity of nutrient concentrations from porewater samples (n = 10) at 5 cm below the sediment-water interface in a 1-m^2 plot was examined using randomized quadrat sampling. Both fine and coarse permeable sediments revealed varying dissolved nutrient concentrations, with the coarse sand displaying a 1.4-6.8 greater coefficient of variation than the fine sand. Second, spatial variability was examined by sampling porewater from three depths under sand ripple crests (n = 10) and sand ripple troughs (n = 10). These *in-situ* studies showed no statistical difference in nutrient concentrations with ripple location in the fine sand; however, statistically different nutrient concentrations between crest and trough were observed in the coarse sand. Similar to observations from flume studies subject to oscillatory flows, depth-integrated nutrient inventories under crests suggest higher inventories than under troughs in the fine sand, although the differences were not statistically significant. In the coarse sand, statistically different depth-integrated nutrient inventories suggest that oxygenated crests were migrating over a deeper, less oxygenated stationary sediment layer. This study supports the idea that the dominant nutrient-regulating process in the upper sediment of coarse sand is advective porewater circulation; however, other nutrient-regulating processes (e.g., organic matter deposition, bioturbation,

oscillating redox conditions, benthic photosynthesis/respiration) control fine-scale spatial variability of nutrients in fine sand.

2.2 Introduction

Sediment geochemists often ignore potential spatial heterogeneity largely due to sampling constraints when interpreting porewater concentration data. In non-bioturbated, fine-grained sediments, the distribution and transport of porewater constituents is controlled by molecular diffusion, and the remineralization of organic matter occurs in a thermodynamically predictable, vertically-stratified sequence (e.g., Froelich et al. 1979; Emerson and Hedges 2003). As a result, one-dimensional sampling techniques are adequate to characterize dissolved porewater constituents in most diffusively-dominated sediment regimes, since horizontal concentration gradients are generally weaker than vertical gradients (Berner 1980).

In contrast, sandy, permeable sediments are subject to advective porewater flows, thus allowing solute transport rates much greater than those due to molecular diffusion (Boudreau et al. 2001; Precht and Huettel 2003; Huettel et al. 2014). Enhanced porewater transport in permeable sediments can be driven by several processes, each of which can affect horizontal and vertical gradients of dissolved oxygen (DO), organic matter and nutrient distribution in the sediment.

First, as surface gravity waves pass over a permeable sediment, oscillatory boundary flows are produced and pressure gradients develop that enhance porewater transport, a process referred to as the "subtidal pump" (Riedl et al. 1972). Permeable sediment, influenced by this process, can develop a deeper DO penetration depth relative to that found in diffusively-dominated sediment. This oxygenated sediment layer then creates a "redox seal", preventing the

release of anoxic porewater from deeper sediments (Falter and Sansone, 2000; Precht et al., 2004; Figure 2.1A)

Second, advective porewater flows are produced as wave-generated oscillatory flows and current-driven unidirectional flows—or a combination thereof—interact with bottom topography (e.g., ripples, benthic mounds, shells; Santos et al., 2012b). The topography-induced pressure gradients force oxygenated bottom water and small particles (e.g., bacteria, algae, diatoms and detritus) into the sediment at areas of high pressure and release porewater to the water column at areas of low pressure (e.g., Figure 2.1; Huettel et al., 1996; Huettel and Rusch, 2000). Flume experiments with wave-generated oscillatory flows produce strong spatial patterns in porewater nutrient and DO concentrations when flowing over sediment ripples: lower nutrient and higher DO concentrations are systematically found under ripple troughs, while higher nutrient and lower DO concentrations are observed under ripple crests (Precht et al. 2004; Huettel et al. 2014). This has been attributed to physically induced, symmetrical porewater circulation and particulate deposition in the upper sediment, with bottom water and its associated particles entering at ripple troughs, and porewater constituents undergoing remineralization before the porewater exits at ripple crests (Figure 2.1B).

Similarly, flume studies with current-driven unidirectional flows over bottom topography also result in lateral spatial patterns in nutrient and DO distribution. As a unidirectional current flows over benthic topography, pressure gradients develop. For example, as currents flow over a ripple field, areas of high pressure are created on the upstream sides of the ripple crests, while low pressure areas develop on the downstream sides of the ripple crests (Huettel et al. 1996). As a result of the pressure gradient, small particles and oxygenated bottom water are forced into the sediment on the upstream side of the ripple crests, while low pressure

on the downstream side of the ripple crests acts as a conduit allowing more reduced, nutrient-rich porewater to reach the overlying water column (Figure 2.1C; Huettel et al., 1998). As near-bed flow increases, the upwelling anoxic porewater continues to be sheared in the direction of the current and can be separated from the sediment-water interface (SWI), trapping reduced constituents in the sediment (Figure 2.1D).

When current and wave stress exceed the bed erosion threshold, ripple migration occurs. Under such conditions, porewater is released from the upstream slopes of the ripples as sand particles are eroded, and bottom water is subsequently trapped as sand is deposited on the downstream side of the ripples (Santos et al. 2012b). Flume experiments reveal that migrating ripples create reduced porewater zones beneath ripple crests that sheared in the direction of the ripple migration, and result in oscillating sediment redox conditions with ripple migration (Precht et al., 2004). If the strength of near-bed boundary flows increase enough, ripple migration occurs faster than porewater movement, resulting in an oxygenated upper sediment layer that hinders the escape of the deeper, reduced porewater (Figure 2.1E).

Permeable sediments undergo redox oscillations when alternating oxic and anoxic conditions occur (e.g., as a result of ripple migration or non-continuous bioturbation/bioirrigation), and these oscillations affect sediment metabolism and subsequent nutrient distributions in different ways. First, redox oscillations increase the efficiency of organic matter remineralization (Aller 1994). Second, redox oscillations result in sorption and desorption of particle-reactive phosphorous on sediment surfaces (Keil and Hedges 1993). Third, redox oscillations can result in suboxic conditions that are ideal for nitrifying bacteria, leading to enhanced denitrification rates in carbonate sands (Haberstroh and Sansone 1999; Santos et al. 2012a)

Because advective forcing had previously been shown to affect horizontal and vertical distributions of porewater constituents in flume studies, the goals of this study were to: (1) evaluate the degree of fine-scale nutrient variability in the upper layers of two permeable sediments, and (2) compare the *in-situ* spatial variability of dissolved nutrients in these nearshore permeable sediments to the nutrient distributions observed across sand ripples during previously published laboratory studies. Two different *in-situ* experiments were performed to examine the spatial variability of dissolved nutrients in both a fine-sand and a coarse-sand permeable sediment. Our results show spatial variability in dissolved nutrient concentrations in both sediments, with smaller coefficients of variation in the fine-sand sediment. Additionally, results of this study suggest that porewater advection through sediment ripples is the dominant nutrient-regulating process in coarse-sand sediment; however, other nutrient-regulating processes (e.g., organic matter deposition/filtration, bioturbation/bioirrigation, redox oscillations, benthic photosynthesis/respiration) may control fine-scale spatial distribution of nutrients in fine-sand sediment.

2.3 Methods

2.3.1 Site Descriptions

Field experiments were conducted at two different sites off Oahu, Hawaii dominated by permeable, carbonate sediments (Figure 2.2). The selected sites were chosen primarily because of their contrasting sediment characteristics.

The Fine Site is located ~115 m from shore at Makai Research Pier (MRP), in a back-reef lagoon on the eastern shore of Oahu at a water depth of 3.1 m. The east side of Oahu is exposed to ocean swells generated from the northeasterly Trade Winds. These swells persist most of the year and have typical wave heights of 0.3-1.3 m, with periods of 5-8 s (Fletcher et al. 2002).

Because the back-reef lagoon is sheltered from the wave energy, sediment at MRP consists of very fine to fine sand.

The Coarse Site is located in the Kapua Channel, a small channel in the reef used by swimmers and human-powered watercraft in Honolulu on the south shore of Oahu. This site is ~110 m from shore at a water depth of 3.0 m. Unlike the first location, the Coarse Site is subject to swells generated by austral winter storms in the southern hemisphere that occur seasonally in summer and early autumn (April to October). These swells typically result in waves ranging from 0.3 to 1.2 m in height with 14- to 22- s periods, but can result in waves as high as 5.5 m with 25-s periods in fully developed seas (Moberly and Chamberlain 1964; Fletcher et al. 2002). As a result of more energetic conditions, the Coarse Site is dominated by coarse to very coarse sand.

2.3.2   *Measurement of water-column characteristics*

At the Fine Site, a bottom-mounted, upward-facing acoustic Doppler current profiler (ADCP; model WH, 1200 kHz, Teledyne RD Instruments) was deployed during porewater experiments and was configured to collect pressure and velocity data. Burst velocity measurements were measured at 1.06 m above the SWI every 5 min. At the Coarse Site, a bottom-mounted, upward-facing Aquadopp Profiler (AQD; 1.0 MHz, NortekUSA) was deployed during porewater experiments, and pressure and velocity measurements were measured at 0.30 m above the SWI at 1 Hz.

Because to instrumental differences, hydrodynamic measurements at the Fine (FS) Site were calculated at 1.06 m above the SWI, whereas measurements at the Coarse Site (CS) were recorded at just 0.30 m above the SWI. To compare the water-column velocities measured at different heights above the SWI at the two sites, velocities at the Fine Site were normalized to

0.30 m above the SWI by modeling the flow velocity as decreasing logarithmically towards the

SWI. To estimate the logarithmic decay of the flow velocities at the Fine Site, the mean shear

velocity, u_*, was calculated from the two bins closest to the SWI (Wright et al. 1999):

$$u_* = \frac{1}{5.75} \cdot \frac{d\bar{u}}{d\log z},$$ (2.1)

where $\bar{u}$ is the mean of the significant velocity measurements (m s^{-1}), and z is the depth of the

velocity measurements (m), reported as the center of the ADCP depth bin. For the Fine Site, the

mean of the significant velocities from 1.06 and 1.56 m above the SWI were used to calculate u_*.

With the mean u_* calculated, the logarithmic decay of the current velocity from its measurement

height above the SWI to 0.30 m above the SWI was estimated for the Fine Site by rearranging

Equation 2.1.

Throughout this study, near-bed flow (U_{Site}) was calculated from the main horizontal

velocity components using the root-mean square:

$$U_{Site} = \sqrt{\langle u^2 + v^2 \rangle_t}$$ (2.2)

where u and v represent flow parallel to the sediment bed in the east and north direction,

respectively; $\langle\ \rangle_t$ indicates the averaging of these variables over time ($t = 60$ min); and site

abbreviations (FS or CS) are used to denote the two sites. It is important to note that this

calculation quantifies near-bed flow regardless of whether the water flow is due to oscillatory

flow or unidirectional flow (Falter et al. 2005).

To examine whether the near-bed flows result from oscillatory or unidirectional flow, the same horizontal velocity components were used to calculate the magnitude of the mean horizontal velocity:

$$|\langle \boldsymbol{U} \rangle_{Site}| = \sqrt{\langle u \rangle_t^2 + \langle v \rangle_t^2} \qquad (2.3)$$

Calculations for $|\langle \boldsymbol{U} \rangle_{FS}|$ are not possible because the ADCP burst sampling we used does not measure the appropriate frequencies for capturing the oscillatory component of the flow.

Under conditions of near-bed flow due to purely oscillatory flow, $|\langle \boldsymbol{U} \rangle_{Site}| = 0$, while under conditions of purely unidirectional flow, $|\langle \boldsymbol{U} \rangle_{Site}| = U_{Site}$. As a result, the ratio of $|\langle \boldsymbol{U} \rangle_{Site}|: U_{Site}$ increases from 0 to 1 as conditions shift from purely oscillatory to purely unidirectional, and values of $|\langle \boldsymbol{U} \rangle_{Site}|:U_{Site}$ between 0 and 1 denote near-bed flow due to mixed conditions.

2.3.3   *Sampling and analysis of sediment*

Bulk-sample sediment grabs from the top ~10 cm of sediment were collected by divers for measurement of solid-phase characteristics. Grain-size distributions were determined by wet sieving, and the results were used to calculate mean grain size and sorting according to McManus (1988). Sediment porosities were measured gravimetrically (Breitzke 2000), and sediment permeabilities were obtained by the constant-head method (Klute and Dirksen 1986). Total weight percent carbon (TC; $\pm$ 0.12 %) was determined on ground sediment using an Elemental Analyzer (Exeter Analytical Elemental Analyzer, model CE-440; Gordon, 1969). Coulometery (UIC, model CM5230) was used to determine total weight percent inorganic carbon (TIC; $\pm$ 0.17 %; Dickson and Goyet, 1994), and the sediment organic matter content was

determined by difference (TC – TIC; $\pm$ 0.21 %). Sediment solid phase measurements of TIC were also used to estimate the calcium carbonate ($CaCO_3$) content of the sediment.

2.3.4 *Sampling and analysis of porewater*

2.3.4.1 *Porewater sampling*

Divers manually collected porewater samples for nutrient analysis using stainless-steel sampling needles inserted to the desired sediment depth, similar to Berg and McGlathery (2001). The porewater sampling needles were connected to 12-mL plastic syringes (Becton, Dickinson and Co.) via three-way stopcocks (Tomopal, Inc.). Custom-built needles (Hamilton Co.) with conical tips and two opposing side-sampling ports were used in this study to avoid sediment clogging. The needles were thin (1.6 mm i.d.) to ensure that minimal dead space needed to be cleared before collection of the intended porewater. Bottom-water nutrient samples were collected similarly, using syringes about 5 cm above the SWI. Once collected in the syringes, porewater and bottom-water samples were taken to shore and filtered through polyethersulfone syringe filters (25-mm diameter, nominal pore size of 0.2 µm). Water samples were stored cold (~1.5 °C) in the dark until analysis.

2.3.4.2 *Quadrat experiments*

The random-number generating function in MATLAB (The MathWorks, Inc.) was used to select 10 locations within a 1-m by 1-m quadrat with 10-cm grid spacing; the quadrat was constructed out of polyvinyl chloride (PVC) pipe and fishing line. Divers positioned the quadrat flush with the sediment bottom and sampled from 5 cm below the SWI at the bottom right corner of each randomly-selected grid point. After porewater samples were collected, divers recorded the ripple location for each of the samples (e.g., ripple crest, ripple trough). Quadrat sampling occurred at the Fine Site on 11 December 2013, and at the Coarse Site on 19 May 2015.

Assuming spherical volumes for the regions of the porewater sampled, sediment-sample volumes were calculated using porewater sample volumes (12 mL) and measured sediment porosities. The sediment-sample volumes at the Fine and Coarse Sites were ~20.3 and ~24.5 cm^3, respectively. These volumes correspond to a vertical porewater sample depth resolution of ~ ±1.7 cm at the Fine Site and ~ ±1.8 cm at the Coarse Site for the Quadrat Experiment.

Water samples collected during the Quadrat Experiments were analyzed for total dissolved nitrogen (TDN; ±0.14 μM), total dissolved phosphorous (TDP; ±0.15 μM), soluble reactive phosphate (SRP; ±0.04 μM), silicate (Si; ±0.05 μM), total nitrate + nitrite (NO$_x$; ±0.05 μM), and ammonium (NH$_4^+$; ±0.13 μM) using a nutrient AutoAnalyzer (Seal Analytical, model AA3 HR) using colorimetric methods for TDN, TDP, SRP, Si and NO$_x$(Grasshoff et al. 1983) and a fluorescence method for NH$_4^+$(Kérouel and Aminot 1997). The mean detection limits for TDN, TDP, SRP, Si and NO$_x$ and NH$_4^+$were 0.21 μM, 0.06 μM, 0.009 μM, 0.05 μM, 0.006 μM and 0.03 μM, respectively.

2.3.4.3   *Crest-trough experiments*

For Crest-Trough Experiments, a transect line was installed perpendicular to the ripple field to indicate the sampling locations. Porewater samples were collected at three sediment depths below 10 consecutive ripple crests and 10 consecutive ripple troughs, for a total of 60 porewater samples at each site. Bottom-water samples for analysis of dissolved inorganic nutrients were collected in triplicate. At the Fine Site, 5.0-mL porewater samples were collected at 3, 6, and 9 cm below the SWI; at the Coarse Site, 8.0-mL porewater samples were collected at 5.5, 11 and 16 cm below the SWI, adapting for the larger sand ripples at this site. Again, assuming a spherical sampling shape and accounting for sample volume and sediment porosity, porewater was extracted from a sediment volume of ~ 8.5 cm^3 at the Fine Site and ~ 16.3 cm^3 at

the Coarse Site, with a vertical depth resolution of about ±1.3 and ±1.6 cm, respectively. Lastly, ripple length and height measurements were made in the field using rulers. Ripple sampling occurred at the Fine Site on 13 June 2014 and at the Coarse Site on 22 May 2015.

Due to volume constraints, water samples collected during the Crest-Trough Experiments were analyzed for SRP (±0.6 µM), Si (± 0.3 µM) and NO_x (± 0.3 µM) using miniaturized colorimetric methods (Grasshoff et al. 1983; Campbell et al. 2006; Ringuet et al. 2011). Samples were reacted in 96-well optical-bottom plates with a 1-cm pathlength (Nalge Nunc International) and measured on a BioTek Synergy HT Multi-Mode Microplate Reader (BioTeck). Samples at the Fine Site were analyzed in duplicate for SRP and Si, while larger sample volumes at the Coarse Site allowed for analytical triplicates of SRP, Si and NO_x measurements. The mean detection limits for SRP, Si and NO_x were 0.6 µM, 0.6 µM and 1.1 µM, respectively.

During the Crest-Trough Experiment at the Fine Site, an *in-situ* Electrochemical Analyzer (ISEA-IV; AIS, Inc.) was deployed with a submersible micromanipulator mounted on an adjustable tripod to collect high-resolution voltammetric profiles of DO in the bottom water, across the sediment-water interface and in the upper sediment (Luther et al. 2008; Sansone et al. 2008). An optical DO sensor (Aanderaa 4330F) was also mounted ~5 cm above the SWI on the tripod to record ambient bottom-water temperature and DO during discrete sampling and profiling. Divers manually positioned the ISEA-IV tripod over sand ripple crests (n = 2) and ripple troughs (n = 2) to collect high-resolution DO profiles. The ISEA-IV was tethered to the surface at MRP with a 30 m ethernet cable to allow for real-time operation of the micromanipulator and voltammetric scanning. Unfortunately, due to sampling logistics, these measurements were not possible at the Coarse Site.

2.3.5   Porewater nutrient-inventory calculations

Depth-integrated sediment-porewater inventories for dissolved inorganic nutrients were calculated using the Curve Fitting Toolbox, a part of the MATLAB data processing software. First, dissolved nutrient concentrations in samples collected during Crest-Trough Experiments were fit using a shape-preserving interpolant and integrated to the deepest sampling depth: 9 cm at the Fine Site and 16 cm at the Coarse Site. Resulting integrations were then corrected for sediment porosity and are reported per m^2.

2.4   Results

2.4.1   Sediment characteristics and hydrodynamic regimes

Sediment and hydrodynamic characteristics for the Fine and Coarse Sites are summarized in Table 2.1. The upper sediment (defined here as the top 10 cm of sediment) at the Fine Site was a fine to very fine sand ($63-250$ μm) containing less than 10% fines (< 63 μm), with a permeability and porosity of $2.3 \pm 1.6 \times 10^{-12}$ m^2 (n = 2) and 0.59 ± 0.1 (n = 5), respectively. A mean grain size of 124 ± 2 μm (n = 2) and a sorting value of 1.53 ± 0 phi (n = 2) indicated a poorly sorted fine sandy sediment (McManus 1988). The upper sediment at the Fine Site consisted of 90.6 ± 0.4 % (n = 2) by weight $CaCO_3$, while the organic matter content of the upper sediment was estimated to be 0.6 ± 0 % (n = 2) by weight carbon (C).

The uppermost sediment at the Coarse Site was a coarse sand ($500-1000$ μm) with less than 5% fines, with a permeability and porosity of $1.61 \pm 0.0 \times 10^{-10}$ m^2 (n = 2) and 0.49 ± 0.01 (n = 5), respectively. A mean grain size of 768 ± 3 μm (n = 2) and a sorting value of 0.60 ± 0.02 phi (n = 2) indicated a moderately well sorted sediment (McManus 1988). The sediment at the Coarse Site was made up of 95.5 ± 0.3 % (n = 2) by weight $CaCO_3$, and the

estimated bulk sediment organic matter content of the upper sediment at the Coarse Site was 0.3 % $\pm$ 0.08 % (n = 2) by weight C.

The water-column hydrodynamics during the experiments at the Fine Site were characterized by generally weak near-bed flows ($U_{FS} = 0.03$ m s^{-1}; Figure 2.3A+B). There was typically a lack of uniform sand-ripple formation at the Fine Site (Figure 2.4A). However, relatively small sand ripples formed at the Fine Site after a day-long squall event associated with stronger near-bed flows ($U_{FS} = 0.08$ m s^{-1}; squall event not shown). Conversely, the Coarse Site was typically covered with uniform sand ripples (Figure 2.4B). Overall, relatively strong near-bed flow was observed at this site (Figure 2.3C; $U_{CS} = 0.23$ m s^{-1}). At the Coarse Site, near bed flow was a combination of oscillatory and unidirectional flow $|\langle U \rangle_{CS}|: U_{CS} = 0.32$), with the mean unidirectional flow onshore from the west/northwest.

During the Quadrat Experiment at the Fine Site on 11 December 2013, near-bed flows (U_{FS}) were 0.04 m s^{-1}. Similarly, during the Crest-Trough Experiment on 13 June 2014, near-bed flows of 0.03 m s^{-1} were observed at the Fine Site. During the Crest-Trough Experiment at the Fine Site, sand-ripples were relatively small, with a mean ripple wavelength of 13 $\pm$ 2.4 cm (n = 9) and a ripple height of ~ 3 cm.

During the Quadrat Experiment at the Coarse Site on 19 May 2015, near-bed flow (U_{CS}) was 0.19 m s^{-1} before increasing to 0.22 m s^{-1} during the Crest-Trough Experiment on 22 May 2015. The ratio of $|\langle U \rangle_{CS}|$ to U_{CS} indicates that conditions were more unidirectional for the Quadrat Experiment ($|\langle U \rangle_{CS}|: U_{CS} = 0.58$), while stronger, wave-driven near-bed flow dominated during the Crest-Trough Experiment ($|\langle U \rangle_{CS}|: U_{CS} = 0.35$). Relatively large sand-ripples, with a mean ripple wavelength of 55 $\pm$ 8 cm (n = 9) cm and a ripple height of ~ 16 cm, were observed at the Coarse Site during both experiments.

Lastly, benthic infauna, consisting mostly of polychaetes, was found in the upper sediment layer at the Fine Site, whereas burrowing shrimp and worm tubes were observed at the Coarse Site. Although not quantified for this study, bioturbation appeared more prevalent at the Fine Site.

2.4.2   Quadrat experiments

Porewater nutrient concentrations of Si, SRP, TDN, TDP, NH_4^+ and NO_x from the Quadrat Experiments are shown in Figure 2.5. At both sites, mean porewater nutrient concentrations from 5 cm below the SWI were enhanced over nutrient concentrations of the overlying water column.

Porewater samples (n = 10), collected at 5 cm below the SWI at the Fine Site, had TDN, Si and SRP concentrations of 24.1 ± 2.5 μM, 27.9 ± 6.8 μM and of 1.98 ± 0.78 μM, respectively. On average, porewater TDP (2.12 ± 0.73 μM) consisted of 93% SRP. Porewater samples from the Quadrat Experiment at the Fine Site were below the mean detection limit for the NO_x method (< 0.006 μM). Conversely, porewater concentrations for NH_4^+ were generally greater than the upper limit of quantification (~16 μM). However, three samples were diluted and quantified for NH_4^+ and had a mean concentration of 21.2 ± 2 μM. Due to sample volume constraints, the remaining over-range samples could not be rerun after their initial analysis.

Porewater samples (n = 10) collected at the Coarse Site from 5 cm below the SWI during the Quadrat Experiment had Si and SRP concentrations of 6.41 ± 4.00 μM and 2.50 ± 1.39 μM, respectively. Again, the majority of TDP (~81%) at the Coarse Site was present as SRP, resulting in TDP concentrations (3.00 ± 1.57 μM) being similar to SRP values. NO_x concentrations of 3.14 ± 3.11 μM, together with NH_4^+ concentrations of 2.13 ± 1.37 μM, accounted for about a third of the TDN (15.5 ± 5.60 μM) in porewater samples.

To examine the meter-scale variability of porewater samples collected during the Quadrat Experiments, the coefficient of variation (CV, %) was calculated for each nutrient. At the Fine Site, the CV for porewater nutrient concentrations ranged from 10.3% to 39.2%, while the CV for porewater nutrient concentrations ranged from 36.0% to 62.5% at the Coarse Site, resulting in meter-scale nutrient variation that was 1.4-6.8 times greater at the Coarse Site. A summary of statistics for the Quadrat Experiments can be found in Table 2.2.

2.4.3   *Crest-trough experiments*

Dissolved inorganic nutrient concentrations and inventories for samples collected from under ripple crests or under ripple troughs during the Crest-Trough Experiments are shown in Figure 2.6 (see Section 2.3.5 for calculations). To examine the variability of samples or inventories at each topological ripple location, CVs were calculated after grouping samples into crest or trough locations. CVs for crests were then compared to CVs for troughs to evaluate the relative amount of variation between the two locations. Next, to determine if porewater nutrient concentrations or inventories from under a crest or from under a trough were statistically different, a two-sample t-test was used. Values of p lower than 0.05 indicate that mean nutrient concentration are statistically different from each other, with 95% confidence levels (Snedecor and Cochran 1989). Statistics for the variability captured during the Crest-Trough Experiments are summarized in Table 2.3; additional nutrient data, including means and standard deviations, are available in Appendix A.

At the Fine Site, no statistically significant difference was determined between mean concentrations from crest or trough locations for Si and SRP at depths of 3, 6 and 9 cm below the SWI. However, at the Coarse Site, the porewater sample closest to the SWI (5.5 cm) had concentrations of Si, SRP and NO_x that were statistically different if sampled from under a crest

or from under a trough. Furthermore, although crest-trough SRP and NO_x concentrations were not statistically different at 11 cm below the SWI, Si concentrations were statistically different between crests and troughs at that depth. All nutrient concentrations for the deepest porewater samples at the Coarse Site (16 cm below the SWI) were statistically the same between crests and troughs.

DO profiles were collected from the bottom water and into the sediment for ripple crests or ripple troughs during the Crest-Trough Experiment at the Fine Site (Figure 2.7). Oxygen penetration depth was less than ~0.5 cm below the SWI in all four profiles. No difference in DO penetration depths below crests and below troughs was observed, consistent with the shallow oxygenation penetration depths recorded. Further, while the *in-situ* micromanipulator has a vertical incremental resolution of sub-millimeter-scale, visually identifying electrode position relative to the SWI in the dynamic environment was limited to about ± 0.2 cm.

2.5 Discussion

2.5.1 *Lateral meter-scale variability*

2.5.1.1 *Sedimentary redox structure*

The multi-dimensional redox structure that characterizes permeable sediments is a function of sediment metabolism, hydrodynamic regime, sediment characteristics and sediment topography (Ziebis et al. 1996; Werner et al. 2006). Similar to diffusively dominated sediments, the degree of organic matter remineralization in permeable sediments increases with time since deposition in the sediment (e.g., Canfield, 1993; Froelich et al., 1979). However, unlike in fine grained sediments, the degree of organic matter remineralization in rippled permeable sediments is not correlated with depth, but rather is correlated with distance and increasing porewater age along porewater flow pathways in the sediment (consistent with porewater residence times and

flow pathways observed by Precht et al., 2004). As a result, the oxygenation and resultant redox structure of these sediments is strongly correlated with the hydrodynamic forcing of the overlying water (Falter and Sansone 2000b; Precht et al. 2004; Werner et al. 2006; Fogaren et al. 2013). Unfortunately, the direct measurement of DO at both sites was not possible. Therefore, along with the available DO profiles, the relative amounts of dissolved inorganic nitrogen (DIN) present in the reduced form (NH_4^+) versus the oxidized form (NO_x) was used to estimate the degree of oxygenation of the sediments at this depth; this approach was used because DIN speciation is indicative of the degree of oxygenation of permeable sediments (Falter and Sansone 2000b).

During the Quadrat Experiment at the Fine Site, all measurable DIN was present in the reduced form (NH_4^+), indicating that the sediment was devoid of measurable DO by 5 cm depth. Furthermore, since porewater samples taken at 5 cm actually collected porewater from ~1.7 cm above and below that depth (see Section 2.3.4.2), the sediment at the Fine Site was likely anoxic by ~3.3 cm below the SWI. The lack of porewater oxygenation at this depth is a result of the relatively weak near-bed flows ($U_{FS} = 0.04$ m s^{-1}) and the likely resulting shallow DO penetration depths during the Quadrat Experiment. Although *in-situ* DO profiles were not made during the Quadrat Experiment, the similar hydrodynamic conditions observed during the Crest-Trough Experiment ($U_{FS} = 0.03$ m s^{-1}) make it reasonable to speculate that DO penetration depths were similar (< 0.5 cm; Figure 2.7) and that the porewater sampled was anoxic.

Conversely, DIN speciation at 5 cm below the SWI during the Quadrat Experiment at the Coarse Site was much more variable, and near-bed flows were nearly five times stronger ($U_{CS} = 0.19$ m s^{-1}). Unfortunately, DO profiles were not obtained due to logistical difficulties associated with the distance from shore. Therefore, to investigate the degree of sediment

oxygenation due to near-bed flow patterns through a rippled sediment, the randomized porewater samples were grouped into their closest sand ripple location (crest or trough), and DIN speciation was used. Consistent with observations from wave-driven flume experiments (Precht et al. 2004), DIN was more oxidized beneath ripple troughs ($NO_x = 72.4 \pm 8.5\%$; $n = 5$), while a greater percentage of reduced DIN was found below ripple crests ($NH_4^+ = 76.1 \pm 18\%$; $n = 5$). This analysis was not done for the Fine Site because all measurable DIN was present in the reduced form.

Near-bed flows at the Coarse Site were not entirely driven by oscillatory flows. During the Quadrat Experiment, near-bed flow was a combination of oscillatory and unidirectional flow, with 58% of the near-bed flow resulting from unidirectional flow. As discussed in the Introduction, when a unidirectional near-bed flow is superimposed on oscillatory flows, water flow through the rippled sediment is sheared in the direction of the net current (Figure 2.1C) and, if near-bed flows are strong enough, anoxic porewater is no longer able to exit at ripple crests (Figure 2.1D). Therefore, porewater samples were grouped into more descriptive sand ripple locations (trough, upstream slope, crest and downstream slope) to investigate the effect of the observed combination of wave-driven and current-driven bottom flows on the spatial structure of variability at the Coarse Site.

The DIN speciation observed at the Coarse Site agrees well with the scenario of a relatively strong bottom current superimposed on oscillatory flow over a rippled sediment (Figure 2.8). The most oxygenated sediment at the Coarse Site occurred under downstream slopes ($NO_x = 82.4 \pm 6.6\%$ of DIN, $n = 2$) and troughs ($NO_x = 78.1 \pm 1.2\%$ of DIN, $n = 2$), with the least oxygenated sediment observed under crests ($NH_4^+ = 78.4 \pm 7.9\%$ of DIN, $n = 4$) and, to a lesser degree, under upstream slopes ($NH_4^+ = 63.0 \pm 5.6\%$ of DIN, $n = 2$). As a result, NO_x and

NH$_4^+$ are the two most variable nutrients at the Coarse Site, and we conclude that DIN speciation is significantly affected by porewater flow pathways.

Additionally, the co-existence of reduced and oxidized DIN species in every porewater sample at the Coarse Site during the Quadrat Experiment suggests each sample collected porewater from both anoxic and oxic environments. The coexistence of thermodynamically incompatible porewater constituents and redox environments in permeable sediments has been attributed to the existence of microenvironments (Sansone and Chanton 1993; Rao et al. 2007; Rusch et al. 2009; Santos et al. 2012a). Conversely, the existence of only reduced DIN at the Fine Site during the Quadrat Experiment suggests we sampled only completely anoxic sediment. Therefore, despite sampling at the same depth at the two sites, we conclude that two different geochemical sedimentary environments were sampled at the Fine Site and the Coarse Site during the Quadrat Experiments.

2.5.1.2   *Fine site variability*

The sampling of different geochemical sedimentary environments at the two sites may help explain the nutrient variability, not only within each site, but also between the two sites. Samples from the Quadrat Experiment at the Fine Site all came from the relatively geochemically stable, anoxic zone of the sediment (discussed above), resulting in less overall lateral meter-scale nutrient variability at this site than at the Coarse Site. In the anoxic sediment sampled at the Fine Site, porewater flow at 5 cm below the SWI is assumed to be weak, and thus not the dominant mechanism controlling meter-scale nutrient variability (see Section 2.5.2).

If organic matter remineralization is solely responsible for DIN, SRP and Si sedimentary inventories, porewater nutrient-nutrient relationships will be linear, assuming that the type of organic matter undergoing remineralization is consistent throughout the sediment (Redfield et al.

1963; Tribble et al. 1990). Porewater nutrient-nutrient relationships at the Fine Site between DIN, SRP and Si all have linear trends (DIN-SRP, $R^2 = 0.67$; Si-SRP, $R^2 = 0.89$; Si-DIN, $R^2 = 0.99$; data not shown), indicating that inorganic nutrient regeneration is dominantly responsible for DIN, SRP and Si sedimentary concentrations. If nutrient variability at the site was driven by location or amount of organic matter retained within sediment, the nutrient-nutrient relationships would remain linear and the degree to which each inorganic nutrient varied would be the same. However, the degree of variation for each nutrient is not consistent, suggesting sedimentary-nutrient inventories are altered post-remineralization.

The largest degree of variation is with the P-species, perhaps due to the particle-reactive nature of SRP and DOP (e.g., Ruttenberg and Sulak, 2011; Ruttenberg, 2014). Despite the majority of our sediment consisting of $CaCO_3$ (Table 2.1), redox-sensitive iron oxide/oxyhydroxide (Fe_{ox}) minerals are commonly found in the coastal sediments of iron-rich volcanic islands (Ruttenberg and Sulak 2011). These Fe_{ox} minerals (e.g., ferrihydrite, goethite and hematite) have large P-sorbing capacities and can scavenge P from the porewater under oxic conditions (Ruttenberg et al. 2014). Conversely, if these Fe_{ox} minerals are then subjected to reduced conditions, P can be liberated from the minerals and released to the porewater, resulting in sediment P-inventories being sensitive to redox conditions (Ruttenberg et al. 2014); this may explain the large variation in the P-species at the Fine Site.

Oscillations in permeable sediment redox conditions are associated with changes in near-bed flows, bioturbation/bioirrigation and/or ripple migration (see Introduction). During both sampling approaches, consistently weak near-bed flows were observed and no ripple migration occurred at the Fine Site, indicating that changes in hydrodynamics or ripple migration at the site were not causing redox oscillations. However, although not quantified as part of this study,

bioturbation was observed at the Fine Site; thus redox oscillations that are often associated with bioturbation/bioirrigation (e.g., Aller, 1994; Huettel, 1990) could account for the enhanced SRP variability at this site. Additionally, enhanced organic-matter remineralization rates are often attributed to redox oscillations caused by bioturbation/bioirrigation, which could affect the lateral meter-scale variability of dissolved nutrients at the site (Aller 1994).

2.5.1.3   Coarse site variability

As discussed in Section 2.5.1, the lateral meter-scale variability of DIN was the greatest at the Coarse Site and seems to be related to the degree of sediment oxygenation along porewater flow paths through the rippled sediment. The degree of oxygenation in the sediments suggested by DIN speciation indicates that oxygenated bottom water enters at downstream slopes and troughs, and DO is consumed while porewater moves towards the upstream slope and ultimately the ripple crest, similar to the schematics shown in Figure 2.8. Similarly, dissolved inorganic nutrient concentrations are expected to increase as oxygenation decreases, with porewater age increasing from downstream slopes and troughs to upstream slopes and, finally, crests.

The increase of dissolved Si concentrations observed along the proposed porewater flow pattern supports the hypothesis that advective flow through the rippled sediment may control meter-scale nutrient variability at the site (Figure 2.8, top panel). At the Coarse Site, Si concentrations increase with proposed porewater age in the sediment: lowest concentrations occur under troughs (Si = 2.7 ± 0.4 µM; n =2) and downstream slopes (Si = 3.4 ± 1.5 µM; n = 2), and higher concentrations occur under upstream slopes (Si = 7.2 ± 0.5 µM; n = 2) and ripple crests (Si = 9.4 ± 4.5 µM; n = 4). Moreover, enhanced porewater Si concentrations in carbonate sediments have been observed to be well-correlated with the increase of porewater DIC concentrations produced during remineralization (e.g., Tribble et al. 1990, Fogaren et al. 2013).

This DIC-Si coupling may be attributed to the sedimentary recycling of organic matter associated with biogenic Si (e.g., planktonic and benthic diatoms, siliceous sponges; Tribble et al., 1990). In the case of diatoms, the organic matrix that protects frustules from dissolution is enzymatically degraded by microbes, allowing inorganic Si dissolution to occur in the sediment (Bidle and Azam 1999). Additionally, because Si dissolution rates depend on the degree of Si undersaturation (van Cappellen et al. 2002), advective porewater flows may enhance sedimentary silica dissolution rates by flushing the sediment with undersaturated seawater (Ehrenhauss and Huettel 2004; Ehrenhauss et al. 2004). As a result of the strong DIC-Si relationship, Si concentrations can be used as a proxy for the relative extent of diagenesis in the sediment, and indicate diagenetic processes occurring along predicted porewater pathways.

Unlike dissolved Si concentrations, DIN concentrations at the Coarse Site actually decrease with proposed porewater age (Figure 2.8, top panel). A possible explanation for this trend is the alteration of the remineralized DIN pool and subsequent removal from the sediment porewater. One possible mechanism for DIN removal is denitrification (Burdige 2006). Denitrification has been previously observed to increase in permeable carbonate sediments with an increase in porewater flow path and, therefore, an increase in porewater age (Santos et al. 2012a). In the same study, denitrification rates were observed to peak under intermediate flow conditions, which the authors attributed to the development of steep redox zones within microenvironments in oxic carbonate sediments. Although denitrification is often considered to be a strictly anoxic process (e.g., Froelich et al., 1979), Gao et al., (2010) suggest that aerobic denitrifying bacteria may adapt to frequent redox oscillations, allowing for the high denitrification rates they observed in sands. A second possible mechanism for removal of DIN at the Coarse Site is the anaerobic oxidation of NH_4^+ by NO_2^- (anammox; Thamdrup and

Dalsgaard, 2002). Although the significance of this process in N budgets is not well constrained (Devol 2015), anammox has been identified as an important removal mechanism of N in some marine sediments, including permeable sedimentary environments (Canion et al. 2014).

Unexpectedly, SRP concentrations do not trend with Si concentrations and increase along the proposed porewater flow path in the rippled coarse sediment, and there is no discernable pattern in the post-remineralization alteration of the dissolved P inventory (Figure 2.8, top panel). As discussed above for the Fine Site, dissolved P inventories can be affected by both the presence of P-sorbing minerals and redox oscillations in the sediment. Redox oscillations at the Coarse Site may also result from bioturbation as observed at the Fine Site. However, because this site is subject to much stronger near-bed flows, redox oscillations associated with ripple migration and/or pressure-driven porewater flow patterns are more likely to occur at the site than redox oscillations associated with bioturbation.

Lastly, strong linear relationships between inorganic nutrients should exist if organic matter remineralization (e.g., Redfield et al., 1963; Tribble et al., 1990) was the only mechanism responsible for lateral meter-scale variability at the Coarse Site. However, the lack of linear nutrient-nutrient correlations at this site (DIN-SRP, $R^2 = 0.09$; Si-SRP, $R^2 = 0.07$; Si-DIN, $R^2 = 0.29$; data not shown) supports the hypothesis of post-remineralization alteration of inorganic nutrient pools in the sediment by processes such as denitrification, anammox and P-sorption/desorption. Therefore, we conclude that lateral variability at the Coarse Site is driven by both the remineralization of organic matter along advective porewater pathways in the sediment and the subsequent chemical reaction of the resultant dissolved inorganic nutrients along the same pathways.

2.5.2   Nutrient variation with ripple location

The Crest-Trough Experiment was designed to further investigate the systematic spatial variability of dissolved nutrients in a rippled sediment. As shown in Table 2.3, Si and SRP concentrations at 3, 6, and 9 cm below the SWI at the Fine Site were statistically the same whether sampled from under a crest or under a trough. However, calculated sediment nutrient inventories for crests and troughs suggest a pattern anticipated for dissolved nutrients under a rippled sediment: higher nutrient inventories under crests and lower inventories under troughs. Although these sedimentary nutrient inventories are not statistically different, the pattern implies that bottom water and its associated organic matter may also be entering at troughs and undergoing remineralization before exiting at ripple crests at this site. Yet, this non-statistically significant result could also be an artifact of the sampling depths chosen for the Crest-Trough Experiment at this site. For example, the 3-cm sample depth may not have been close enough to the SWI to properly capture ripple field effects on nutrient distributions at the Fine Site, given the weak bottom flows and shallow DO penetration depths (Figure 2.7) observed at the site. Additionally, other nutrient-regulating processes (e.g., bioturbation, organic matter deposition) that were not specifically targeted by our field experiments may have a greater influence on spatial nutrient distributions in the sediment than porewater flow through the rippled sediment at this site.

At the Coarse Site, porewater nutrient concentrations were enhanced over bottom water concentrations, except for crest samples closest to the SWI. Those samples appeared to be well flushed with bottom water and contained relatively low nutrient concentrations, almost matching those of the overlying water column (Figure 2.6B). As a result, mean Si, SRP and NO_x concentrations 5.5 cm below the SWI of a crest were statistically different from those taken from

under a trough. However, deeper into the sediment, only Si concentrations from 11 cm below the SWI were not statistically different between crests or troughs. Also, while sediment SRP and Si inventories were statistically different between crest and trough locations, there was no difference in the NO_x sediment inventories between the crests and troughs.

Interestingly, the sedimentary nutrient inventories at the Coarse Site trended in the opposite direction to those at the Fine Site: higher nutrient inventories occurred under troughs and lower nutrient inventories occurred under crests (Figure 2.6). Taking the strength and the relative direction of near-bed flow during the Crest-Trough Experiment into consideration, it is likely that a migrating ripple field was sampled (similar to Figure 2.1E) during this experiment. In this scenario, the uppermost sediment is flushed completely with bottom water, which explains the low nutrient concentrations observed in the 5.5-cm deep porewater samples below crests. Furthermore, in this scenario the sediment below a crest is flushed deeper than is the sediment below a trough, which may explain lower sedimentary nutrient inventories at the Coarse Site.

2.5.3   *Sediment characteristics of rippled sediment*

Sediment characteristics (e.g., grain size, porosity) often change with depth in fine-grained sediments without bioturbation (Burdige 2006). Because of the dynamic nature of hydrodynamic porewater flows through permeable sediments, sediment characteristics not only change vertically but can also change horizontally along a sand ripple formation. Precht and Huettel (2004) observed that the mean grain size of ripple troughs was larger than that of crests in a non-migrating, rippled permeable sediment, and attributed this to the settling of larger particles in the ripple troughs. However, the larger particles created no statistical difference in the permeability and porosity of the crests versus the troughs at their study site.

As part of a companion study to the present research (A.K. Hannides, pers. comm.), sediment characteristics of ripple crests and ripple troughs were measured at our two field sites. There was no statistical difference between crest and trough sediment characteristics at the Fine Site, a likely consequence of the weak advective flows. However, sediment from ripple crests at the Coarse Site contained larger sand grains than sediment from ripple troughs, resulting in statistically greater permeability and porosity of ripple crests at the site. We infer that the hydrodynamic conditions at the Coarse Site systematically influenced both the sediment characteristics and nutrients concentrations (as previously discussed) along the ripple topography. The sediment at the Coarse Site appears to be made up of two layers: a more permeable layer migrating over a less permeable, stationary layer. As near-bed velocities at the Coarse Site increased during the experiments, the upper mobile sediment layer that made up the ripple crests appeared to migrate above the more stationary underlying sand layer. The migration of the ripple crests is thought to create a well-flushed upper sediment layer, resulting in nutrient concentrations of the uppermost crest porewater almost matching those of the overlying bottom water (Figure 2.6B).

2.5.4   *Comparison to other studies*

Due to the difficulty of obtaining permeable sediment porewater samples, few *in-situ* experiments are available for comparison. To our knowledge, this is the first *in-situ* study to observe the systematic variation of nutrient concentrations in a carbonate rippled sediment. Precht and Huettel (2004) measured dissolved inorganic nutrients 10, 20 and 30 cm below ripple crests and ripple troughs in a coastal permeable medium-sized siliceous sand with similar ripple characteristics to those observed at the Coarse Site. However, no lateral spatial variation was observed in the sediment, and this was attributed to rapid flushing with seawater. While the two

studies are not completely analogous, the lack of nutrient structure in Precht and Huettel's sediment emphasizes the fundamental difference between siliceous and carbonate sands, and indicates the potential importance of microenvironments in the biogeochemistry of carbonate sediments (e.g., Santos et al., 2012a).

2.6 Summary and implications for permeable sediment research

Dissolved nutrient concentrations varied laterally on a fine scale in both the fine and coarse sands examined here, but to varying degrees and due to different nutrient-regulating processes. Variations in nutrient concentrations and nutrient inventories at the Fine Site could not be attributed statistically to sediment ripple location. However, the lesser degree of variation observed at the Fine Site may be due to porewater sampling in only the anoxic zone of the sediment. Other mechanisms affecting the spatial distribution of nutrients (e.g., redox oscillation and organic matter deposition) could be of equal or greater significance, although our experiments were not designed to isolate the significance of these nutrient-regulating processes. Overall, the sediment at the Fine Site, in which weak near-bed currents flow over stationary sediment ripples, appeared similar to a diffusively-controlled sediment.

A greater degree of fine-scale dissolved nutrient variability was observed at the Coarse Site and the variability was systematically related to topographic position along the sand ripple field. The spatial distribution of dissolved nutrients in the sediment observed during the Quadrat Experiment (Figure 2.1D) changed as the site was exposed to the stronger wave-driven conditions observed during the Crest-Trough Experiment (Figure 2.1E). Stronger advective porewater flows appear to be the process primarily responsible for the dissolved nutrient structure in the sediment. However, observed nutrient distributions in the sediment were also

influenced by post-remineralization nutrient alteration (e.g. denitrification, P-sorption/desorption).

Our *in-situ* experiments demonstrate that sediment geochemistry and porewater nutrient distributions can be shaped by advective porewater flow through a rippled permeable sediment, complicating permeable sediment research in multiple ways. First, conventional one-dimensional sampling techniques do not seem appropriate in permeable sediments subject to advective flows, as horizontal nutrient gradients can be just as large as vertical nutrient gradients. Second, sediment geochemists should consider lateral variability when interpreting spatial and temporal observations in porewater concentrations of permeable sediments. Third, the effects of the changing hydrodynamic conditions in these environments need to be taken into account because of the tight coupling between hydrodynamics and the multi-dimensional structure of permeable sediment geochemistry. Last, spatial and temporal extrapolations of porewater nutrient concentrations need to be made cautiously because nutrient distributions in permeable sediments can vary along sand ripple fields and can be modified by changing hydrodynamic conditions. These complications can make understanding and quantifying the importance of permeable sediments in coastal and global nutrient budgets challenging.

2.7 Acknowledgements

2.8   References

Aller, R. C. 1994. Bioturbation and remineralization of sedimentary organic matter: effects of redox oscillation. Chem. Geol. **114**: 331–345.

Berg, P., and K. J. McGlathery. 2001. A high-resolution pore water sampler for sandy sediments. Limnol. Oceanogr. **46**: 203–210. doi:10.4319/lo.2001.46.1.0203

Berner, R. A. 1980. Early Diagenesis: A Theoretical Approach, Princeton University Press.

Bidle, K. D., and F. Azam. 1999. Accelerated dissolution of diatom silica by marine bacterial assemblages. Nature **397**: 508–512. doi:10.1038/17351

Boudreau, B. P., M. Huettel, S. Forster, and others. 2001. Permeable marine sediments: Overturning an old paradigm. Eos (Washington. DC). **82**: 133–136. doi:10.1029/EO082i011p00133-01

Breitzke, M. 2000. Acoustic and elastic characterization of marine sediments by analysis, modeling, and inversion of ultrasonic P wave transmission seismograms. J. Geophys. Res. **105**: 21,411-21,430. doi:http://dx.doi.org/10.1029/2000JB900153; doi:10.102

Burdige, D. J. 2006. Geochemistry of Marine Sediments, Princeton University Press.

Campbell, W. H., P. Song, and G. G. Barbier. 2006. Nitrate reductase for nitrate analysis in water. Environ. Chem. Lett. **4**: 69–73. doi:10.1007/s10311-006-0035-4

Canfield, D. E. DE. 1993. Organic Matter Oxidation in Marine Sediments, p. 333–363. *In* Interactions of C, N, P and S biogeochemical Cycles and Global Change.

Canion, A., J. E. Kostka, T. M. Gihring, M. Huettel, J. E. E. Van Beusekom, H. Gao, G. Lavik, and M. M. M. Kuypers. 2014. Temperature response of denitrification and anammox reveals the adaptation of microbial communities to in situ temperatures in permeable marine sediments that span 50 in latitude. Biogeosciences **11**: 309–320. doi:10.5194/bg-11-309-2014

van Cappellen, P., S. Dixit, and J. van Beusekom. 2002. Biogenic silica dissolution in the oceans: Reconciling experimental and field-based dissolution rates. Global Biogeochem. Cycles **16**: 10–23. doi:10.1029/2001GB001431

Devol, A. H. 2015. Denitrification, anammox, and N2 production in marine sediments. Ann. Rev. Mar. Sci. **7**: 403–23. doi:10.1146/annurev-marine-010213-135040

Dickson, A., and C. Goyet. 1994. Handbook of methods for the analysis of the various parameters of the carbon dioxide system in sea water.

Ehrenhauss, S., and M. Huettel. 2004. Advective transport and decomposition of chain-forming planktonic diatoms in permeable sediments. J. Sea Res. **52**: 179–197. doi:10.1016/j.seares.2004.01.004

Ehrenhauss, S., U. Witte, F. Janssen, and M. Huettel. 2004. Decomposition of diatoms and nutrient dynamics in permeable North Sea sediments. Cont. Shelf Res. **24**: 721–737. doi:10.1016/j.csr.2004.01.002

Emerson, S., and J. Hedges. 2003. Sediment diagenesis and benthic flux, p. 293–319. *In* Treatise on Geochemistry.

Falter, J. L., M. J. Atkinson, and C. F. M. Coimbra. 2005. Effects of surface roughness and oscillatory flow on the dissolution of plaster forms: Evidence for nutrient mass transfer to coral reef communities. Limnol. Oceanogr. **50**: 246–254. doi:10.4319/lo.2005.50.1.0246

Falter, J. L., and F. J. Sansone. 2000. Hydraulic control of pore water geochemistry within the oxic-suboxic zone of a permeable sediment. Limnol. Oceanogr. **45**: 550–557. doi:10.4319/lo.2000.45.3.0550

Fletcher, C. H., E. E. Grossman, B. M. Richmond, and A. E. Gibbs. 2002. Atlas of Natural Hazards in the Hawaii Coastal Zone. I-2761. U.S. Geological Survey.

Fogaren, K. E., F. J. Sansone, and E. H. De Carlo. 2013. Porewater temporal variability in a wave-impacted permeable nearshore sediment. Mar. Chem. **149**: 74–84. doi:10.1016/j.marchem.2012.12.005

Froelich, P. N., G. P. Klinkhammer, M. L. Bender, N. A. Luedtke, G. R. Heath, D. Cullen, and P. Dauphin. 1979. Early oxidation of organic matter in pelagic sediments of the eastern equatorial Atlantic: suboxic diagenesis. Geochim. Cosmochim. Acta **43**: 1075–1090.

Gao, H., F. Schreiber, G. Collins, and others. 2010. Aerobic denitrification in permeable Wadden Sea sediments. ISME J. **4**: 417–426. doi:10.1038/ismej.2009.127

Gordon, D. G. 1969. Examination of methods of particulate organic carbon analysis. Deep Sea Res. Oceanogr. Abstr. **16**: 661–665. doi:10.1016/0011-7471(69)90066-7

Grasshoff, K., M. Ehrhardt, and K. Kremling. 1983. Methods of Seawater Analysis. Second, Revised and Extended Edition, 3rd ed. Wiley-VCH.

Haberstroh, P. R., and F. J. Sansone. 1999. Reef framework diagenesis across wave-flushed oxic-suboxic-anoxic transition zones. Coral Reefs **18**: 229–240.

Huettel, M. 1990. Influence of the lugworm Arenicola marina on porewater nutrientprofiles of sand flat sediments. Marine Ecology Progress Series, 62(3): 241-248. Mar Ecol Prog Ser.

Huettel, M., P. Berg, and J. E. Kostka. 2014. Benthic exchange and biogeochemical cycling in permeable sediments. Ann. Rev. Mar. Sci. **6**: 23–51. doi:10.1146/annurev-marine-051413-012706

Huettel, M., and A. Rusch. 2000. Transport and degradation of phytoplankton in permeable sediment. Limnol. Oceanogr. **45**: 534–549. doi:10.4319/lo.2000.45.3.0534

Huettel, M., W. Ziebis, S. Forester, G. W. Luther III, S. Forster, G. W. Luther III, and G. W. Luther. 1998. Advective transport affecting metal and nutrient distributions and interfacial fluxes in permeable sediments. Geochim. Cosmochim. Acta **62**: 613–631. doi:10.1016/S0016-7037(97)00371-2

Huettel, M., W. Ziebis, and S. Forster. 1996. Flow-induced uptake of particulate matter in permeable sediments. Limnol. Oceanogr. **41**: 309–322.

Keil, R. G., and J. I. Hedges. 1993. Sorption of organic matter to mineral surfaces and the preservation of organic matter in coastal marine sediments. Chem. Geol. **107**: 385–388. doi:10.1016/0009-2541(93)90215-5

Kérouel, R., and A. Aminot. 1997. Fluorometric determination of ammonia in sea and estuarine waters by direct segmented flow analysis. Mar. Chem. **57**: 265–275.

Klute, A., and C. Dirksen. 1986. Methods of Soil Analysis: Part 1—Physical and Mineralogical Methods, Soil Science Society of America, American Society of Agronomy.

Luther, G. W., B. T. Glazer, S. Ma, and others. 2008. Use of voltammetric solid-state (micro)electrodes for studying biogeochemical processes: Laboratory measurements to real time measurements with an in situ electrochemical analyzer (ISEA). Mar. Chem. **108**: 221–235. doi:10.1016/j.marchem.2007.03.002

McManus, J. 1988. Grain size determination and interpretation, p. 63–85. *In* M. Tucker [ed.], Techniques in Sedimentology. Oxford (Blackwell).

Moberly, R. J., and T. Chamberlain. 1964. Hawaiian beach systems. Hawaii Inst. Geophys. Rep. HIG **64**.

Precht, E., U. Franke, L. Polerecky, and M. Huettel. 2004. Oxygen dynamics in permeable sediments with wave-driven pore water exchange. Limnol. Oceanogr. **49**: 693–705. doi:10.4319/lo.2004.49.3.0693

Precht, E., and M. Huettel. 2003. Advective pore-water exchange driven by surface gravity waves and its ecological implications. Limnol. Oceanogr. **48**: 1674–1684. doi:10.4319/lo.2003.48.4.1674

Precht, E., and M. Huettel. 2004. Rapid wave-driven advective pore water exchange in a permeable coastal sediment. J. Sea Res. **51**: 93–107. doi:10.1016/j.seares.2003.07.003

Rao, A. M. F., M. J. McCarthy, W. S. Gardner, and R. a. Jahnke. 2007. Respiration and denitrification in permeable continental shelf deposits on the South Atlantic Bight: Rates of carbon and nitrogen cycling from sediment column experiments. Cont. Shelf Res. **27**: 1801–1819. doi:10.1016/j.csr.2007.03.001

Redfield, A., B. Ketchum, and F. Richards. 1963. The influence of organisms on the composition of seawater, p. 26–77. *In* M. Hill [ed.], The Sea. Interscience.

Riedl, R. J., N. Huang, and R. Maohan. 1972. The subtidal pump: a mechanism of interstitial water exchange by wave action. Mar. Biol. **13**: 210–221.

Ringuet, S., L. Sassano, and Z. I. Johnson. 2011. A suite of microplate reader-based colorimetric methods to quantify ammonium, nitrate, orthophosphate and silicate concentrations for aquatic nutrient monitoring. J. Environ. Monit. **13**: 370–6. doi:10.1039/c0em00290a

Rusch, A., A. K. Hannides, and E. Gaidos. 2009. Diverse communities of active Bacteria and Archaea along oxygen gradients in coral reef sediments. Coral Reefs **28**: 15–26. doi:10.1007/s00338-008-0427-y

Ruttenberg, K. C., G. M. Filippelli, K. C. Ruttenberg, G. M. Filippelli, and K. C. Ruttenberg. 2014. The Global Phosphorus Cycle, p. 499–588. *In* H. H.D. and K.K. Turekian [eds.], Treatise on Geochemistry. Elsevier Ltd.

Ruttenberg, K. C., and D. J. Sulak. 2011. Sorption and desorption of dissolved organic phosphorus onto iron (oxyhydr)oxides in seawater. Geochim. Cosmochim. Acta **75**: 4095–4112. doi:10.1016/j.gca.2010.10.033

Sansone, F., and J. Chanton. 1993. Methane cycling in coral reef frameworks. Trends Microb. Ecol. **6**: 157–162.

Sansone, F. J., G. Pawlak, T. P. Stanton, and others. 2008. Kilo Nalu physical/biogeochemical dynamics above and within permeable sediments. Oceanography **21**: 173–178.

Sansone, F. J., G. W. Tribble, C. C. Andrews, and J. P. Chanton. 1990. Anaerobic diagenesis within Recent, Pleistocene, and Eocene marine carbonate frameworks. Sedimentology **37**: 997–1009.

Santos, I. R., B. D. Eyre, and R. N. Glud. 2012a. Influence of porewater advection on denitrification in carbonate sands: Evidence from repacked sediment column experiments. Geochim. Cosmochim. Acta **96**: 247–258. doi:10.1016/j.gca.2012.08.018

Santos, I. R., B. D. Eyre, and M. Huettel. 2012b. The driving forces of porewater and groundwater flow in permeable coastal sediments: A review. Estuar. Coast. Shelf Sci. **98**: 1–15. doi:10.1016/j.ecss.2011.10.024

Snedecor, G. W., and W. G. Cochran. 1989. Statistical Methods, 8th Editio. Iowa State University Press.

Thamdrup, B., and T. Dalsgaard. 2002. Production of N 2 through Anaerobic Ammonium Oxidation Coupled to Nitrate Reduction in Marine Sediments. Appl. Environ. Microbiol. **68**: 1312–1318. doi:10.1128/AEM.68.3.1312

Tribble, G. W., F. J. Sansone, and S. V Smith. 1990. Stoichiometric modeling of carbon diagenesis within a coral reef framework. Geochim. Cosmochim. Acta **54**: 2439–2449.

Werner, U., P. Bird, C. Wild, and others. 2006. Spatial patterns of aerobic and anaerobic mineralization rates and oxygen penetration dynamics in coral reef sediments. Mar. Ecol. Prog. Ser. **309**: 93–105. doi:10.3354/meps309093

Wright, J., A. Colling, D. Park, and Open University. Oceanography Course Team. 1999. Waves, tides, and shallow-water processes, Butterworth-Heinemann, in association with the Open University.

Ziebis, W., M. Huettel, and S. Forster. 1996. Impact of biogenic sediment topography on oxygen fluxes in permeable seabeds. Mar. Ecol. Prog. Ser. **140**: 227–237. doi:10.3354/meps140227

Table 2.1: Summary of study site characteristics. Reported errors are ± 1 standard deviation.

	Fine Site	Coarse Site
Location	Makai Research Pier	Kapua Channel
Latitude	21°19'9.16" N	21°15'44.47" N
Longitude	157°40'8.23" W	157°49'21.27" W
Water column depth (m)	3.1	3
Distance from shore (m)	115	110
Sediment OM content (wt. % C)	0.6 ± 0	0.3 ± 0.08
Mean grain size (μm)	124 ± 2	768 ± 3
Fines (< 63 μm; wt. %)	10 %	<5 %
Sorting	Poorly sorted	Moderately well sorted
Sediment permeability (m^2)	$2.3 \pm 1.6 \times 10^{-12}$	$1.61 \pm 0.0 \times 10^{-10}$
Sediment porosity	0.59 ± 0.01	0.49 ± 0.01
$CaCO_3$ content (wt. %)	90.6 ± 0.4	95.5 ± 0.3
Sand ripple wave length (cm)	13 ± 2.4	55 ± 8
Sand ripple wave height (cm)	3	16
Quadrat sample depth (cm)[a]	5	5
Crest-Trough sample depths (cm)[a]	3, 6, 9	5.5, 11, 15
Mean near-bed flow, U_{rms}	0.03 ± 0.02	0.23 ± 0.02

[a]Depth below the SWI.

Table 2.2: Statistics for porewater nutrient concentrations (n = 10, except as noted) sampled from 5 cm below the SWI during Quadrat Experiments. STD = standard deviation, CV = coefficient of variation, CS = Coarse Site, FS = Fine Site. NO_x samples taken at the FS were below the limit of detection (LOD).

Analyte	Mean conc. (µM) ± STD		CV (%)		CV_{CS}: CV_{FS}
	FS	CS	FS	CS	
Si	27.9 ± 6.8	6.4 ± 4.0	24.4	62.5	2.6
TDP	2.1 ± 0.73	3.0 ± 1.6	34.6	52.1	1.5
SRP	2.0 ± 0.78	2.5 ± 1.4	39.2	55.8	1.4
TDN	24.1 ± 2.5	15.6 ± 5.6	10.3	36.0	3.5
NH_4^+	21.2 ± 2.0*	2.1 ± 1.4	9.4	64.6	6.8
NO_x	<LOD	3.1 ± 3.1	--	99.0	NA

*n = 3 samples for NH_4^+ at the Fine Site (see text).

Table 2.3: Statistics for the Crest-Trough Experiments. Statistics are grouped into crest or trough for each nutrient sample depth (n = 10) or depth-integrated nutrient inventory (Inv.; n = 10). Nutrient inventories are calculated per m^2; see Section 2.3.5 for nutrient inventory calculations. CV = coefficient of variation; CV_C = CV for crest; CV_T = CV for trough; CV_C:CV_T is the ratio of the relative variability between crests and troughs at indicated sample depth or inventory. Statistically significant p-values ($p < 0.05$) for crests versus troughs, and their corresponding depth or inventory, are in bold. Additional nutrient data, including means and standard deviations are available in Appendix A.

Site	Nutrient	Depth	Variability			
			CV_C (%)	CV_T (%)	CV_C:CV_T	*p-value*
Fine Site	Si	3 cm	31.2	19.8	1.6	0.051
		6 cm	23.5	8	2.9	0.300
		9 cm	15.0	8.7	1.7	0.294
		Inv.	21.9	11	2.0	0.051
	SRP	3 cm	30.5	25.5	1.2	0.382
		6 cm	33.3	23.1	1.4	0.057
		9 cm	28.6	17.4	1.6	0.054
		Inv.	21.6	19.4	1.1	0.157
Coarse Site	Si	**5.5 cm**	35.6	37.2	1.0	**2.82E-06**
		11 cm	35.3	47.9	0.7	**0.022**
		16 cm	44.1	71.6	0.6	0.297
		Inv.	24.2	41.6	0.6	**2.10E-03**
	SRP	**5.5 cm**	128	42.9	3.0	**2.96E-04**
		11 cm	37.4	33.4	1.1	0.807
		16 cm	43.9	66.8	0.7	0.600
		Inv.	36.1	34.2	1.1	**0.032**
	NO$_x$	**5.5 cm**	298	55.5	5.4	**0.014**
		11 cm	16.9	92.4	0.2	0.281
		16 cm	66.0	87.3	0.8	0.869
		Inv.	55.3	53.5	1.0	0.332
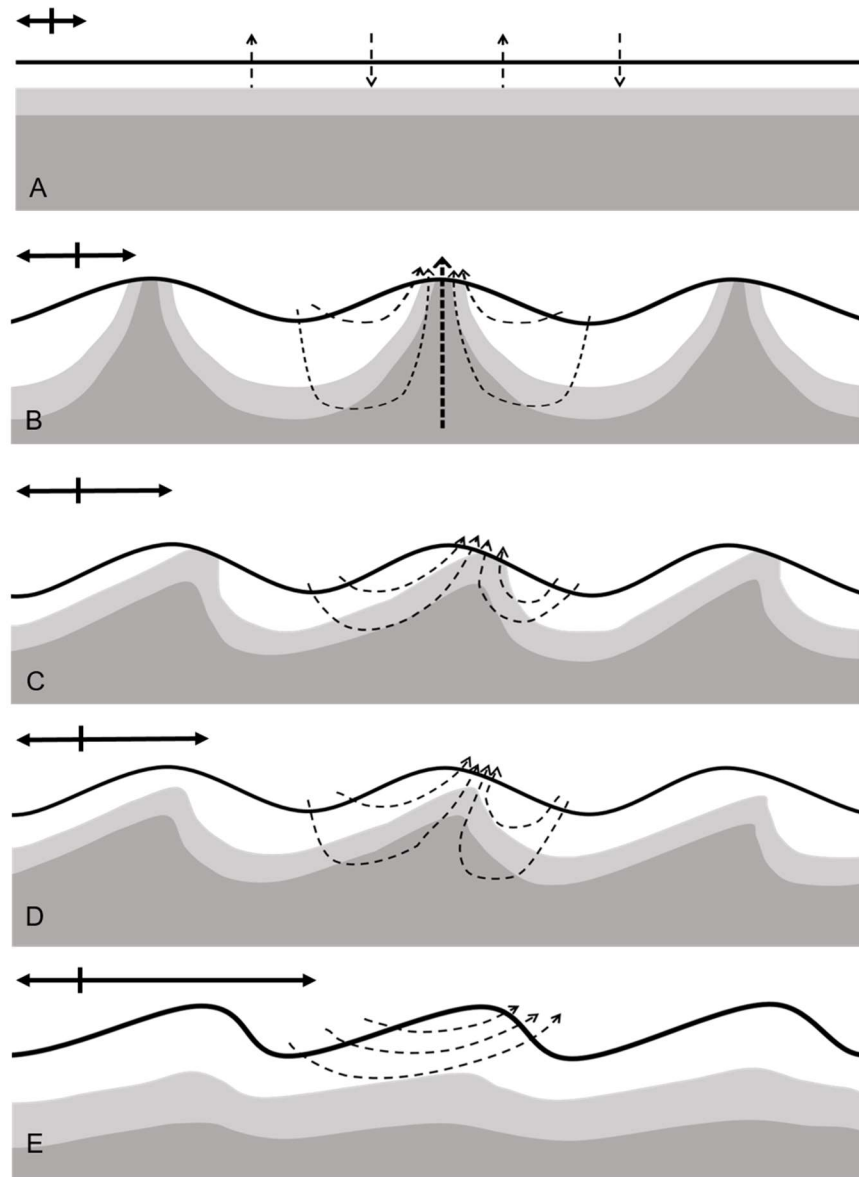
Figure 2.1: Schematic cross-sections of a conceptual permeable sediment under various near-bed flows. Black line represents the SWI; black horizontal arrows indicate relative strengths and directions of near bed flows; dashed arrows show porewater pathways as bottom water flows through sediment; white areas represents oxygenated sediment; grey and dark grey areas represent increasingly anoxic sediment conditions; not to scale. (A) Non-rippled sediment under weak oscillatory bottom flows; wave pumping (see Introduction) causes a deeper DO penetration depth than under simply diffusive conditions. (B) Rippled sediment under oscillatory bottom flow; oxygenated bottom water enters at ripple troughs and anoxic porewater exits to the water column through ripple crests. (C) Rippled sediment subject to oscillatory flow and weak-to-moderate unidirectional near-bed flow; the addition of a unidirectional current results in upwelling of anoxic porewater downstream of ripple crests. (D) Rippled sediment subject to

48

oscillatory flow and moderate unidirectional near-bed flow; as bottom currents increase, upwelling anoxic porewater may not cross the SWI, trapping reduced porewater constituents in the sediment. (E) Rippled sediment subject to oscillatory flow with a strong unidirectional bottom current; anoxic sediment is separated from the overlying water column by a thick oxygenated sediment layer. Adapted from Huettel et al., 2014 and Precht et al., 2004.
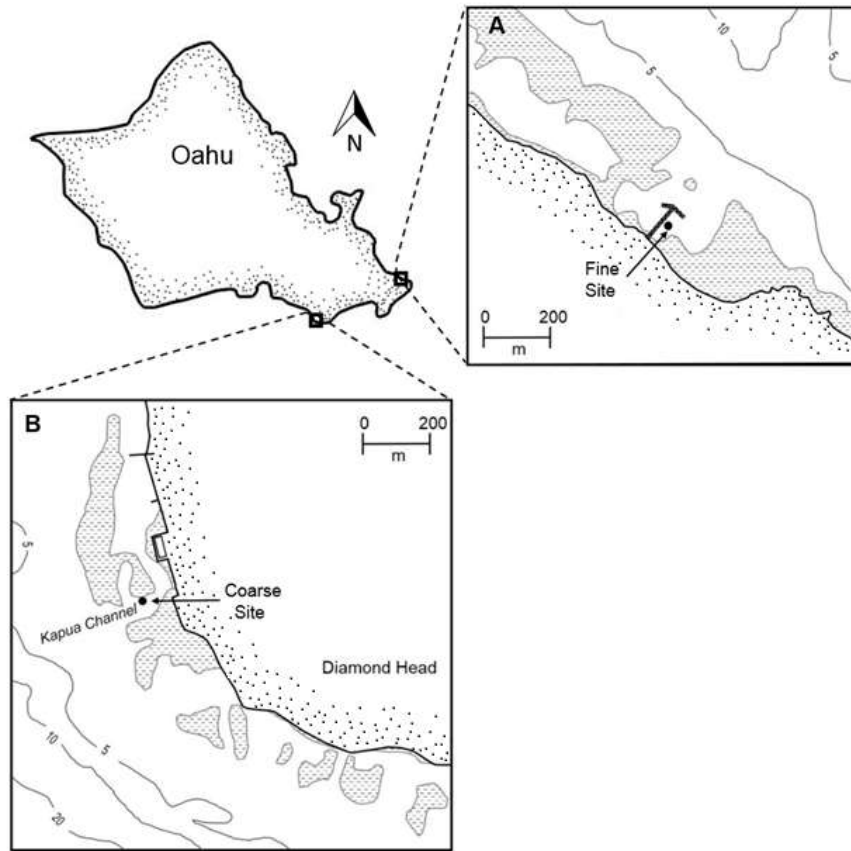
Figure 2.2: Overview of study site locations on Oahu, Hawaii. Dashed areas represent reef and filled circles indicate study sites. Contours show depth in meters. (A) Makai Research Pier and breakwall (indicated by black lines) adjacent to the Fine Site. (B) Coarse Site in the Kapua Channel. Data for both inserts from NOAA National Ocean Service Office of Coast Survey.
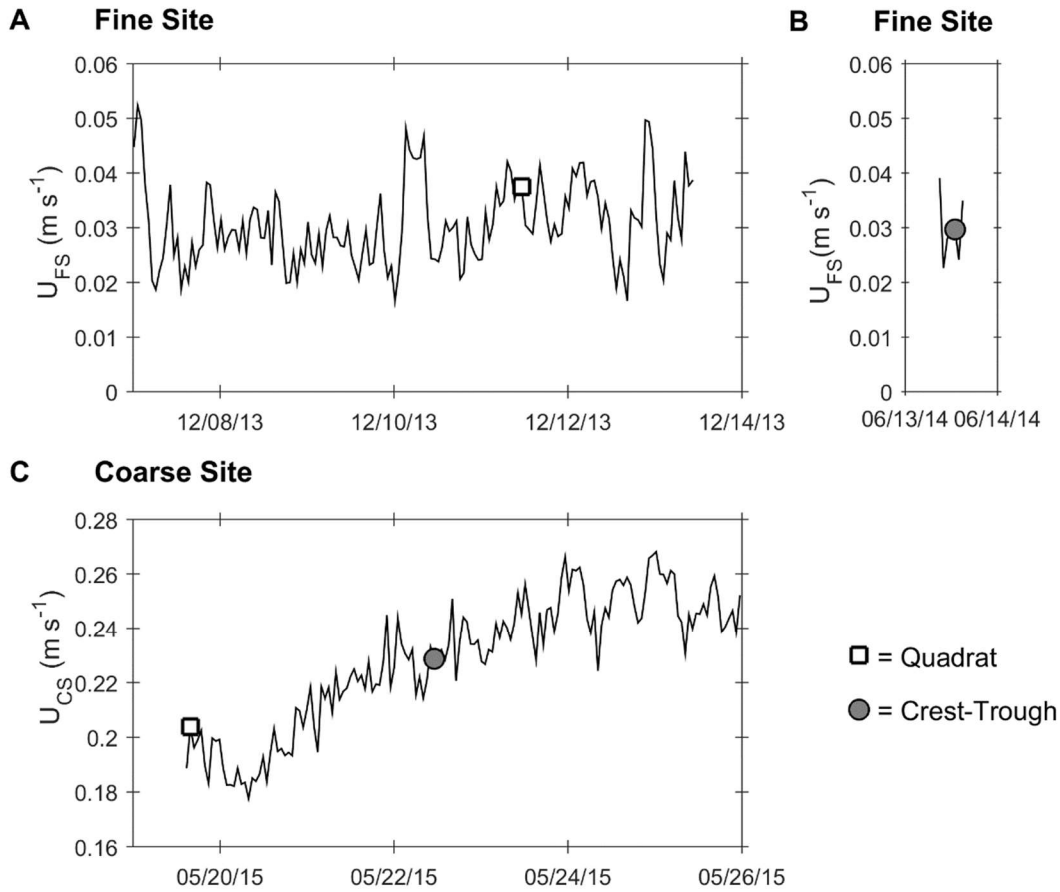
Figure 2.3: Near-bed flows for the Fine and Coarse Sites; note the change in axes between sites. Open squares (□) represent the Quadrat Experiments and filled circles (●) represent the Crest-Trough Experiments. (A+B) Near-bed flows (calculated for 0.30 m above the SWI; see Section 2.3.2) at the Fine Site. (C) Near-bed flows (measured 0.30 m above the SWI) at the Coarse Site.
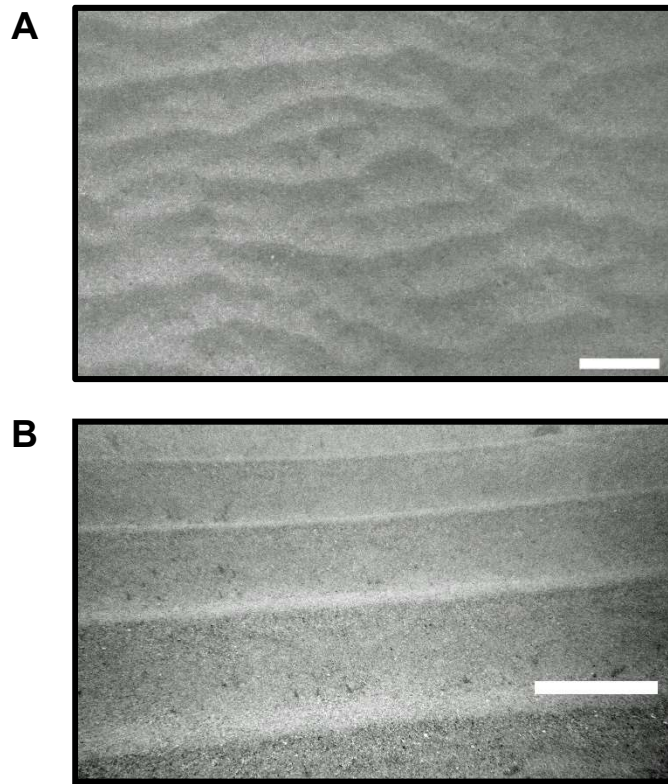
Figure 2.4: Sand ripples at the two sites. (A) Plan view of the Fine Site; the white scale bar is 15 cm. (B) Oblique view of the Coarse Site; the white scale bar is ~50 cm at the location shown.

A   **Fine Site**   **B**   **Coarse Site**

Figure 2.5: Plan-view maps of 1-m^2 quadrat sampling area showing porewater results for analytes at (A) the Fine Site and (B) the Coarse Site. Porewater samples (from 5 cm below SWI) are indicated with circles. Colors of filled circles correspond to the adjacent concentration bars for Si, SRP, TDN and TDP, NO$_x$ and NH$_4^+$; circles marked with an × represent concentrations below the limit of detection. Note the changes in ranges of nutrient concentrations.

A Fine Site

Crests: Si (μM) | Troughs: Si (μM) | Crests: SRP (μM) | Troughs: SRP (μM) | Crests: | Troughs:

1796 μmol/m^2

1526 μmol/m^2

44.7 μmol/m^2

39.2 μmol/m^2

B Coarse Site

Si (μM) | Si (μM) | SRP (μM) | SRP (μM) | NO$_x$ (μM) | NO$_x$ (μM)

200.1 μmol/m^2

393.8 μmol/m^2

52.5 μmol/m^2

76.3 μmol/m^2

185.9 μmol/m^2

237.4 μmol/m^2

Depth below SWI (cm)
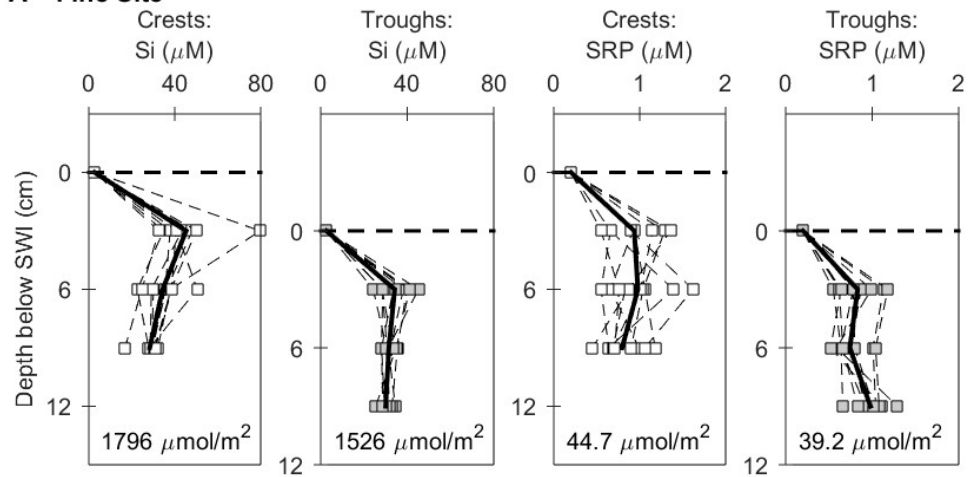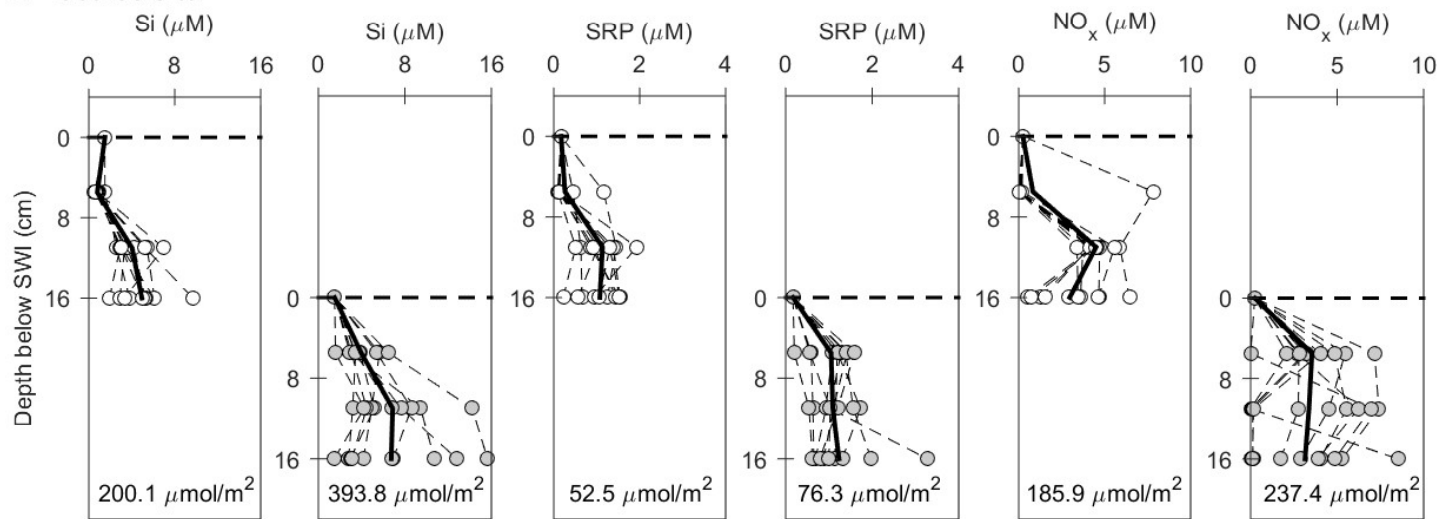
Figure 2.6: Porewater results for the Crest-Trough Experiments; each plot shows porewater profiles (n = 10) for a given analyte taken under a crest or trough. Squares (Fine Site) and circles (Coarse Site) respresent individual porewater samples, with dashed lines connecting samples in each profile; the SWI is represented with a horizontal dashed line at depth = 0; open symbols are crest samples and filled symbols are trough samples; the mean values at each depth are shown as solid black lines; mean nutrient inventories per m^2 are provided at the bottom of each plot; see Section 2.3.5 for complete nutrient inventory calculations. (A) Si and SRP porewater concentrations for the Crest-Trough Experiment at the Fine Site. (B) Si, SRP and NO_x porewater concentrations for the Crest-Trough Experiment at the Coarse Site. Note different concentration scales between the two sites.
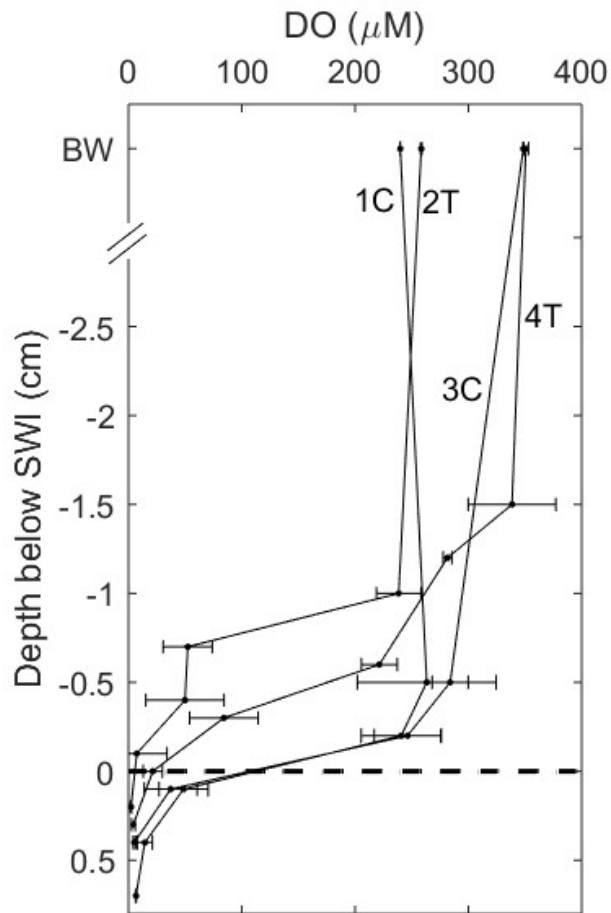
Figure 2.7: Dissolved oxygen (DO) profiles taken at the Fine Site during the Crest-Trough Experiment. Profiles are sequentially numbered, with topographical location indicated as crest (C) or trough (T). Points represent the mean (n = 3); error bars representing ±1 standard deviation. The dashed horizontal line indicates the SWI. Vertical depth resolution is about ± 0.3 cm. The bottom water (BW) measurement was ~5 cm above the SWI of mean sediment height of ripple crests and troughs. Profile start times for 1C, 2T, 3C and 4T were 9:28, 10:04, 13:13 and 14:45 HST, respectively.
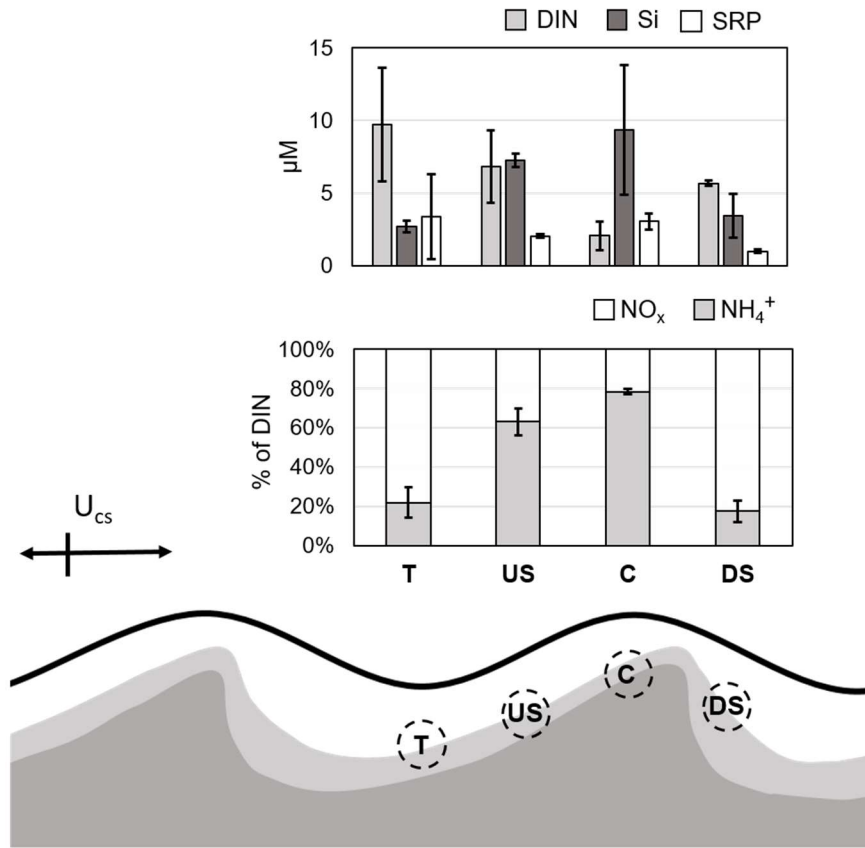
Figure 2.8: Schematic cross-section of the rippled sediment at the Coarse Site during the Quadrat Experiment. The black, horizontal arrow indicates the relative strength and direction of the near-bed flow; white area represents oxygenated sediment, grey and dark grey areas represent increasingly anoxic sediment. Porewater sample locations and sampling volumes (see Section 2.3.4.1) are shown by dashed circles; ripples not to scale. Porewater samples were grouped into trough (T, n = 2), upstream slope (US, n = 2), crest (C, n = 4) or downstream slope (DS, n = 2) according to sample locations. Slopes are defined relative to ripple crest: upstream slope refers to the area between a trough and a crest in the direction opposite of the flow, while downstream slope refers to the area between a crest and a trough in the direction of flow. Upper bar graphs show the mean concentrations of DIN, Si and SRP grouped by ripple location. Lower bar graphs show the mean percentage of DIN present in the oxygenated (NO_x) or reduced (NH_4^+) form grouped by ripple location. Error bars are the standard deviation of the mean.

Chapter 3: A statistical method for calculating 1-D porewater velocities and effective diffusivities from temperature time series

3.1 Abstract

While the biogeochemical importance of advective flows in permeable sediment environments is established, the direct measurement of material fluxes in these environments remains challenging. We present a method using transient heat as a natural tracer of fluid transport to estimate vertical exchange in permeable sediments. While this approach has gained popularity in freshwater environments, few studies have utilized this method in marine environments. We develop here a method using a statistical solution to the 1-D heat transport model to estimate vertical front velocities and effective thermal diffusivities from unfiltered temperature time-series from an array of buried thermistors. Vertical porewater velocities are then obtained after applying known sediment thermal parameters. The use of unfiltered temperature data avoids potential problems associated with isolating a single frequency of the temperature signal in environments where changes in temperature structure reflect a variety of processes. The method is assessed using streambed datasets from New York and marine datasets from a nearshore sandy sediment in Hawaii. Estimates of effective thermal diffusivity and thermal front velocity are used to statistically evaluate proposed relationships between thermal dispersivity and velocity for both the freshwater and marine environments.

3.2 Introduction

Although sandy, permeable sediments (permeability $> 10^{-12}$ m^2) cover nearly half of continental shelves worldwide (Riedl et al. 1972; Hall 2002), their role in coastal and global biogeochemical budgets is not well constrained. Permeable sediments are subject to much higher advective flows than fine sediments, which typically enhance fluid and particle exchange

between the porewater and the overlying water column (Santos et al. 2012b; Huettel et al. 2014). This enhanced exchange of solutes and particles promotes a biogeochemically active system by delivering oxygenated water (Ziebis et al. 1996; Fogaren et al. 2013) and labile organic matter (Huettel et al. 1996; Huettel and Rusch 2000b) to the sediments while flushing remineralization end-products to the overlying water column (Grigg 1995; Huettel et al. 1998b).

While the biogeochemical importance of advective flows in permeable sediments is well established, quantifying advective transports across the sediment-water interface (SWI) in natural environments remains challenging. Conventional methods used to calculate porewater fluxes in fine-grained, diffusively dominated sediments (e.g., coring, porewater extraction, benthic chambers) are often unsuitable for permeable sediments because they disrupt the structure of sand sediments, or interfere with the hydrodynamics that make permeable sediments so reactive (Boudreau et al. 2001). As a result, eddy-correlation techniques (Berg et al. 2003), stirred benthic chambers (Janssen et al. 2005), and dye-based tracer studies (Precht and Huettel 2004b; Hebert et al. 2007) have been developed as less invasive techniques to measure fluxes in permeable sediment environments.

In freshwater permeable sediment environments, transient heat has been used as a natural tracer of fluid transport to estimate vertical exchange between streams and aquifers (e.g., Briggs et al. 2012; Gordon et al. 2013; Rau et al. 2014). The transport of heat through a saturated, porous medium occurs due to convection and conduction, and the rate and attenuation of the signal propagation depends on the thermal properties of the sediment-water matrix, the period of the surface temperature signal, and the velocity of the vertical fluid flow in the sediment (Goto et al. 2005). As a result, numerous freshwater studies have exploited the daily temperature

fluctuations of surface waters to calculate vertical water fluxes by measuring the rate and strength of the temperature penetration into the sediment.

In these environments, surface-water temperature variations occur primarily at a daily period due to solar heating. Consequently, methods have focused on the dominant diurnal temperature signal that penetrates within the sediment. Relative to temperature variations above the SWI, the diurnal signal below the SWI becomes increasingly lagged in time and attenuated with depth (Figure 3.1). The degree of temperature lag and attenuation depend largely on the rate of heat transfer, with the amplitude decaying exponentially, and with phase delayed linearly with depth in the sediment (Stallman 1965; Goto et al. 2005). Observations to determine the temperature lag and attenuation (e.g., using thermistors within the sediment) can then be used to estimate porewater advection, including vertical velocities that can then be used to specify the exchange of dissolved constituents (e.g., nutrients, oxygen) across the SWI. Semi-automated programs (Gordon et al. 2012; Irvine et al. 2015) have been developed that are capable of calculating vertical flows for large data sets using one-dimensional analytical solutions to the heat transport equation (Hatch et al. 2006; Keery et al. 2007; McCallum et al. 2012; Luce et al. 2013). Additionally, with temperature being a relatively easy and inexpensive measurement to conduct, the use of heat as a tracer for calculating vertical velocities and diffusion coefficients in streambed environments is gaining popularity.

Conversely, the use of heat transport methodologies in coastal marine sediments is more limited. With the exception of two coastal, permeable sediment applications (Fram et al. 2014; Savidge et al. 2016; Wilson et al. 2016), such research has focused primarily on quantifying submarine groundwater discharge (e.g., Taniguchi 2000; Moore et al. 2002; Befus et al. 2013). Wilson et. al (2016) and Savidge et al. (2016) developed and applied inverted temperature time-

series measurements to estimate the depth and extent of hydrodynamic exchange below the SWI in a sandy sediment of the South Atlantic Bight. Fram et al. (2014) used a vertically stacked array of thermistors to measure temperature variations in permeable sediments on the south shore of Oahu, Hawaii at 12-m depth. Fram et al. (2014) identified lagged and attenuated temperature signals, and a trend of increasing phase lag with depth below the SWI; however, they did not compute vertical velocities and diffusivities. The primary motivation for the current study is to estimate vertical porewater velocities and diffusivities from high-resolution temperature data collected from an array of buried thermistors

An important distinction between marine and stream/aquifer environments is that temperature variations in marine environments are not necessarily dominated by diurnal heating. Fram et al. (2014) demonstrated that energetic non-diurnal fluctuations occur at their study site, associated with internal tides, shoaling bores, eddies, and other processes. Therefore, isolation of a temperature signal at a single frequency may exclude important information available across a broader range of frequencies. In addition, the dataset collected by Fram et al (2014) featured periods of weak diurnal signal, presumably due to cloudy conditions and other dynamic effects, such as variable diurnal wind forcing or diurnal internal tides (Smith et al. 2017). Preliminary results that we obtained from the Fram et al. (2014) dataset were particularly sensitive to standard filtering methods during these periods of weak diurnal signal.

In this study, a method is developed using a statistical solution to the one-dimensional heat transport equation to estimate values for vertical thermal front velocity and effective thermal diffusivity using unfiltered temperature time-series from an array of buried thermistors. Vertical porewater velocities are then obtained after applying known sediment thermal parameters. The presented method uses unfiltered temperature data to avoid potential problems associated with

isolating a single temperature frequency in environments where changes in temperature structure reflect a variety of processes. Unlike frequency-dependent analytical solutions, the proposed method allows for calculation of porewater velocities when processes such as cloud cover, rain input, or snowmelt mask the usually dominant signal. The method is assessed using temperature time-series data from diurnally dominated streambed environments, and a nearshore marine sediment.

3.3 Procedures and datasets

3.3.1 The heat transport equation

The transport of heat in a saturated porous medium has been examined by Stallman (1965) and others based on a one-dimensional (1-D) heat transport equation (HTE) of the form

$$\frac{\partial T}{\partial t} = D \frac{\partial^2 T}{\partial z^2} - v \frac{\partial T}{\partial z},$$
(3.1)

where T is temperature; t is time; z is depth below the SWI; D is the effective thermal diffusivity; and v is thermal front velocity, specified here as positive into the sediment (See Table 3.1 for a list of symbols). Application of Equation (3.1) assumes that the horizontal heat transport is negligible compared to the vertical transport, fluid and solid temperatures are in local thermal equilibrium, and thermal and textural properties of the fluid and medium remain constant (Stallman 1965).

For a saturated porous medium, v explains thermal front velocity as heat travels through the saturated sediment matrix and is transported with the movement of the fluid in the bed, and is related to q, the specific discharge (or Darcy velocity), by

$$v = \frac{\rho_w c_w}{\rho c} q \, , \tag{3.2}$$

where $\rho_w c_w$ is the specific volumetric heat capacity of water, and ρc is the bulk heat capacity (Rau et al. 2012), defined as

$$\rho c = n\rho_w c_w + (1 - n)\rho_s c_s \, , \tag{3.3}$$

where n is the porosity, and $\rho_s c_s$ is the specific volumetric heat capacity of the solids (Buntebarth and Schopper 1998).

The porewater velocity, v_{pw}, in a saturated sediment is given by

$$v_{pw} = \frac{q}{n} \, . \tag{3.4}$$

From Equations (3.2) and (3.4), it follows (Rau et al. 2012) that

$$v_{pw} = v \frac{\rho c}{\rho_w c_w n}. \tag{3.5}$$

For a saturated porous medium, Rau et al. (2012) (adapted from Green et al., 1964) expressed the effective thermal diffusivity (D, also referred to as the thermal dispersion coefficient) in terms of the thermal diffusivity (the first term) and the thermal dispersivity (the second term):

$$D = \frac{\kappa}{\rho c} + \beta(|v|)^{\gamma}, \tag{3.6}$$

where κ is the bulk thermal conductivity, β is the thermal dispersivity coefficient in the direction of fluid flow, and γ is a power law coefficient. κ is defined as

$$\kappa = \kappa_w^n \cdot \kappa_s^{1-n}, \tag{3.7}$$

where κ_w and κ_s are the thermal conductivities of the water and solids, respectively (Woodside and Messmer 1961). Throughout this paper, Equation (3.6) is referred to as the dispersivity-velocity power law relationship.

Alternatively, Bons et al. 2013 used a unified expression for the normalized effective diffusivity of heat (h) or solutes (s)

$$\frac{D_{h,s}}{D_{h,s\,ref}} = \alpha Pe_{h,s}, \tag{3.8}$$

where $D_{h,ref}$ is conduction of the saturated sediment matrix ($k/\rho c$), $D_{s,ref}$ is the diffusion coefficient of the solute in the porewater, α is the thermal dispersivity coefficient, and Pe is the Péclet number of heat (h) or the solute (s), defined as

$$Pe_{h,s} = \frac{v_{pw}L}{D_{h,s\,ref}}, \tag{3.9}$$

where *L* is the characteristic length scale (e.g., Bear 1972; de Marsily 1986). The characteristic length scale for this study is the length of the thermistor array used. The transport regime is theoretically considered to be convection/advection dominated over the scale of the characteristic length for *Pe* > 1, and conduction/diffusion dominated for *Pe* < 1. Throughout this paper, Equation (3.8) is referred to as the normalized dispersivity-Péclet number relationship. Two symbols are used for dispersivity coefficients, *β* (in Equation 3.6) and *α* (in Equation 3.8), to distinguish between the proposed dispersivity relationships.

Methods for estimating *v* and surface water-groundwater interactions using analytical solutions to the 1-D HTE (Equation 3.1) and a sinusoidal surface-temperature signal have been previously developed by Stallman (1965), Hatch et al. (2006), Keery et al. (2007), McCallum et al. (2012), and Luce et al. (2013). In these approaches, the phase shift and amplitude attenuation of the diurnal component of the sinusoidal signal are calculated from a pair of thermistors. The components of the sinusoidal signal are then used in analytical solutions of Equation (3.1) to quantify *v*. Analytical solutions for *v* (Equation 3.1) are expressed in either terms of amplitude attenuation, in terms of phase shift, or a combined solution in terms of both amplitude attenuation and phase shift. Solutions expressed in terms of only amplitude attenuations or phase shift require estimations of *D,* while solutions in terms of both are inclusive of *D*.

3.3.2   *Statistical solution for D and v*

We propose an alternative approach for estimating *D* and *v* that avoids using analytical solutions of Equation (3.1) (Hatch et al. 2006; Keery et al. 2007; McCallum et al. 2012; Luce et al. 2013), which we find to be highly sensitive for the weak temperature variations observed in the marine sediments at KN. We take advantage of the depth-time sampling provided by the miniTchain (Fram et al. 2014) and solve the partial derivatives in Equation (3.1) using finite

differences in time and a regression fit of basis functions in depth. An array of five evenly-spaced thermistors is used, although the method can be adapted to as few as three sensors.

The time-depth temperature data are referenced as $T(t_i, z_j)$ where i is the timestep from 1 to the total number of hours in the data record, and j is the thermistor number (from 1 to 5), where $j = 1$ for the sensor closest to the SWI. The solution to Equation (3.1) is centered on the middle thermistor, z_3. To compute dT/dt in Equation (3.1), we first construct a weighted depth-average of T centered on z_3, or

$$\bar{T}(t_i, z_3) = 0.08\big(T(t_i, z_1) + T(t_i, z_5)\big) + 0.23(T(t_i, z_2) + T(t_i, z_4)) + 0.38\, T(t_i, z_3) \quad (3.10)$$

dT/dt is then formed using the central difference:

$$dT/dt(t_i, z_3) \;=\; (\bar{T}(t_{i+1}, z_3) - \bar{T}(t_{i-1}, z_3))/(2 * \Delta t), \quad (3.11)$$

with $\Delta t = 3600$ s. The first and second partial derivatives with respect to depth in Equation (3.1) are computed by fitting three orthogonal basis functions to the temperature-depth profile at each timepoint, namely a depth-uniform constant, $z\text{-}z_3$, and $(z\text{-}z_3)^2$. At each time step, a least squares fit provides coefficients, b_0, b_1, and b_2, that are used to estimate $d^2\,T/d\,z^2 = 1/2b_2$, $dT/dz = b_1$,, and the depth-averaged $T = b_0$ for the temperature-depth profile.

After directly calculating the partial derivatives of the HTE, an ordinary least square regression is constructed with the observed dT/dt as the output, and the time series of d^2T/dz^2 and dT/dz as the inputs. A least-squares fit yields the coefficients for the two inputs, the effective thermal diffusivity (D) and thermal front velocity (v). The regressions are performed using three-

hour time steps with a two-day window centered around the time step. The 95% confidence intervals (CI) for D and v are computed assuming an independent data point every 3 hours. A three-hour time step was required to avoid correlation between data points in the temperature-depth time series, and was determined using decorrelation time scale estimates from autocorrelation functions. A two-day window was chosen to include enough independent measurements to minimize the errors in the estimates of D and v while allowing for the temporal resolution needed to investigate the effects of changing water column hydrodynamics.

The model outputs for D and v can be used to evaluate the coefficients in the power law dispersivity relationship in Equation (3.6), as well as the dispersivity coefficient in the unified solute/heat Péclet number relationship (Equation 3.8). We solve Equation (3.6) iteratively by specifying γ and solving for the thermal sediment diffusivity term $\left(k/\rho c \right)$ and the thermal dispersion coefficient (β) as the intercept and slope of a least-squares fit, respectively, for model outputs of D and v. We repeat this over a range of γ values and choose the solution that yields the minimum least-square error over all iterations. Next, the model outputs for D and v are used to find the slope of the least-squares fit to Equation (3.8), which is the dispersivity coefficient (α) of the unified solute/heat-Péclet number relationship.

In Section 3.4, we apply the model to estimate D and v values for two types of sediment temperature time series: 1) streambed temperature data previously analyzed by Gordon et al. (2013), and 2) coastal marine temperature data collected on the south shore of Oahu, Hawaii and analyzed in Fram et al. (2014). Descriptions of those datasets follow.

3.3.3 *Datasets*

Previously published time series of temperature collected from streambed environments were provided by R.P. Gordon. Streambed temperature profiles (TPs) were collected in summer

and fall 2009 and 2010 from Boyer Creek and Nine Mile Creek in central New York (Gordon et al. 2013). The sediment was similar at all sites and consisted of gravel and cobbles, with some silt and sand. Temperature was recorded using iButton temperature sensors and loggers (0.0625 °C resolution, 0.5 °C accuracy) at 10-minute intervals. Vertical TPs were measured using temperature sensors fixed to a buried rod at 5, 10, 15, 20, 25, and 30 cm below the SWI. Vertical TPs were analyzed using the VFLUX2 program (Gordon et al., 2012) to compute estimates of vertical seepage flux (q) for each study site using the Hatch et al. (2006) amplitude method. Of the 41 streambed TPs provided, 30 TPs met the evenly-spaced thermistor criterion for the assessment of the statistical solution to the HTE.

Time series temperature measurements from a marine environment were collected at the Kilo Nalu Nearshore Reef Observatory (Kilo Nalu, KN) in Mamala Bay, Oahu, Hawaii (Figure 3.2). We seek to provide the first v and D estimates from this dataset to extend the work of Fram et al. (2014). Kilo Nalu is a benthic observatory located in 12-m water depth about 400 m from shore (Sansone et al. 2008; Pawlak et al. 2009). The sediment at Kilo Nalu consists of a well-sorted fine to medium carbonate reef sand (125−500 µm) with less than 1% fines (Fogaren et al. 2013). The sediment permeability, using the Carmen-Kozeny equation, and the sediment porosity, were previously determined to be ~8.8 × 10^{-11} m^2 and 0.49, respectively (Hebert et al. 2007).

Temperature measurements at Kilo Nalu were made using a miniature thermistor chain (miniTchain). The miniTchain recorded coincident time series of temperature (0.002 °C accuracy) at 2-minute sample intervals just above the SWI and at fixed positions within the upper ~ 20 cm of sediment (Figure 3.3). The sensor configuration was ten thermistors vertically stacked in a main spine, and five thermistors vertically stacked in a side spine, positioned 90°

from the main spine. The top five thermistors of the main spine (the "Main" array) and side spine (the "Side" array) were spaced every 1.5 cm, while the bottom five thermistors of the main spine (the "Deep" array) were spaced every 2.0 cm. The average depth of the center thermistor of the Main and Side arrays was 10 cm below the SWI, while the average depth of the center thermistor of the Deep Array was 19 cm below the SWI. Fram et al. (2014) provide a detailed description of the miniTchain.

3.4   Results and Discussion

We apply the HTE statistical model to the streambed and Kilo Nalu datasets and assess the results in three ways:

1) Model skill: we compute the coefficient of determination (R^2), the p-value, the root mean square error (RMSE), and the bias between the observed and model-estimated dT/dt.

2) Comparison with VFLUX2: for the streambed data, we compare times series of D and v from the second version of the Vertical Fluid Heat Transport Solver, VFLUX2, with our statistical model results. The correlation coefficient (r^2), the p-value, the RMSE and the bias are used to compare statistical and analytical outputs of D and v for these datasets. We were not able to obtain stable VFLUX2 solutions for the KN data.

3) Relationship between v and D: we evaluate relationships between v and D using both the statistical and VFLUX2 results. Statistical results are then evaluated through the proposed 1) dispersivity-velocity power law relationship in Equation (3.6), and the 2) normalized dispersivity-Péclet number relationship in Equation (3.8).

   VFLUX2 is a MATLAB toolbox that uses temperature time series and user-input sediment and water thermal characteristics to estimate Darcy velocities (q) and effective thermal diffusivities (D) based on different analytical solutions to the 1-D HTE Equation (3.1) (Gordon

et al. 2012; Irvine et al. 2015). The program calculates signal lags and/or amplitude attenuations between pairs of thermistors at a single, isolated frequency of the temperature signal. The resulting time series of signal lags and/or amplitude attenuations is then applied to one of the analytical solutions to the 1-D HTE (Hatch et al. 2006; Keery et al. 2007; McCallum et al. 2012; Luce et al. 2013). The analytical solutions of McCallum and Luce in VFLUX2 are identical and require both the phase lag and amplitude attenuation of the signal, producing estimates of both D and v. That is the solution used for comparisons in this study. Other solutions return v for user-estimated values of D.

3.4.1   Streambed temperature data

3.4.1.1   Model skill

Time series of observed and modeled dT/dt for one of the streambed datasets illustrates the ability of the model to capture observed changes (Figure 3.4). The coefficients of determination (R^2) range from 0.284 to 0.995 (Table 3.2). The dataset presented in Figure 3.4 is an example of a high skill result ($R^2 > 0.90$, met by 26 of 30 datasets; indicated in Table 3.2). In this figure, we show the dT/dt contributions from the D and v components, which reveals the D term contribution is 7.8% of the v term contribution. For the four low skill datasets ($R^2 < 0.75$, see Appendix B), the average temperature difference between each thermistor in the TP was below the reported accuracy of the temperature sensors (0.5 °C), likely resulting in the poor fit between the field and model data.

3.4.1.2   Comparative assessment

We next compare our estimates of D and v with those obtained from the McCallum/Luce solution using VFLUX2. The VFLUX2 toolbox requires temperature recordings from two thermistors to calculate q and D, and reports outputs for q and D as the depth-average value

between the two thermistors. Therefore, we use the first and fifth buried thermistors for comparison with results computed using our statistical model. The VFLUX2 results are comparable to our statistical results because both are representative of the center of the five-required thermistors. For the purpose of comparison we converted the VFLUX2-generated q to v (Equation 3.2) using the values of sediment thermal and textural properties provided in Table 2 of Gordon et al. (2013). For four of the freshwater data sets, VFLUX2 was unable to calculate solutions. These data sets and the four data sets that were not well explained by our statistical solution ($R^2 < 0.75$) were not included in the comparative assessment of the two methods. The remaining 22 datasets were used in the comparative assessment of the two methods.

Time series of temperature profiles and the statistical model estimates of D and v, along with 95% CIs, for all streambed temperature data collected at Boyer and Nine Mile Creeks are available in Appendix B. Analytical estimates of D and v (from VFLUX2) are also shown for comparison. Additionally, time series of observed and statistically modeled dT/dt are also available in Appendix B. With the true v and D values unknown, outputs from the two solutions were compared statistically using r^2, p-value, RMSE, and bias metrics (Table 3.3).

Results of the comparative assessment of D and v values from the two methods are mixed (Table 3.3). The correlation (r^2) for D values ranged from 0 to 0.906, and ranged from 0.001 to 0.829 for v values. Correlations were statistically significant ($p < 0.05$) for 17 of the 22 D-value comparisons and 13 of the 22 v-value comparisons. Statistical outputs for D values resulted in generally positive biases compared to the analytical solution for D values. No overall positive or negative bias between the solutions was revealed for v.

3.4.1.3   Theoretical assessment

We next evaluate the relationship between D and v from in our statistical model outputs for which $R^2 > 0.90$. In general, the TPs at Boyer Creek and Nine Mile Creek (Figure 3.5A) show that D increases as $|v|$ increases, as expected from Equations (3.6) and (3.8). There are a few exceptions: two TPs (TP06 at Boyer Creek, TP04 at Nine Mile Creek) show an increase in diffusivity with decreasing $|v|$, and show a high offset relative to the other TPs. We do not know the reasons for these discrepancies.

In contrast, the VFLUX2 estimates of D and $|v|$ for the same stream data do not show as clear of a relationship as the statistical model results (Figure 3.5B), and show considerable scatter for all TPs. The VFLUX2 outputs have a larger number of TPs that show decreasing D's for increasing $|v|$ than do statistical model outputs.

3.4.1.4   The dispersivity-velocity relationship

There has been much debate in the literature regarding the significance of the thermal dispersivity term, and its relationship to thermal front velocity (e.g., Lu et al. 2009; Rau et al. 2012, 2014). Our statistical solution method bypasses both these issues by 1) solving directly for D, which includes both the thermal sediment diffusivity and dispersivity terms (Equation 3.6); and 2) then using Equations (3.6) and (3.8) with outputs of D and v to investigate the dispersivity-velocity relationship. Outputs of D and v from our statistical solution are then used to empirically determine the γ exponent and the β coefficient in Equation (3.6), and the α coefficient in Equation (3.8).

Using our v and D estimates from all the stream data, we find that the dispersivity-velocity relationship proposed in Equation (3.6) is optimized using a γ exponent of 0.98 (Figure 3.6A; $R^2 = 0.91$, n = 2105). A γ exponent of 0. 98 is consistent with both the 0.9 value suggested

by Lu et al. 2009, and the linear relationship suggested by numerous authors (e.g., Anderson 2005; Hatch et al. 2006; Keery et al. 2007). In contrast, the thermal diffusivity of the sediments is estimated as 0.1196 m^2d^{-1} (95% CI, 0.1175-0.1217), which is ~50% larger than the thermal diffusivity of 0.0779 m^2d^{-1} (range of 0.0643 – 0.0927 m^2d^{-1}) calculated from the reported sediment properties in Table 2 of Gordon et al. 2013. The best fit for the β coefficient is 0.068 m (95% CI, 0.0677-0.0695), which is different than the estimated β coefficient of 0.001 m used for Boyer and Nine Mile Creeks.

Differences between our statistically-derived estimates and reported values for the thermal sediment diffusivity and the β coefficient may result from the assumption that the sediment is the same for all datasets at the two creeks. While the approximations used by Gordon et al. (2013) for sediment textures and parameters are reasonable estimates, it is unlikely the sediment properties were identical at all the TPs at both creeks. To investigate the effect of this potential sediment heterogeneity on the thermal dispersivity-velocity relationship in Equation (3.6), γ exponents, β coefficients and thermal diffusivity terms were determined after grouping TPs by site location and year (Figure 3.6B-D). The slightly different γ exponents, β coefficients, and thermal sediment diffusivity estimates for Boyer Creek, Nine Mile Creek in 2009, and Nine Mile Creek in 2010 suggest that the sediment characteristics were not consistent.

The scatter in effective thermal diffusivity (a combination of thermal sediment diffusivity and dispersivity terms) at small thermal front velocities may be due to lateral sediment heterogeneity within each site. At zero or very weak thermal front velocities, the effective thermal diffusivity is solely due to the thermal sediment diffusivity (Equation 3.6). As thermal front velocities increase, the increase in D due to the dispersivity depends on the sediment characteristics, with heterogenous sediments associated with more dispersivity (Lu et al. 2009).

As a result, the lateral variability in sediment characteristics at each site will result in a different linear relationship (slope and intercept) for values of D and v for each TP. This is best illustrated in the slightly different regression slopes (dispersivity coefficients, β) and intercepts (thermal sediment diffusivities) that are calculated for values of D and v from each of the TPs at Nine Mile Creek in 2009 (Figure 3.6C).

Next, we used our v and D estimates, an estimated sediment thermal diffusivity ($D_{h,ref}$) of 0.1196 m^2d^{-1} (see above), and a characteristic length (L) of 0.20 m, the distance between thermistors z_1 and z_5, to determine a α coefficient of 0.23 ($R^2 = 0.490$) that describes the normalized dispersivity-Péclet number relationship of Equation (3.8) using all the stream data (Figure 3.7A). Similarly to dispersivity coefficients (β) determined from dispersivity-velocity power law relationships, slightly different dispersivity coefficients (α) were determined as a function of Péclet number after grouping TPs by site location and year (Figure 3.7B-D). α coefficients were determined to be 0.12 ($R^2 = 0.967$), 0.28 ($R^2 = 0.768$), and 0.32 ($R^2 = 0.901$) for Boyer Creek, Nine Mile Creek in 2009, and Nine Mile Creek in 2010, respectively (Table 3.4).

Bons et al. (2013) demonstrated that the determination of the dispersivity coefficient (α) in terms of Pe allows for a unified expression for heat and solute dispersivity, in which dispersivity can be described over a large range of Pe values. As a result, the effective solute diffusivity (D_s) can be calculated using the α coefficient that describes the normalized thermal dispersivity-Péclet number relationship. This is useful because the same porewater velocity will result in different Péclet numbers for solutes and heat (Equation 3.9). The different Pe_s and Pe_h numbers for the same porewater velocity, v_{pw}, result from conductive heat transfer through both the solid and fluid parts of the saturated matrix, while solute diffusion occurs through just the

fluid phase, resulting in $D_{h,ref}$ being several orders of magnitude larger than the $D_{s,ref}$. Application of this unified solute/heat dispersivity-Péclet number relationship will be demonstrated using Kilo Nalu data, below.

3.4.2   Kilo Nalu temperature data

3.4.2.1   Model skill

Time series of observed and modeled dT/dt for the Kilo Nalu Deep Array illustrates the ability of the model to capture the observed changes (Figure 3.8A). Using the entire 80-day dataset, the model resulted in R^2 values of 0.81, 0.54, and 0.88 (n = 623) for the Main, Side and Deep Arrays of the miniTchain, respectively (Table 3.2).

Investigation into values of D and v from all arrays that resulted in poor model performance revealed D values that are theoretically impossible and therefore invalid solutions to the HTE (see Theoretical assessment below). While investigating a low skill time-period of the model results from the Side Array, it was discovered that the uppermost part of the miniTchain was scoured out of the sediment, and one or more of the thermistors from the Side Array was recording water-column temperatures. With the theoretically invalid results and scoured-out time period removed, the model skill improved with R^2 values for the Main, Side and Deep of 0.89 (n = 541), 0.91 (n = 565), and 0.90 (n = 567), respectively (Table 3.2).

The week-long period presented in Figure 3.8B is an example of high model skill. For the presented time period, the dT/dt contributions from the D and v components are shown, with the v-term contribution being about 11.6% of the D-term contribution (Figure 3.8C). We found the contribution of the D term to dT/dt is much larger than the v-term contribution, in contrast to the high skill freshwater example (Figure 3.4). Over the entire deployment for the Deep Array, the v-term contribution was about 23% of the D term contribution to dT/dt.

3.4.2.2   Theoretical assessment

To evaluate the relationship between D and v, all model outputs from Kilo Nalu were used (Figure 3.9). In general, the Kilo Nalu arrays showed the expected increase in D as $|v|$ increases. Violations of the increase in D with an increase in v were found to occur when the values for D were below the estimated thermal diffusivity of the sediment at Kilo Nalu, 0.018 m^2d^{-1}. With no thermal front velocity ($v = 0$), the D term is equal to the thermal diffusivity of the sediments (Equation 3.6). Therefore, the thermal diffusivity of the sediment was estimated as the intercept of the D-v relationship the Deep Array. Values of D and v from the Deep Array were used because they had the strongest D-v relationship ($R^2 = 0.863$). It is theoretically impossible to have values for D less than the thermal diffusivity of the sediments. As a result, D values less than the thermal diffusivity of the sediments, and their corresponding v values, were removed as invalid solutions to the 1-D HTE and excluded from the analysis below. In Figure 3.8A, gaps in the time series of modeled dT/dt (red line) represent time periods of theoretically invalid model results. Values of model skill (R^2) for the Main, Side and Deep Arrays after the theoretical assessment are shown in Table 3.2.

3.4.2.3   The dispersivity-velocity relationship

The dispersivity-velocity power law relationship predicted in Equation (3.6) was assessed for each array once the theoretically impossible outputs for Kilo Nalu were removed (Table 3.4). For the Main Array, a γ exponent of 3.3 was used to optimize the weakly positive dispersivity-velocity relationship ($R^2 = 0.182$, n = 541; Figure 3.10A). For the Side Array, a weakly positive dispersivity-velocity power law relationship ($R^2 = 0.28$, n = 565) was optimized with a γ term of 1.97 (Figure 3.10B). The strongest dispersivity-velocity power law relationship ($R^2 = 0.88$, n = 567) was determined for the Deep Array with a γ term of 1.5 (Figure 3.10C). Using data from all

arrays, the dispersivity-velocity power law relationship was optimized with a γ term of 2.04 (R^2 = 0.49, n = 1673, Figure 3.10D).

Next, the normalized dispersivity as a function of the Péclet number (Equation 3.8) was assessed for each array once the theoretically impossible outputs for Kilo Nalu were removed (Figure 3.11). Again, the weakest relationship was observed for the Main Array (Figure 3.11A, R^2 = 0.11), followed by the Side Array (Figure 3.11B, R^2 = 0.27), with the strongest relationship for the Deep Array (Figure 3.11C, R^2 = 0.93). Péclet number calculations revealed that for porewater velocities at the Main Array, an average Pe of 0.31 $\pm$ 0.37 was observed, with Pe > 1 only 5.3 % of the time. Similarly, for the Side Array, an average Pe of 0.61 $\pm$ 0.34 was observed, with Pe > 1 during 12.2% of the deployment. Lastly, an average Pe of 1.13 $\pm$ 0.70 was calculated for the Deep Array, with Pe > 1 during 43.2 % of the time.

The normalized dispersivity-Péclet number relationships at Kilo Nalu reveal that dispersivity starts to increase as a function of Péclet number before the theoretically critical Pe > 1 (dashed lines Figure 3.11) is reached. However, this is not unexpected because experimental work has revealed that diffusion dominates for Pe < 0.1-0.3 (dotted lines, Figure 3.11), diffusion and dispersion dominate for 0.3 < Pe < 5, and advection dominates for Pe > 5 (Bons et al. 2013). The weak dispersivity relationship for the Main Array likely results from the fact that over half the Pe numbers fall into the diffusion-dominated transport regime (Pe < 0.3). This may also explain the larger γ exponent needed to optimize the dispersivity relationship proposed in Equation (3.6) compared to the Side and Deep Arrays. A stronger dispersivity relationship for the Side Array likely results in Pe > 0.3 for ~ 80% of the deployment. The strong dispersivity relationship observed at the Deep Array occurs because diffusion and dispersion dominate the transport regime, with Pe > 0.3 during 97% of the entire deployment. The outputs from the

statistical solution to the HTE at Kilo Nalu fit well with findings from other dispersion-velocity studies, which revealed that dispersivity is not a significant component of D until a Pe threshold of 0.1-0.3 has been reached (Bons et al. 2013).

The normalized dispersivity as a function of Péclet number in Equation (3.8) is useful because it is a unified expression for both heat (h) and solutes (s). Thus, the α coefficient determined from the relationship between normalized thermal dispersivity, $D_h/D_{h,ref}$, and thermal Péclet number, Pe_h, can be used to calculate the normalized effective diffusivity for a solute, $D_s/D_{s,ref}$, in the same sediment. This is demonstrated for the Deep Array in Figure 3.12. First, model values of D are normalized using the estimated sediment diffusivity, $D_{h,ref}$, value of 0.018 $m^2 d^{-1}$, and Pe_h numbers are calculated using a characteristic length (L) of 0.08 m. From the regression of $D_h/D_{h,ref}$ as a function of Pe_h, a dispersivity coefficient, α, of 0.39 is determined (Table 3.4). Because Equation (3.8) can be used for both heat and solute, the dispersivity coefficient, α, determined for the thermal relationship can also be used to describe $D_s/D_{s,ref}$, as a function of the solute Péclet number, Pe_s. Additionally, the unified expression in Equation (3.8) is valid for a large range of Péclet numbers, or transport regimes, which is important because much larger Péclet numbers result for solutes than for heat under the same flow conditions. For example, for dissolved oxygen at the Deep Array ($L = 0.08$ m), a v_{pw} of 0.15 m d^{-1} results in a Pe_h of ~0.67 and a Pe_S of ~126. Calculated using the α coefficient determined for the Deep Array, projected values of $D_s/D_{s,ref}$ as a function of Pe_S are indicated with a dashed line in Figure 3.12.

3.4.2.4 Vertical porewater velocities

Time-series of v and D outputs for the 80-day deployment at Kilo Nalu are shown in Figure 3.13. Model outputs that were theoretically impossible were removed. Values for D and v

are reported for the center depth for each temperature array, despite changes in relative depth to the SWI sediment due to processes such as ripple migration and sediment scouring. However, except for thermistor exposure in the overlying water column, slight changes in sediment cover should not have a large effect on D and v values since they are calculated over the length of an array.

Throughout the 80-day deployment, D values are relatively consistent for all arrays, with a mean value of 0.026 ± 0.0044 m^2 d^{-1}. Consistent D values likely result from the dominating contribution of the thermal sediment diffusivity term (~ 0.018 m^2 d^{-1}), with relatively small contributions from the thermal dispersivity term to the computed v values.

Values of v are converted to v_{pw} using Equation (3.5). With the speed of v retarded because of the heat capacity of the sediments (Rau et al. 2012, 2014), v_{pw} values are proportional to v values; therefore, trends for v and v_{pw} are similar. Vertical v_{pw} are shown for the 80-day deployment at Kilo Nalu in Figure 3.14. Mean v_{pw} for the Main, Side and Deep Arrays are 0.055 ± 0.13 m d^{-1}, $- 0.17 \pm 0.12$ m d^{-1}, and $- 0.25 \pm 0.16$ m d^{-1}, respectively, with negative velocities moving upwards towards the SWI and positive velocities moving downwards into the bed. The mean porewater magnitude, $|v_{pw}|$, for the Main, Side and Deep Arrays are 0.094 ± 0.11 m d^{-1}, 0.18 ± 0.10 m d^{-1}, and 0.25 ± 0.16 m d^{-1}.

Comparisons of porewater velocities computed from the three arrays reveal that fluid flow in the sediment may not have been solely in the vertical. The values of $|v_{pw}|$ computed from arrays at Kilo Nalu reveal that larger vertical porewater magnitudes occurred at 19 cm below the SWI (Deep Array) than at 10 cm below the SWI (Main and Side Array). This is unusual because models suggest that the strength of advective flows will decrease with increasing depth from the SWI (Shum 1992; Huettel et al. 1996; Precht and Huettel 2003). However, these models are

multidimensional and include lateral components of fluid flow in the sediment that we cannot capture using vertically-stacked thermistors. Lateral fluid flow in permeable sediments results from the development of pressure gradients, and has been demonstrated in flume experiments (e.g., Precht and Huettel 2004; Huettel et al. 2014) and porewater transport models (e.g., Webb and Theodor 1968; Shum 1992). Pressure gradients can develop as bottom currents move over small topographic features, such as sand ripples (Santos et al. 2012b). As a result, bottom water enters the sediment at areas of high pressure, and flows in multiple directions toward areas of low pressure, where it is released to the overlying water column (Huettel et al., 1996; Huettel and Rusch, 2000). Stronger pressure gradients that exist closer to the SWI may result in a larger component of lateral porewater flow closer to the SWI than deeper in the sediment, and may explain the weaker vertical flows at 10 cm (Side and Main Array) than at 19 cm (Deep Array).

This multidimensional flow field in the upper sediment may also explain differences in the means and magnitudes of vertical porewater velocities computed for the Side and Main Array, both located at ~10 cm below the SWI. The 90° offset between the Side and Main Array was designed to be approximately the length of a sand ripple at Kilo Nalu (~ 20 cm) to simultaneously capture temperature changes resulting from flow into the sediment at a ripple trough and out of the sediment at a ripple crest (Fram et al. 2014). Fram et al. (2014) were not able to discern any measurable difference in temperature at the Main or Side Array as a function of ripple height, presumably due to difficulties measuring the chaotic ripple formations at Kilo Nalu. Thus, differences in computed porewater velocities for the Side and Main Array may also result from complex 3-D porewater flow in the sediment not captured by our vertically-stacked arrays. Furthermore, with the Side and Main Array offset at the same depth below the SWI, the

horizontal component of porewater flow interacting with the buried structure of the upstream array could have altered the hydrodynamics for the downstream array.

Mean porewater velocities computed for Kilo Nalu suggest that over the entire deployment there was overall net flow out of the sediment. This is unusual because the overall flow of water into the sediment at ripple troughs is expected to be balanced by the overall flow of water out of the sediment at ripple crests. Therefore, the observed overall flow out of the sediment could be indicative of a larger scale flow process, such as submarine groundwater discharge, although previous porewater salinity measurements indicated no obvious interaction between the porewater and a freshwater source at Kilo Nalu (Fogaren et al. 2013). However, while salinity measurements indicated no fresh groundwater input to the system, they do not exclude the possibility of seepage from saline or brackish sources (Moore et al. 2002).

MiniTchain experiments were conducted in a ~70 m wide sand patch that is part of a larger coral reef framework. Like permeable sediments, the reef framework is also subject to hydraulically-driven advective flows, with flow traveling preferentially along high permeability zones such as cavities and rubble (Parnell 2011). As a result, the larger scale internal circulation of water through the adjacent coral reef framework could also be responsible for the observed net flow out of the sediment.

3.5   Conclusions

The proposed method solves the 1-D heat transport equation (HTE) using finite differences and regression fits calculated from a time series of temperature profiles in a sediment. The method is demonstrated using five evenly-spaced thermistors. Since miniTchain thermistors are relatively fixed, no adjustments to individual thermistor spacing due to ripple migration or sediment scouring was required. Most importantly, the proposed method does not

require that the data be filtered at a dominant frequency. The unfiltered data allow for application of the method in environments with temperature signals made up of different frequency components, such as in coastal marine sediments. Additionally, the use of unfiltered temperature allows for the calculation of thermal front velocities, and subsequent Darcy and porewater velocities, during time periods when the dominant, usually diurnal, signal is weak.

One of the strengths of the method proposed here is that it does not require any prior knowledge of sediment characteristics or an estimation of the dispersivity coefficient to statistically solve for the thermal front velocity and the effective thermal diffusivity. Furthermore, outputs for D and v can be used to statistically evaluate the significance of the dispersivity term and its proposed relationship to effective thermal diffusivity and thermal velocity.

The proposed method was assessed statistically, comparatively, and theoretically using streambed and nearshore permeable sediment temperature profiles. The modeled outputs for thermal front velocity and effective thermal diffusivity demonstrated high model skill between the observed and modeled rate of temperature change for both the streambed and nearshore environments. However, the proposed method did an overall better job of explaining the observed field data for the stream data than for the nearshore data (Table 3.2). This may be due to 1) complexities in the nearshore temperature profiles as a result of the additional frequencies of the temperature signal; 2) the small marine temperature changes (despite the use of high precision thermistors); and/or 3) the possibility that porewater flow in marine environments may include a stronger lateral component of flow than in the freshwater environments, violating the vertical-flow assumption of the 1-D HTE.

With actual porewater flows and values of effective diffusivity unknown, the importance of assessing solutions to the 1-D HTE was demonstrated in order to ensure high skill, theoretically possible solutions. The importance of theoretically assessing solutions to the 1-D HTE was demonstrated by flagging otherwise reasonable outputs as impossible solutions. Lastly, while these assessments are vital to the quality assurance of our solutions, further *in-situ* investigations assessing flow measurements using independent techniques are needed to verify our results.

3.6   References

Anderson, M. P. 2005. Heat as a Ground Water Tracer. Groundwater **43**: 951–968. doi:10.1111/j.1745-6584.2005.00052.x

Bear, J. 1972. Dynamics of fluids in porous media., American Elsevier Pub. Co.

Befus, K. M., M. B. Cardenas, D. V. Erler, I. R. Santos, and B. D. Eyre. 2013. Heat transport dynamics at a sandy intertidal zone. Water Resour. Res. **49**: 3770–3786. doi:10.1002/wrcr.20325

Berg, P., H. Røy, F. Janssen, V. Meyer, B. B. Jørgensen, M. Huettel, and D. De Beer. 2003. Oxygen uptake by aquatic sediments measured with a novel non-invasive eddy-correlation technique. Mar. Ecol. Prog. Ser. **261**: 75–83. doi:10.3354/meps261075

Bons, P. D., B. P. Van Milligen, and P. Blum. 2013. A general unified expression for solute and heat dispersion in homogeneous porous media. Water Resour. Res. **49**: 6166–6178. doi:10.1002/wrcr.20488

Boudreau, B. P., M. Huettel, S. Forster, and others. 2001. Permeable marine sediments: Overturning an old paradigm. Eos (Washington. DC). **82**: 133–136. doi:10.1029/EO082i011p00133-01

Briggs, M. a., L. K. Lautz, J. M. McKenzie, R. P. Gordon, and D. K. Hare. 2012. Using high-resolution distributed temperature sensing to quantify spatial and temporal variability in vertical hyporheic flux. Water Resour. Res. **48**: n/a-n/a. doi:10.1029/2011WR011227

Buntebarth, G., and J. R. Schopper. 1998. Experimental and theoretical investigations on the influence of fluids, solids and interactions between them on thermal properties of porous rocks. Phys. Chem. Earth **23**: 1141–1146. doi:10.1016/S0079-1946(98)00142-6

Fogaren, K. E., F. J. Sansone, and E. H. De Carlo. 2013. Porewater temporal variability in a wave-impacted permeable nearshore sediment. Mar. Chem. **149**: 74–84. doi:10.1016/j.marchem.2012.12.005

Fram, J. P., G. R. Pawlak, F. J. Sansone, B. T. Glazer, and A. K. Hannides. 2014. OCEANOGRAPHY : METHODS Miniature thermistor chain for determining surficial sediment porewater advection. 155–165. doi:10.4319/lom.2014.12.155

Gordon, R. P., L. K. Lautz, M. a. Briggs, and J. M. McKenzie. 2012. Automated calculation of vertical pore-water flux from field temperature time series using the VFLUX method and computer program. J. Hydrol. **420**–**421**: 142–158. doi:10.1016/j.jhydrol.2011.11.053

Gordon, R. P., L. K. Lautz, and T. L. Daniluk. 2013. Spatial patterns of hyporheic exchange and biogeochemical cycling around cross-vane restoration structures: Implications for stream restoration design. Water Resour. Res. **49**: 2040–2055. doi:10.1002/wrcr.20185

Goto, S., M. Yamano, and M. Kinoshita. 2005. Thermal response of sediment with vertical fluid flow to periodic temperature variation at the surface. J. Geophys. Res. B Solid Earth **110**: 1–11. doi:10.1029/2004JB003419

Grigg, R. W. 1995. Coral reefs in an urban embayment in Hawaii: a complex case history controlled by natural and anthropogenic stress. Coral Reefs **14**: 253–266.

Hall, S. J. 2002. The continental shelf benthic ecosystem: current status, agents for change and future prospects. Environ. Conserv. **29**: 350–374. doi:10.1017/S0376892902000243

Hatch, C. E., A. T. Fisher, J. S. Revenaugh, J. Constantz, and C. Ruehl. 2006. Quantifying surface water-groundwater interactions using time series analysis of streambed thermal records: Method development. Water Resour. Res. **42**: n/a-n/a. doi:10.1029/2005WR004787

Hebert, A. B., F. J. Sansone, and G. R. Pawlak. 2007. Tracer dispersal in sandy sediment porewater under enhanced physical forcing. Cont. Shelf Res. **27**: 2278–2287. doi:10.1016/j.csr.2007.05.016

Huettel, M., P. Berg, and J. E. Kostka. 2014. Benthic exchange and biogeochemical cycling in permeable sediments. Ann. Rev. Mar. Sci. **6**: 23–51. doi:10.1146/annurev-marine-051413-012706

Huettel, M., and A. Rusch. 2000. Transport and degradation of phytoplankton in permeable sediment. Limnol. Oceanogr. **45**: 534–549. doi:10.4319/lo.2000.45.3.0534

Huettel, M., W. Ziebis, S. Forester, G. W. Luther III, S. Forster, G. W. Luther III, and G. W. Luther. 1998. Advective transport affecting metal and nutrient distributions and interfacial fluxes in permeable sediments. Geochim. Cosmochim. Acta **62**: 613–631. doi:10.1016/S0016-7037(97)00371-2

Huettel, M., W. Ziebis, and S. Forster. 1996. Flow-induced uptake of particulate matter in permeable sediments. Limnol. Oceanogr. **41**: 309–322.

Irvine, D. J., L. K. Lautz, M. A. Briggs, R. P. Gordon, and J. M. McKenzie. 2015. Experimental evaluation of the applicability of phase, amplitude, and combined methods to determine water flux and thermal diffusivity from temperature time series using VFLUX 2. J. Hydrol. **531**: 728–737. doi:10.1016/j.jhydrol.2015.10.054

Janssen, F., M. Huettel, and U. Witte. 2005. Pore-water advection and solute fluxes in permeable marine sediments (II): Benthic respiration at three sandy sites with different permeabilities (German Bight, North Sea). Limnol. Oceanogr. **50**: 768–778. doi:10.4319/lo.2005.50.3.0768

Keery, J., A. Binley, N. Crook, and J. W. N. Smith. 2007. Temporal and spatial variability of groundwater–surface water fluxes: Development and application of an analytical method using temperature time series. J. Hydrol. **336**: 1–16. doi:10.1016/j.jhydrol.2006.12.003

Lu, X., T. Ren, and Y. Gong. 2009. Experimental investigation of thermal dispersion in saturated soils with one-dimensional water flow. Soil Sci. Soc. Am. J. **73**: 1912–1920. doi:10.2136/sssaj2008.0251

Luce, C. H., D. Tonina, F. Gariglio, and R. Applebee. 2013. Solutions for the diurnally forced advection-diffusion equation to estimate bulk fluid velocity and diffusivity in streambeds from temperature time series. Water Resour. Res. **49**: 488–506. doi:10.1029/2012WR012380

de Marsily, G. 1986. Quantitative hydrogeology: groundwater hydrology for engineers, Academic Press.

McCallum, a. M., M. S. Andersen, G. C. Rau, and R. I. Acworth. 2012. A 1-D analytical method for estimating surface water-groundwater interactions and effective thermal diffusivity using temperature time series. Water Resour. Res. **48**: n/a-n/a. doi:10.1029/2012WR012007

Moore, W. S., J. Krest, G. Taylor, E. Roggenstein, S. Joye, and R. Lee. 2002. Thermal evidence of water exchange through a coastal aquifer: Implications for nutrient fluxes. Geophys. Res. Lett. **29**: 44–49. doi:10.1029/2002GL014923

Parnell, K. E. 2011. Internal Circulation, p. 1205. *In* D. Hopley [ed.], Encyclopedia of modern coral reefs: structure, form and process. Springer.

Pawlak, G., E. H. De Carlo, J. P. Fram, and others. 2009. Development, deployment, and operation of Kilo Nalu nearshore cabled observatory. Ocean. 2009-Europe 1–10. doi:10.1109/OCEANSE.2009.5278149

Precht, E., and M. Huettel. 2003. Advective pore-water exchange driven by surface gravity waves and its ecological implications. Limnol. Oceanogr. **48**: 1674–1684. doi:10.4319/lo.2003.48.4.1674

Precht, E., and M. Huettel. 2004. Rapid wave-driven advective pore water exchange in a permeable coastal sediment. J. Sea Res. **51**: 93–107. doi:DOI 10.1016/j.seares.2003.07.003

Rau, G. C., M. S. Andersen, and R. I. Acworth. 2012. Experimental investigation of the thermal dispersivity term and its significance in the heat transport equation for flow in sediments. Water Resour. Res. **48**: 1–21. doi:10.1029/2011WR011038

Rau, G. C., M. S. Andersen, A. M. McCallum, H. Roshan, and R. I. Acworth. 2014. Heat as a tracer to quantify water flow in near-surface sediments. Earth-Science Rev. **129**: 40–58. doi:10.1016/j.earscirev.2013.10.015

Riedl, R. J., N. Huang, and R. Maohan. 1972. The subtidal pump: a mechanism of interstitial water exchange by wave action. Mar. Biol. **13**: 210–221.

Sansone, F. J., G. Pawlak, T. P. Stanton, and others. 2008. Kilo Nalu physical/biogeochemical dynamics above and within permeable sediments. Oceanography **21**: 173–178.

Santos, I. R., B. D. Eyre, and M. Huettel. 2012. The driving forces of porewater and groundwater flow in permeable coastal sediments: A review. Estuar. Coast. Shelf Sci. **98**: 1–15. doi:10.1016/j.ecss.2011.10.024

Savidge, W. B., A. Wilson, and G. Woodward. 2016. Using a Thermal Proxy to Examine Sediment–Water Exchange in Mid-Continental Shelf Sandy Sediments. Aquat. Geochemistry **22**: 419–441. doi:10.1007/s10498-016-9295-1

Shum, K. 1992. Wave-induced advective transport below a rippled water-sediment interface. J. Geophys. Res. Ocean. **97**: 789–808. doi:10.1029/91jc02101

Smith, K. A., M. A. Merrifield, and G. S. Carter. 2017. Coastal-trapped behavior of the diurnal internal tide at O'ahu, Hawai'i. J. Geophys. Res. Ocean. doi:10.1002/2016JC012436

Stallman, R. W. 1965. Steady one-dimensional fluid flow in a semi-infinite porous medium with sinusoidal surface temperature. J. Geophys. Res. **70**: 2821. doi:10.1029/JZ070i012p02821

Taniguchi, M. 2000. Evaluations of the saltwater-groundwater interface from borehole temperature in a coastal region. Geophys. Res. Lett. **27**: 713–716.

Webb, J. E., and J. Theodor. 1968. Irrigation of submerged marine sands through wave action. Nature **220**: 682–683.

Wilson, A. M., G. L. Woodward, and W. B. Savidge. 2016. Using heat as a tracer to estimate the depth of rapid porewater advection below the sediment-water interface. J. Hydrol. **538**: 743–753. doi:10.1016/j.jhydrol.2016.04.047

Woodside, W., and J. H. Messmer. 1961. Thermal Conductivity of Porous Media. I. Unconsolidated Sands. J. Appl. Phys. **32**: 1688–1699. doi:10.1063/1.1728419

Ziebis, W., M. Huettel, and S. Forster. 1996. Impact of biogenic sediment topography on oxygen fluxes in permeable seabeds. Mar. Ecol. Prog. Ser. **140**: 227–237. doi:10.3354/meps140227

Table 3.1: List of symbols used, in order of appearance in text

Symbol	Unit	Description
T	°C	temperature
t	d	time
z	m	depth
D	$m^2\,d^{-1}$	effective thermal diffusivity
v	$m\,d^{-1}$	thermal front velocity
q	$m\,d^{-1}$	Darcy velocity
ρ_w	$kg\,m^{-3}$	density of the fluid
c_w	$J\,kg^{-1}\,°C^{-1}$	heat capacity of the fluid
ρ	$kg\,m^{-3}$	bulk density of the matrix
c	$J\,kg^{-1}\,°C^{-1}$	bulk heat capacity of the matrix
n	-	porosity
ρ_s	$kg\,m^{-3}$	density of the solid
c_s	$J\,kg^{-1}\,°C^{-1}$	heat capacity of the solid
v_{pw}	$m^{-1}\,d^{-1}$	porewater velocity
κ	$J\,s^{-1}\,m^{-1}\,°C^{-1}$	bulk thermal conductivity
β	m	thermal dispersion coefficient
γ	-	power law coefficient
κ_w	$J\,s^{-1}\,m^{-1}\,°C^{-1}$	thermal conductivity of the water
κ_s	$J\,s^{-1}\,m^{-1}\,°C^{-1}$	thermal conductivity of the solid
D_h	$m^2\,d^{-1}$	effective thermal diffusivity
D_s	$m^2\,d^{-1}$	effective solute diffusivity
D_{href}	$m^2\,d^{-1}$	bulk sediment conductivity
D_{sref}	$m^2\,d^{-1}$	bulk sediment solute diffusivity
α	-	solute/thermal dispersion coefficient
Pe_h	-	thermal Péclet number
Pe_s	-	solute Péclet number
L	m	characteristic length
i	-	hour number is time record
j	-	thermistor number
$\bar{T}$	°C	weighted depth-averaged T
CI	-	confidence intervals
R^2	-	coefficient of determination
RMSE	-	root mean square error
r^2	-	correlation coefficient

Table 3.2: Table of model skill metrics: the squared correlation (R^2), the p-value, the root mean square error (RMSE), and the bias between observed and modeled dT/dt for freshwater and marine datasets.

Site	Array	R^2	p-value	RMSE	Bias
Boyer	TP01	0.946	3.22E-47	1.61	0.26
	TP02	0.993	5.81E-78	0.528	-0.025
	TP03	0.986	5.41E-67	0.938	-0.17
	TP04	0.993	5.69E-78	0.623	0.068
	TP05	0.988	7.70E-70	0.764	0.0094
	TP06	0.995	1.35E-78	0.547	0.85
	TP07	0.971	4.36E-54	1.05	-0.37
	TP08	0.905	1.22E-36	2.34	0.50
	TP09	0.967	2.50E-50	1.39	-0.036
	TP10	0.468	8.37E-11	8.98	-13.7
	TP11	0.744	9.15E-24	4.69	5.4
	TP12	0.924	4.70E-39	2.42	8.9
	TP13	0.979	4.01E-62	1.07	0.50
Nine Mile 2009	TP04	0.981	5.31E-117	0.44	-0.052
	TP05	0.305	1.29E-12	7.4	-0.45
	TP08	0.991	5.42E-144	0.28	-0.0032
	TP09	0.988	1.63E-135	0.43	0.013
	TP10	0.992	3.47E-142	0.26	0.014
Nine Mile 2010	TP01	0.984	1.45E-74	0.539	0.19
	TP02	0.984	6.58E-78	0.532	0.24
	TP03	0.992	5.24E-88	0.306	0.023
	TP04	0.984	6.61E-75	0.722	0.13
	TP05	0.992	2.24E-87	0.367	0.070
	TP06	0.284	3.29E-07	10.1	-2.7
	TP07	0.972	7.26E-64	1.17	0.56
	TP08	0.982	4.48E-73	0.431	0.18
	TP09	0.987	3.94E-80	0.434	0.11
	TP10	0.991	4.53E-87	0.373	0.037
	TP11	0.989	3.01E-82	0.377	0.14
	TP12	0.983	3.32E-73	0.553	0.29
Kilo Nalu	Main	0.809	4.00E-250	0.1483	0.0055
	Side	0.5401	4.66E-110	0.2876	0.0281
	Deep	0.882	4.73E-296	0.0325	-0.0036
	Main[*]	0.893	1.56E-239	0.0942	0.0077
	Side[*]	0.912	1.45E-272	0.0759	0.0311
	Deep[*]	0.896	1.39E-283	0.0306	-0.0011

[*] Model skill metrics after removal of theoretically impossible values (see text).

Table 3.3: Statistical and analytical estimates of v and D for freshwater temperature profiles are compared using the correlation squared (r^2), p-values, root mean square error (RMSE) and bias. Bias values are reported with reference to the VFLUX2 outputs.

Site	Array	v				D			
		r^2	p-value	RMSE	bias	r^2	p-value	RMSE	bias
Boyer	TP01	0.057	0.34	0.453	4.96	0.590	2.80E-06	0.0264	0.127
	TP02	0.654	2.36E-07	0.039	-0.204	0.627	8.23E-07	0.00250	0.0201
	TP03	0.724	5.66E-09	0.078	0.266	0.021	0.18	0.0176	0.0789
	TP04	0.232	0.0044	0.065	-0.106	0.174	0.024	0.0207	-0.0545
	TP05	0.298	0.0032	0.049	-0.0448	0.001	0.49	0.0118	0.116
	TP06	0.009	0.90	0.361	-0.537	0.196	0.058	0.0470	-0.108
	TP07	0.127	0.069	0.301	0.671	0.568	2.24E-05	0.0208	0.0613
	TP08	0.464	2.41E-04	4.13	11.9	0.906	4.39E-13	0.0707	-0.0649
	TP09	0.002	0.97	0.329	1.74	0.015	0.537	0.0915	-0.0027
	TP12	0.761	1.47E-10	1.11	4.62	0.629	1.45E-07	0.188	0.188
	TP13	0.148	0.026	0.142	0.484	0.095	0.041	0.0331	0.0773
Nine Mile 2010	TP01	0.003	0.964	0.022	-0.0552	0.306	0.0010	0.0038	0.0136
	TP02	0.220	0.013	0.038	-0.156	0.457	3.01E-05	0.0056	0.0194
	TP03	0.031	0.63	0.019	-0.0218	0.609	1.33E-07	0.0026	0.0112
	TP04	0.319	0.0014	0.053	0.111	0.313	4.70E-05	0.0140	0.0345
	TP05	0.164	0.012	0.034	-0.131	0.654	1.19E-07	0.0038	0.0196
	TP07	0.829	8.38E-12	0.248	1.48	0.782	2.53E-11	0.0157	0.164
	TP08	0.123	0.032	0.038	0.0369	0.394	2.03E-04	0.0034	0.0015
	TP09	0.017	0.76	0.036	-0.167	0.187	0.0099	0.0034	0.0190
	TP10	0.001	0.65	0.020	-0.0983	4.00E-05	0.97	0.0034	0.0146
	TP11	0.049	0.13	0.021	-0.190	0.454	1.97E-05	0.0031	0.0218
	TP12	0.395	1.65E-04	0.038	-0.136	0.717	1.56E-09	0.0033	0.0182

Table 3.4: Evaluation of relationships between statistical outputs of *v* and *D* for both the freshwater and marine environments using the dispersivity-velocity power law relationship in Equation (3.6), or the normalized dispersivity-Péclet number relationship in Equation (3.8).

		Freshwater				Kilo Nalu			
		Boyer	Nine Mile 2009	Nine Mile 2010	All	Main	Side	Deep	All
Eq. (6)	γ	0.79	1.17	1.26	0.98	3.3	1.97	1.55	2.04
	β	0.127	0.200	0.165	0.069	0.427	0.106	0.068	0.084
	$\kappa/\rho c$	0.0096	0.1200	0.1100	0.12	0.0251	0.0234	0.0210	0.0239
	R^2	0.973	0.771	0.911	0.917	0.182	0.283	0.863	0.490
Eq. (8)	α	0.12	0.28	0.32	0.11	0.20	0.30	0.39	0.23
	R^2	0.967	0.768	0.901	0.917	0.11	0.27	0.83	0.34
	n	560	685	860	2105	541	565	567	1673
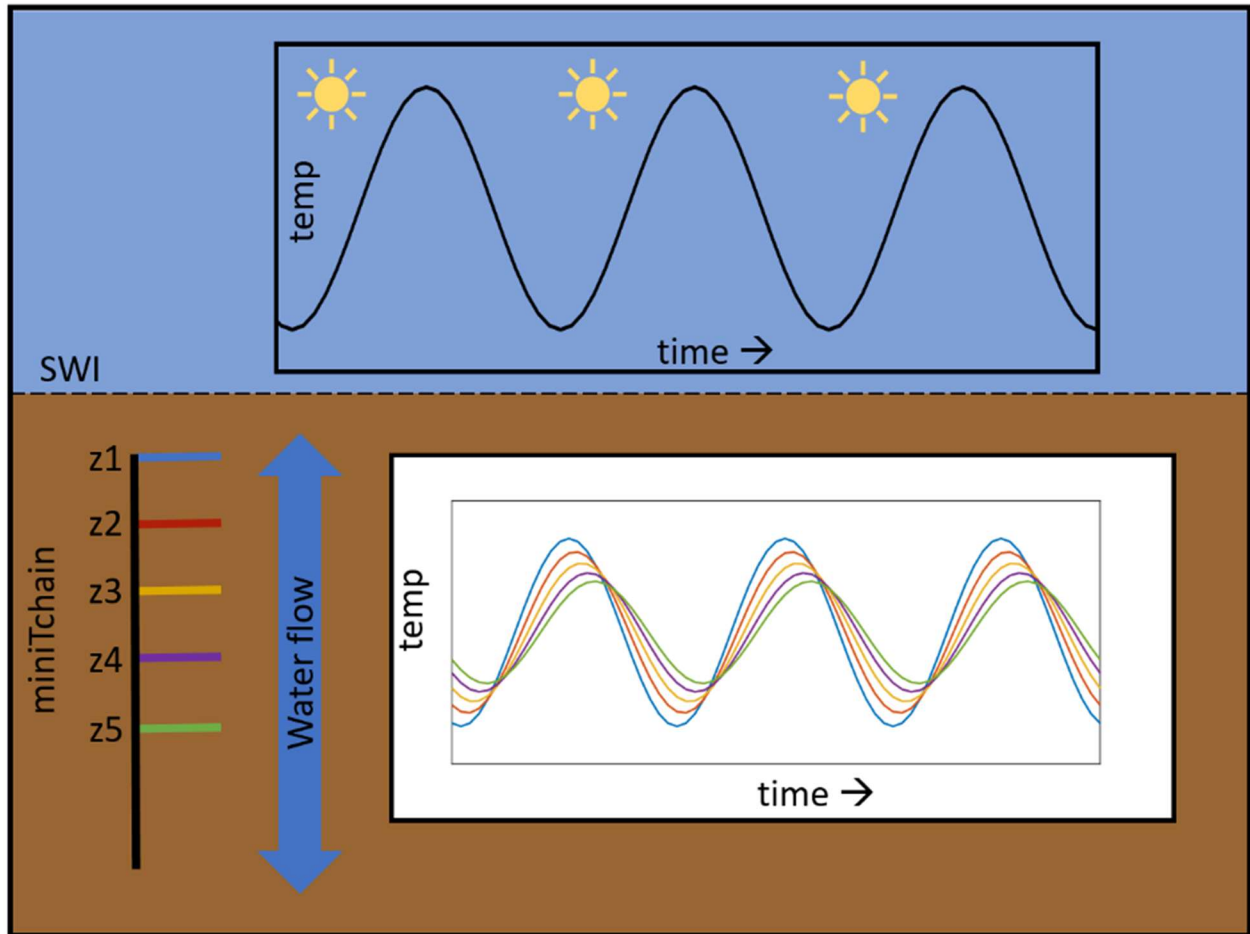
Figure 3.1: An idealized schematic of daily temperature changes penetrating into a sediment. As heat penetrates into the sediment, through conduction and convection, the temperature signal is recorded by thermistors. The color of the thermistor corresponds with the color of the recorded tempeature signal in the sediment. The recorded sediment tempearture signal is lagged and attenuated with depth.
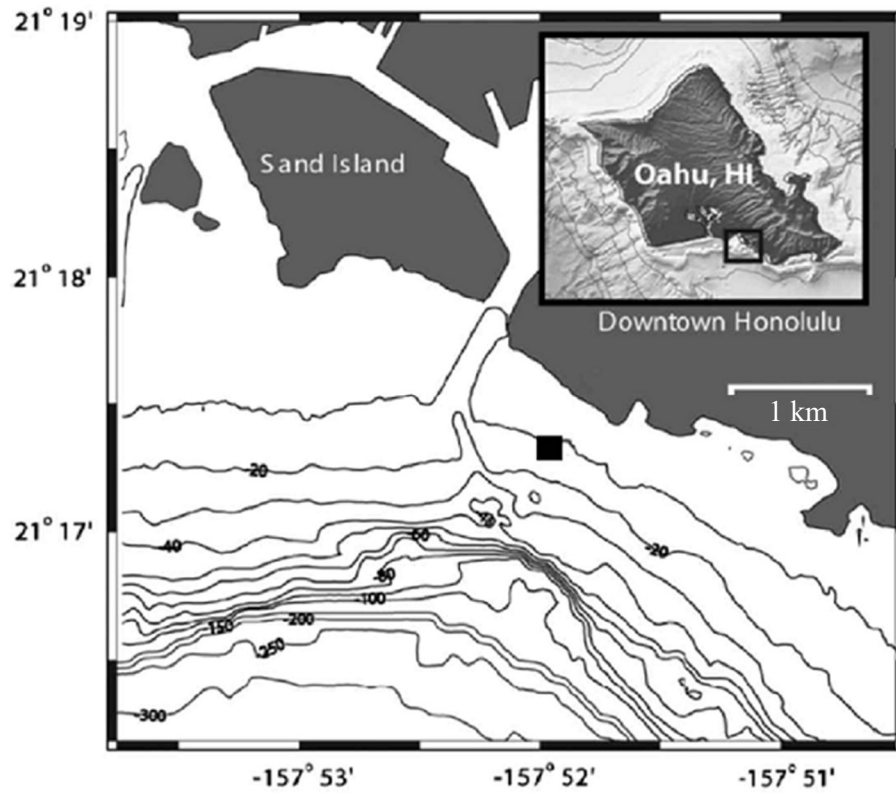
Figure 3.2: Location of the field site, Kilo Nalu, on the south shore of Oahu, Hawaii. The black square indicates the sand patch where experiments were conducted at 12-m depth. Depth contours are in meters (From Fram et al. 2014).
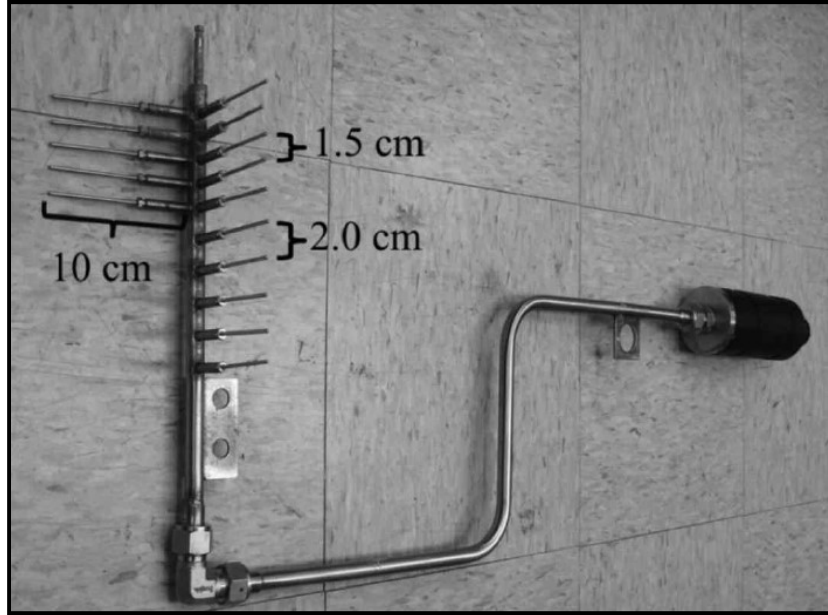
Figure 3.3: Photograph of the miniTchain. The electronics module is located in the black cylinder to the right. Background tiles are 30 x 30 cm. The left 5 thermistors are referred to as the Side Array, while the top 5 thermistors and bottom 5 thermistors on the right make up the Main and Deep Arrays, respectively (from Fram et al. 2014).
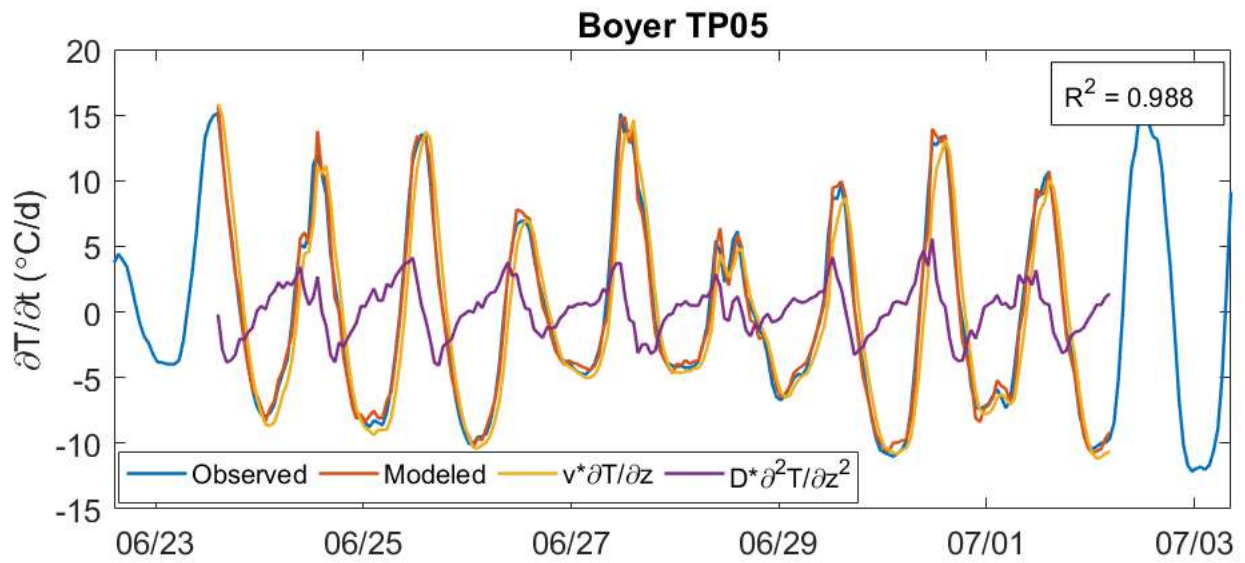
Figure 3.4: Time series of observed and modeled dT/dt for a high skill example of model results for the freshwater datasets. Contributions to the modeled dT/dt from the *D* and *v* terms are shown.
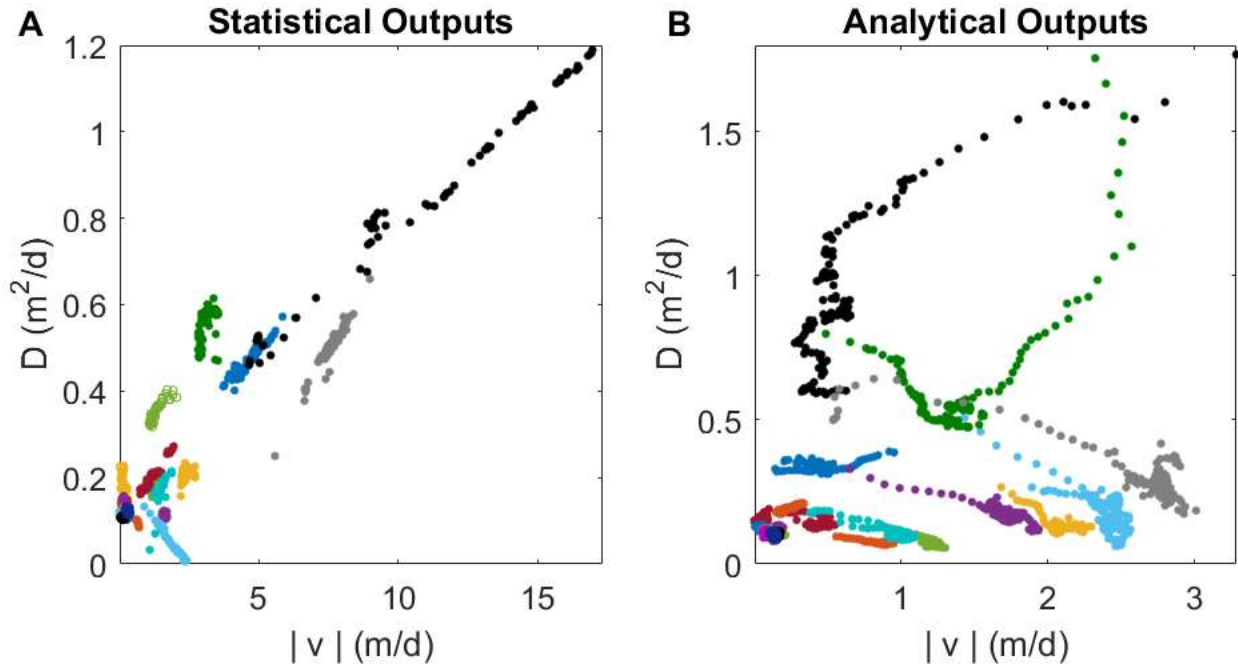
Figure 3.5: Plots of effective thermal diffusivity (*D*) as a function of the magnitude of the thermal front velocity (*v*) from (A) the statistical solution, and from (B) the analytical solution for freshwater temperature profiles that passed the statistical assessment ($R^2 > 0.90$). Outputs are color coded for each temperature profile examined, and are consistent for both panels.
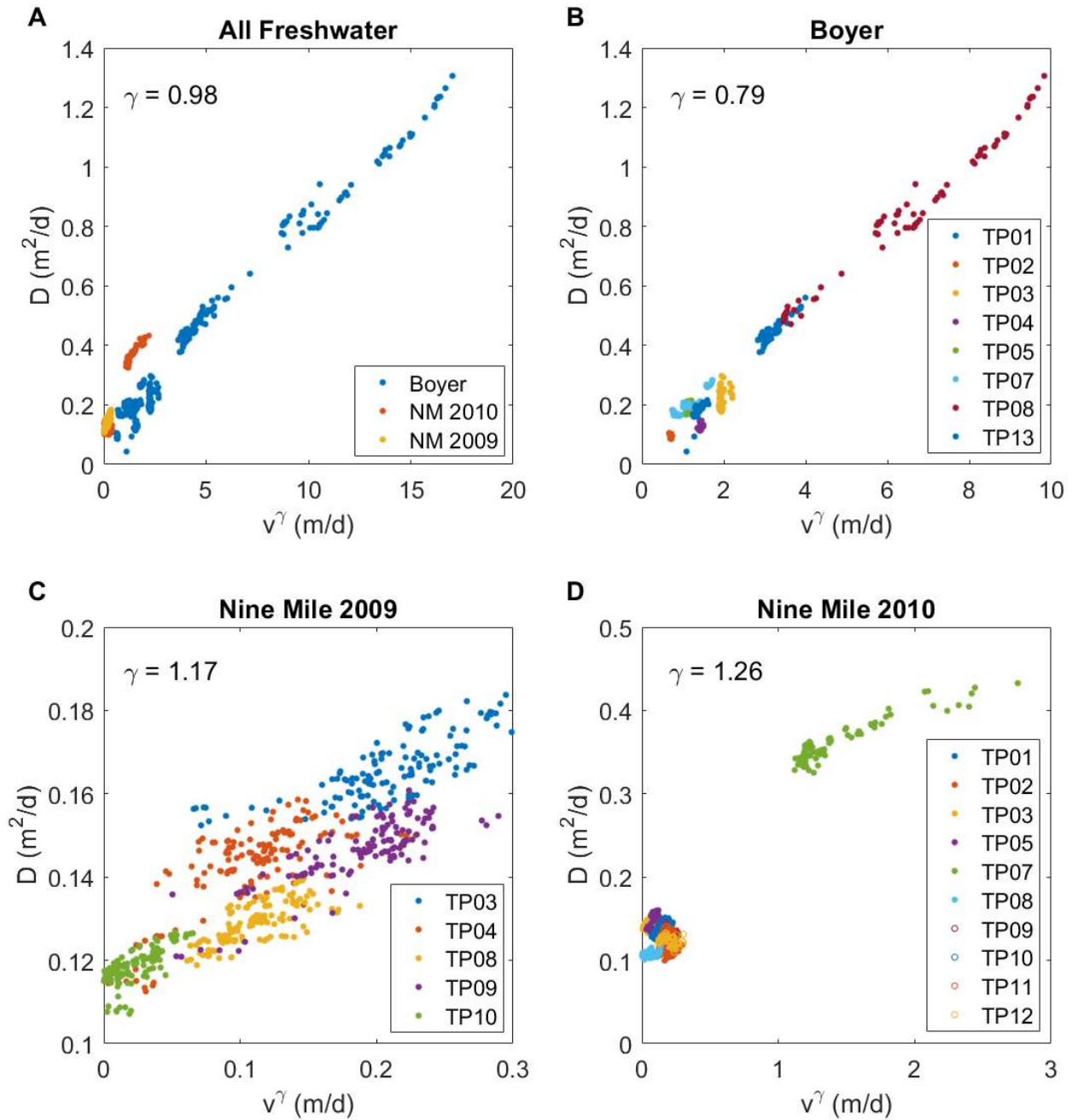
Figure 3.6: Optimized thermal dispersivity-velocity relationship from statistical model outputs for freshwater temperature profiles (TPs) that passed the statistical and theoretical assessments for (A) all sites, (B) Boyer Creek , (C) Nine Mile Creek in 2009, and (D) Nine Mile Creek in 2010. The variable γ, calculated for each creek, is the exponent used to optimize the dispersivity-velocity power law relationship in Equation (3.6).
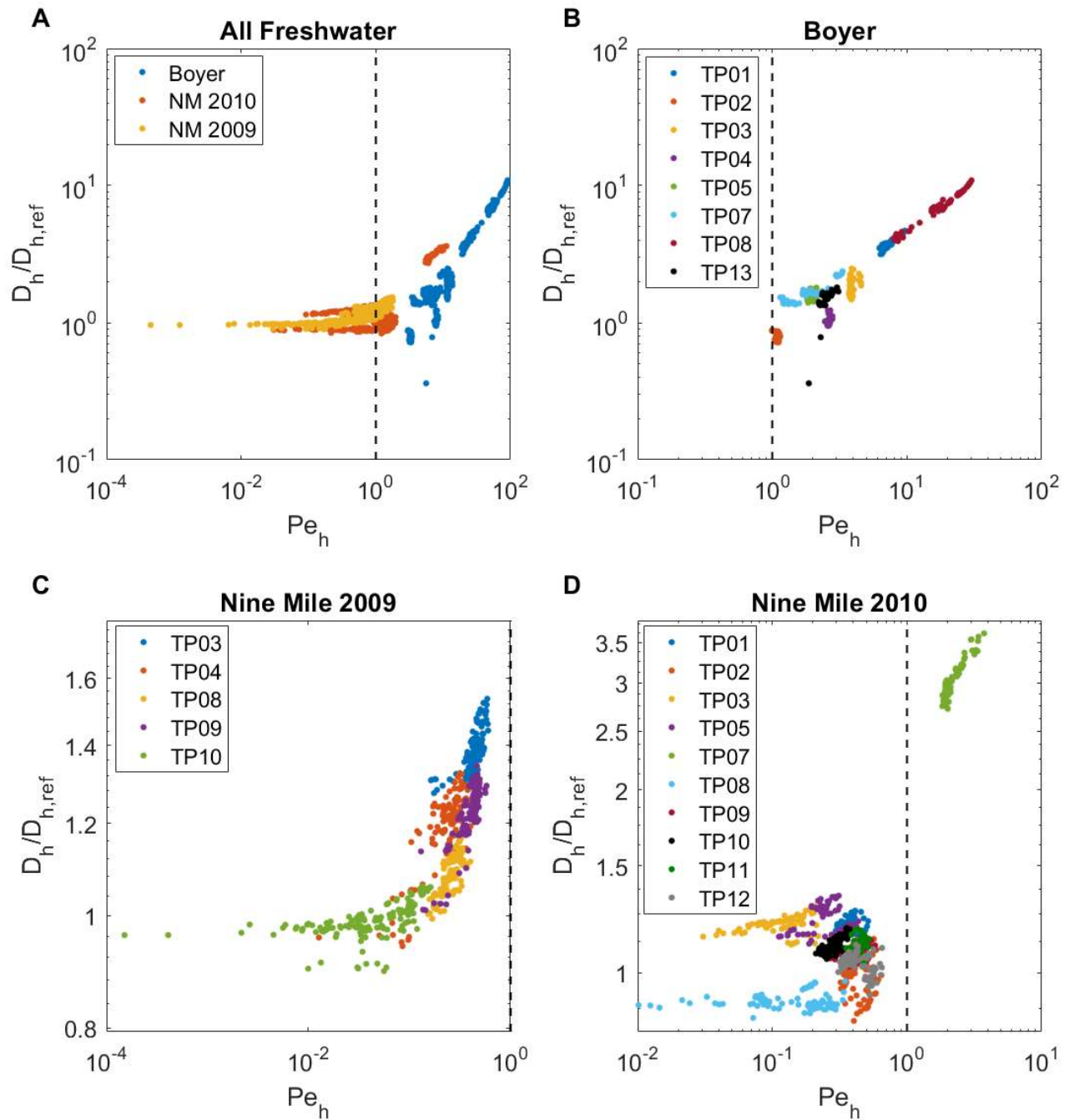
Figure 3.7: Normalized thermal dispersivity-Péclet number relationships (Equation 3.8) from statistical model outputs for freshwater temperature profiles (TPs) that passed the statistical and theoretical assessments for (A) all sites, (B) Boyer Creek, (C) Nine Mile Creek in 2009, and (D) Nine Mile Creek in 2010. Vertical dashed lines indicate a thermal Péclet number of 1. Note the differences in scales.
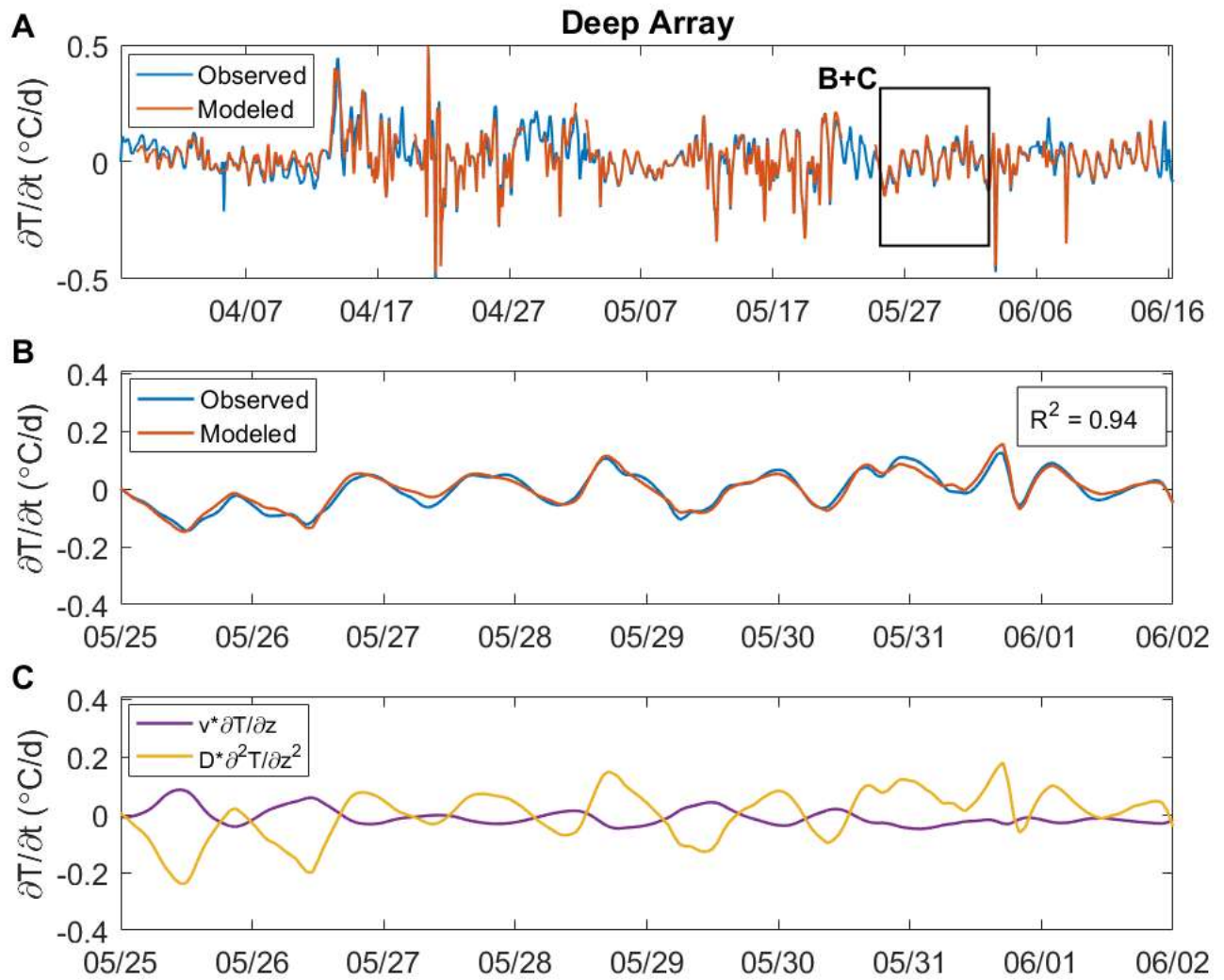
Figure 3.8: (A) Time series of observed and modeled dT/dt for the Deep Array at Kilo Nalu for the whole deployment. Time series of modeled dT/dt excludes theoretically-impossible results (see text). (B) Time series of observed and modeled dT/dt, and (C) contributions to the modeled dT/dt from the *D* and *v* terms for a week-long subperiod of high model skill.
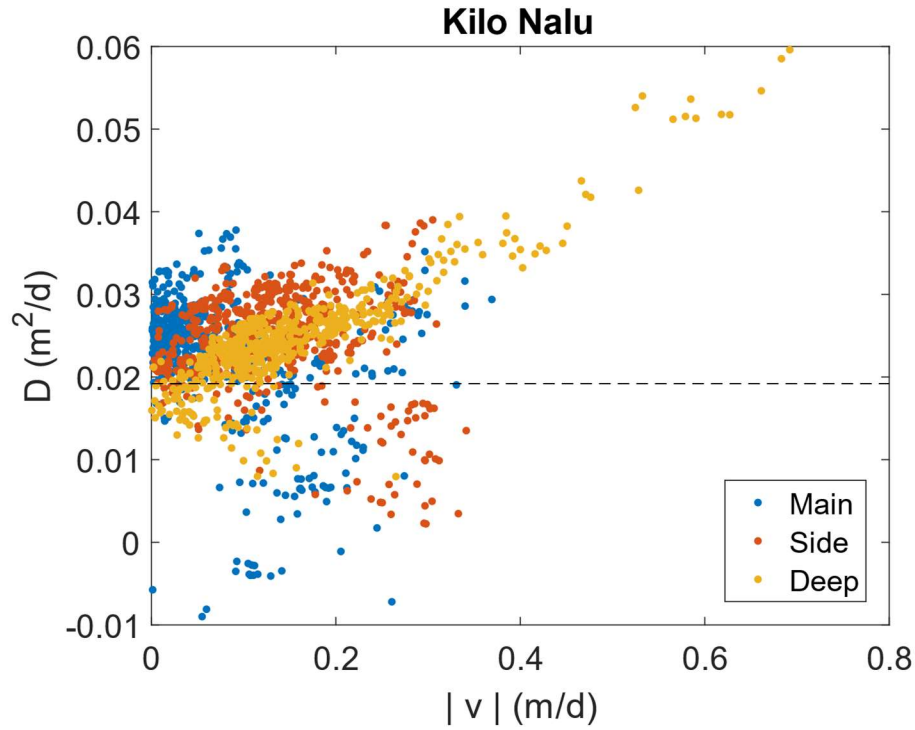
Figure 3.9: Output for effective thermal diffusivity (*D*) as a function of magnitude of the thermal front velocity (*v*) for the Main, Side and Deep Arrays for the entire 80-day deployment at Kilo Nalu. The dashed line represents the estimated thermal diffusivity for the sediments (0.018 m^2d^{-1}, see text). Values below the estimated thermal diffusivity of the sediments were considered invalid and removed from further analysis.
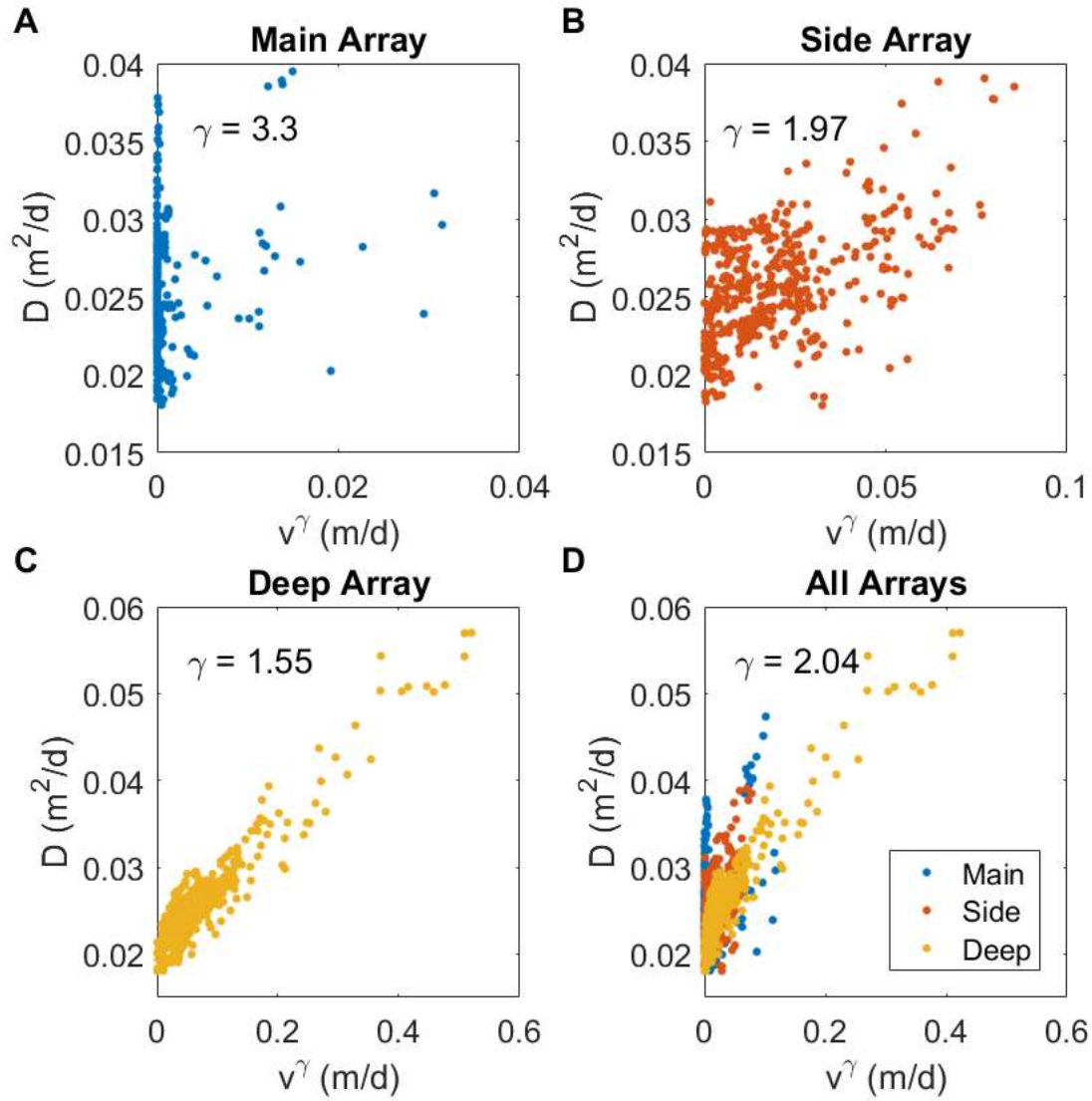
Figure 3.10: Optimized dispersivity-velocity power-law relationships for model-generated results for the (A) Main Array, (B) Side Array, (C) Deep Array, and (D) all Arrays at Kilo Nalu using theoretically assessed outputs of D and v. The γ exponent is used to optimize the dispersivity-velocity power-law relationship in Equation (3.6).
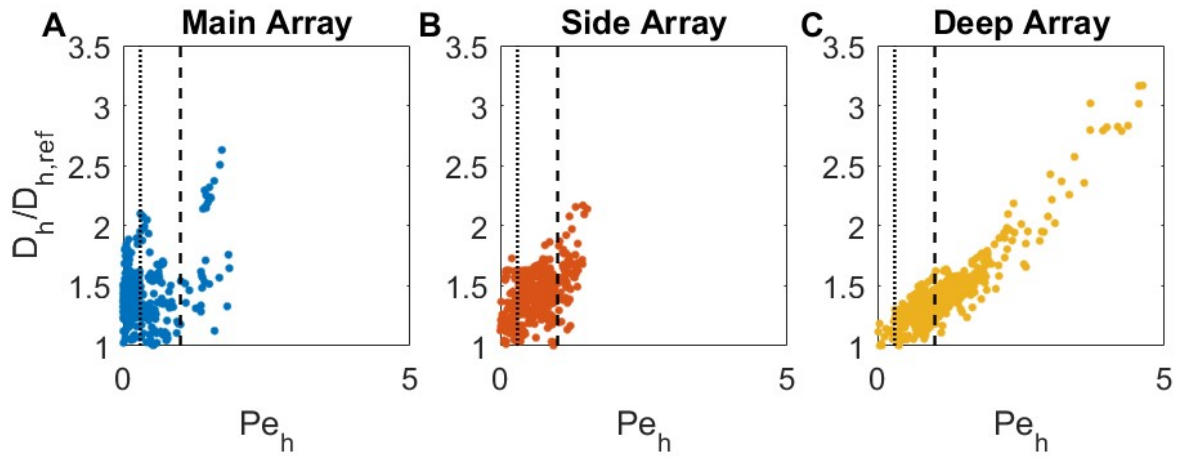
Figure 3.11: Normalized thermal dispersivity-Péclet number relationships (Equation 3.8) for statistical model ouput from the (A) Main Array, (B) Side Array, and (C) Deep Array at Kilo Nalu that passed the theoretical assessment (see text). Vertical dotted lines indicate a Péclet number of 0.3, and vertical dashed lines indicate a Péclet number of 1.
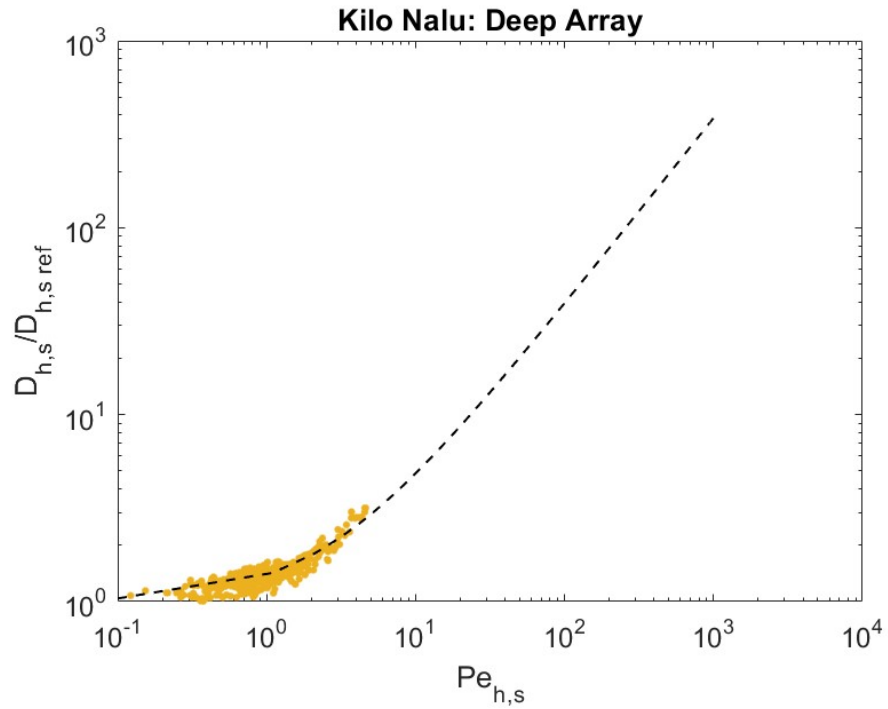
Figure 3.12: The normalized dispersivity-Péclet number relationship for statistical model output of D and v using a unified dispersivity coefficient of $\alpha = 0.385$ in Equation (3.8). The dashed line indicates the projected normalized dispersivity over a larger range of heat (h) or solute (s) Péclet numbers using the dispersivity coefficient of $\alpha = 0.385$ (see text).
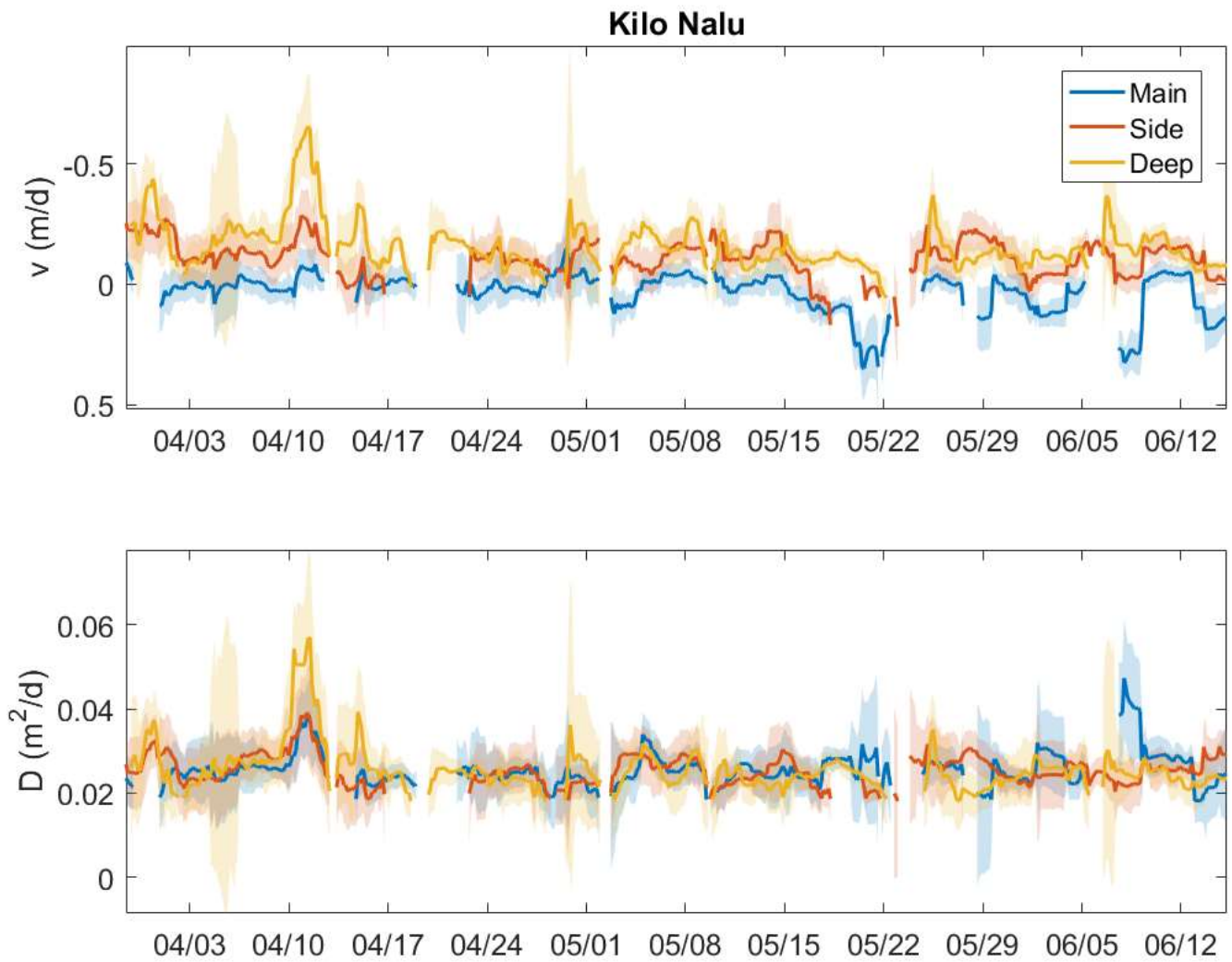
Figure 3.13: Vertical values of *v* (top panel) and *D* (bottom panel) for the Main, Side and Deep Arrays at Kilo Nalu in 2011 for model output that passed the theoretical assessment (see text). Error bars indicate 95% confidence intervals.
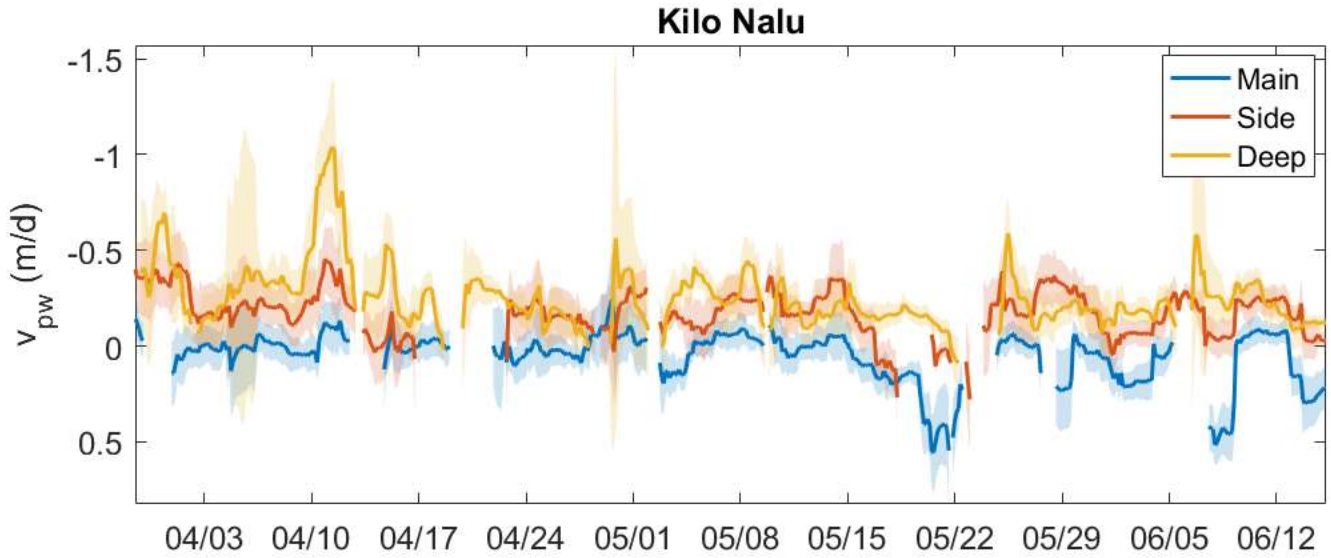
Figure 3.14: Vertical porewater velocities (v_{pw}) at Kilo Nalu in 2011. Negative velocities indicate motion towards the water column and positive velocities indicate motion into the bed. The average center depth of the miniTchain arrays over the 80-day deployment was 10 cm below the SWI for the Main and Side Arrays, and 19 cm below the SWI for the Deep Array. Error bars indicate 95% confidence intervals.

Chapter 4: Nutrient and carbon fluxes and depth-dependent remineralization rates in permeable sediments estimated using 1-D diagenetic models

4.1 Abstract

While the importance of enhanced exchange between the sediment and water column to permeable sediment biogeochemistry has now been recognized, the quantification of fluxes and remineralization rates in these environments remains challenging. The goal of this study was to apply field-measured porewater transport rates to diagenetic models to estimate depth-dependent solute fluxes and remineralization rates in permeable sediments. Porewater transport rates were constrained using the rate of change in the vertical temperature structure of the porewater-sediment matrix, and modeled to decay exponentially below the sediment water interface (SWI). Porewater profiles and field-constrained transport rates were used in 1-D steady-state diagenetic models to calculate depth-dependent vertical fluxes of dissolved nutrients and carbon at two nearshore sites dominated by permeable carbonate sediments. Profiles of the depth-dependent solute production and consumption processes were then inversely calculated as the divergence or convergence of the solute fluxes. Resultant solute fluxes at the SWI are consistent with other field-based permeable sediment flux measurements. However, additional measurements are needed to quantify the processes (e.g., benthic primary production, denitrification, larger-scale circulation) driving carbon and nutrient dynamics and resultant fluxes in these environments.

4.2 Introduction

Although sandy, permeable sediments (permeability $> 10^{-12}$ m^2) cover nearly half of continental shelves worldwide (Riedl et al. 1972; Hall 2002), their role in nearshore and global biogeochemical budgets is not well constrained. Historically, the study of permeable sediment environments has been neglected, in part because they were typically observed to have lower

107

organic matter content than fine-grained sediments (Meyer-Reil 1986; Boudreau et al. 2001), resulting in the perception that they are 'biogeochemical deserts' (Boudreau et al. 2001; Rocha 2008). However, high oxygen consumption rates measured in permeable sediments (Reimers et al. 2004; Rusch et al. 2006), coupled with their low organic matter content, indicate that these sediments may in fact be sites of high biogeochemical activity and efficient organic matter remineralization (Webb and Theodor 1968; Huettel et al. 1998a; Rocha 2008), even matching metabolic rates found in organic-rich, fine-grained sediments (Jahnke et al. 2000, 2005b).

Permeable sediments are able to support high remineralization rates through enhanced fluid and particle transport between the water column and porewater (Santos et al. 2012b; Huettel et al. 2014). This enhanced exchange of solutes and particles promotes a biogeochemically active system by delivering oxygenated water (Ziebis et al. 1996; Fogaren et al. 2013) and labile organic matter (Huettel et al. 1996; Huettel and Rusch 2000b) to the sediments, while flushing remineralization end-products to the overlying water column (Grigg 1995; Huettel et al. 1998b).

Because permeable sediments are subject to advective flows, conventional methods used to calculate porewater fluxes in fine-grained, diffusively dominated sediments (e.g., coring, porewater extraction, benthic chambers) are often unsuitable, as they either disrupt the structure of sandy sediments or interfere with the hydrodynamics that make permeable sediments so biogeochemically reactive (Boudreau et al. 2001). As a result, eddy-covariance methods (Berg et al. 2003), stirred benthic chambers (Janssen et al. 2005), dye-based tracer studies (Webb and Theodor 1968; Precht and Huettel 2004b; Hebert et al. 2007), and sedimentary temperature-depth measurements (Fram et al. 2014; Wilson et al. 2016; Chapter 3) have been developed as less invasive techniques to measure fluxes in nearshore permeable sediments.

While the importance of enhanced exchange between the sediment and the overlying water column in permeable sediment biogeochemistry has now been recognized, the quantification of fluxes and sedimentary remineralization rates in these environments remains challenging. The goal of this study was to apply field-measured porewater transport rates to 1-D diagenetic models to estimate depth-dependent solute fluxes and remineralization rates in permeable sediments.

4.3   Methods

4.3.1   Site Descriptions

Nearshore field experiments were conducted at two sites off Oahu, Hawaii dominated by permeable carbonate sediments. The two study sites, the Medium Sand Site (Medium Site, Figure 4.1), located at the Kilo Nalu Nearshore Reef Observatory (Kilo Nalu, KN), and the Fine Sand Site (Fine Site, Figure 4.2), located at Makai Research Pier (Makai Pier, MRP), were selected because of their different sediment characteristics (Table 4.1) and their relative ease for deploying instruments.

The Medium Site is 12-m deep, located ~385 m offshore in Mamala Bay on the south shore of Oahu, Hawaii. The study site is located within a large sand patch that is part of a larger, carbonate reef framework (Figure 4.1). The upper sediment (defined here to be the uppermost ~10 cm) at the Medium Site was previously determined to be >99 % sand, with a phi value of 2.27 and phi standard deviation of 0.46 (Fogaren et al. 2013), indicating a well-sorted sediment (Folk and Ward 1957). In contrast, the deeper sediment had greater heterogeneity, with large coral debris found at sediment depths of 15 cm and deeper. The sediment permeability and the sediment porosity at the Medium Site were previously determined to be ~3.9×10^{-11} m^2 and 0.49, respectively (Hebert et al., 2007).

The existing infrastructure at Kilo Nalu allowed for long-term continuous instrument deployment and for the collected hydrodynamic data to be accessed in near real-time (Sansone et al. 2008; Pawlak et al. 2009). Surface-gravity waves and water-column currents were measured using a bottom-mounted, upward-facing 1200-kHz acoustic Doppler current profiler (ADCP; RDI-Teledyne, Poway, CA, USA). The vertical temperature structure of the porewater-sediment matrix was measured using a miniature thermistor chain (miniTchain; custom built by Precision Measurement Engineering, Inc., Vista, California, USA). See Chapter 3 for a full description of the miniTchain.

The Fine Site is 3-m deep, located ~115 m from shore in a back-reef lagoon northwest of Makapu'u Point on the easternmost extremity of Oahu, Hawaii (Figure 4.2). Because no ocean-observing infrastructure existed at Makai Pier, instruments were deployed as needed using the Permeable Sediment Observatory (PSO). The PSO is a mobile, bottom-mounted platform equipped with a suite of oceanographic instruments. The platform can either be powered from shore or by batteries. For the Makai Pier deployment, the PSO was powered by two 24-V deep-cycle marine batteries and was outfitted with the above-mentioned 1200-kHz ADCP and the miniTchain. The data logger on the PSO was designed to record measurements from multiple instruments with a unified time stamp, and was connected to a shore-based computer for on-demand data access.

4.3.2   *Water-column hydrodynamics*

Surface-gravity waves and bottom currents are important drivers of enhanced fluid and particle transport in permeable sediments in nearshore wave-impacted environments (e.g., Santos et al. 2012b; Fogaren et al. 2013; Huettel et al. 2014). There are two distinct types of ocean swells of interest at our study sites. The trade wind swell is the dominant type of swell at the Fine

Site. The trade wind swell is also common at the Medium Site, as the swell can wrap around the southern flank of Diamond Head and impact the south shore of Oahu. These swells are persistent most of the year, with typical wave heights of 0.3-1.3 m and periods of 5-8 s (Fletcher et al. 2002). The Medium Site is also impacted by southern swells that are generated in the southern hemisphere by austral winter storms (Fletcher et al. 2002; Fogaren et al. 2013). The southern swell typically occurs from April to October, and results in waves of 0.3-1.2 m in height with 14- to 22-s periods (Moberly and Chamberlain 1964; Fletcher et al. 2002).

The ADCP measured near-bed current velocity, surface-wave characteristics, and tide levels. At the Medium Site, the bottom-mounted, upward-looking ADCP was deployed continuously and was configured to collect high-resolution ensemble pressure and velocity data at 1 Hz. Velocity readings were collected starting at 0.56 m above the sediment water interface (SWI), continuing upward through the water column at a vertical resolution of 25 cm. Wave data presented in this study were calculated over 20-min periods, the shortest period over which wave statistics could be reasonably calculated. Values of significant wave height (H_{sig}) were determined using a spectral method (Emery and Thomson 2004) in which H_{sig} is equal to four times the integral of the power spectrum (wave energy as a function of frequency); this is equivalent to the mean height of the one-third largest waves. Values for H_{sig} were averaged in three-hour intervals to correspond with porewater velocity measurements (see Section 4.3.5.1).

At the Fine Site, a bottom-mounted, upward-facing ADCP was deployed during porewater experiments and was configured to collect pressure and velocity data. Burst velocity measurements were collected at 5-min intervals starting at 0.81 m above the SWI, continuing upward through the water column with a vertical resolution of 50 cm. Velocity measurements are

reported as the center of the 50-cm depth bins, with the first bin depth-centered at 1.06 m above

the SWI. Wave characteristics are not available for the Makai Pier deployment.

At both sites, near-bed velocities, V_{bed}, were used as an indication of hydrodynamic

conditions close to the SWI. Values of V_{bed} were calculated from significant velocities, V_{sig},

which are equivalent to the mean of the highest one-third of the current speeds measured

vertically throughout the water column. To compare the water-column velocities measured at

different heights above the SWI at the two sites, velocities at both sites were normalized to the

same depth by modeling the flow velocity as decreasing logarithmically towards the SWI. To

estimate the logarithmic decay of the flow velocities at the two sites, the mean shear velocity, u_*,

was calculated for each site using significant velocities from the two bins closest to the SWI

(Wright et al. 1999):

$$u_* = \frac{1}{5.75} \cdot \frac{d\bar{u}}{d\,log\,z} \,, \tag{4.1}$$

where $\bar{u}$ is the mean of the significant velocity measurements (m s^{-1}), and z is the depth of the

velocity measurements (m), reported as the center of the ADCP depth bin.

At the Fine Site, the mean of the significant velocities from 1.06 and 1.56 m above the

SWI were used to calculate u_*. At the Medium Site, a representative u_* value was estimated

from significant velocity measurements from 0.81 and 1.06 m above the SWI using ten

randomly-chosen 3-hour velocity profiles from the 80-day deployment (Figure 4.3). With a mean

u_* calculated for each site, the logarithmic decay of the current velocity from its measurement

height above the SWI to 0.3 m above the SWI was estimated by rearranging Equation 4.1 (Figure

4.4). Values for H_{sig} and V_{bed} were averaged in three-hour intervals to correspond with time intervals of estimated porewater velocities.

4.3.3 Sampling and analysis of sediment

Sediment porosity, permeability, and grain-size distribution were previously measured at the Medium Site (Hebert et al. 2007; Hannides 2008; Fogaren et al. 2013). At the Fine Site, bulk-sample sediment grabs from the uppermost sediment (<10 cm) were collected by divers for measurement of solid-phase characteristics. Grain-size distributions were determined by wet sieving, and the results were used to calculate mean grain size and sorting characteristics according to McManus (1988). Sediment porosities ($\pm$ 0.01) were measured gravimetrically (Breitzke 2000), and sediment permeabilities were obtained by the constant-head method (Klute and Dirksen 1986). The mean standard deviation of duplicate permeability measurements was 0.35×10^{-12} m^2.

At both sites, total weight percent carbon (TC; $\pm$ 0.12 %) was determined from ground sediment using an elemental analyzer (Exeter Analytical Elemental Analyzer, model CE-440; Gordon, 1969). Coulometery (UIC, model CM5230) was used to determine total weight-percent inorganic carbon (TIC; $\pm$ 0.17 %; Dickson and Goyet, 1994), and the sediment organic matter content was determined by difference (TC – TIC; $\pm$ 0.21 %).

4.3.4 Porewater sampling and analysis

4.3.4.1 Porewater sampling

Divers manually collected porewater samples for analysis of dissolved constituents. At the Fine Site, porewater was collected by inserting stainless-steel sampling needles to the desired sediment depth, similar to the method described by Berg and McGlathery (2001). The porewater sampling needles were connected to 12-mL plastic syringes (Becton, Dickinson, and Co.) via

three-way stopcocks (Tomopal, Inc.). Custom-built needles (Hamilton Co.) with conical tips and two opposing side-sampling ports were used in this study to avoid clogging. The needles were thin (1.6 mm i.d.) to ensure that minimal internal dead space needed to be cleared before collection of the intended porewater.

At the Fine Site, porewater samples for vertical profiles were collected from 3, 5, 7, 9 and 11 cm below the SWI on 29 November 2013, 2 December 2013, and 13 December 2013. Assuming spherical volumes for the regions of the porewater sampled, sediment sampling volumes were calculated using porewater sample volumes and a measured sediment porosity of 0.59. The sediment sampling volume for 5-mL porewater samples was ~8.5 cm^3, which corresponded to a vertical porewater sample depth resolution of ca. ±1.3 cm.

At the Medium Site, porewater was manually collected by divers from porewater sampling wells (Falter and Sansone 2000c; Fogaren et al. 2013) using 140-mL Monoject plastic syringes (Medtronic) connected to Tygon tubing via three-way stopcocks. Porewater samples were collected from 5, 12.5, 17, 27, 37, and 47 cm below the SWI after the dead volume in each well was discarded. Samples were collected on 28 March 2011, 6 April 2011, and 15 April 2011. Again, assuming a spherical sampling shape, and accounting for sample volume and a sediment porosity of 0.49 (Hebert et al. 2007), a 140-mL porewater sample was extracted from a sediment volume of ~286 cm^3, and had a vertical depth resolution of about ca. ±4 cm. Bottom-water nutrient samples were also collected with 140-mL plastic syringes at each site from ~5 cm above the SWI.

Once collected, porewater and bottom-water samples were taken to shore and filtered. Porewater samples were filtered through polyethersulfone syringe filters (25-mm diameter, nominal poresize of 0.2 μm) at the Fine Site and precombusted Whatman GF/F filters (25-mm

114

diameter, nominal poresize of 0.7 µm) held in plastic Whatman Swin-Loc filter holders (GE

Healthecare, UK) at the Medium Site. Water samples for nutrient analysis were stored cold

(~1.5°C) in the dark until analysis. Water samples for dissolved inorganic carbon (DIC) analysis

were preserved in 20-mL glass serum bottles using 50 µL of saturated mercuric chloride solution

as a preservative (Dickson et al. 2007)

4.3.4.2   *Porewater analysis*

Porewater samples were analyzed for soluble reactive phosphate (SRP; ± 0.6 µM),

silicate (Si; ± 0.3 µM), total nitrate + nitrite (NO$_x$; ± 0.3 µM) and ammonium (NH$_4^+$; ± 0.8 µM)

using miniaturized colorimetric and fluorometric methods (Grasshoff et al. 1983; Kérouel and

Aminot 1997; Campbell et al. 2006; Ringuet et al. 2011). Samples were reacted in 96-well

optical-bottom plates with a 1-cm pathlength (Nalge Nunc International) and measured on a

BioTek Synergy HT Multi-Mode Microplate Reader (BioTek). Samples at the Fine Site were

analyzed in duplicate for SRP and Si, while larger sample volumes at the Medium Site allowed

for analytical triplicate measurements of SRP, Si, NO$_x$ and NH$_4^+$. The mean detection limits for

SRP, Si, NO$_x$ and NH$_4^+$ were 0.6 µM, 0.6 µM, 1.1 µM and 1.0 µM, respectively.

The larger porewater volumes collected at the Medium Site allowed for additional

measurements of total dissolved nitrogen (TDN; $\pm 4.63\%$) and dissolved organic carbon

(DOC; $\pm 0.46\%$) using a TOC-L Combustion Analyzer (Shimadzu, model TOC-V; Gordon

1969). Dissolved inorganic carbon (DIC; ± 0.02 mM) was also determined for the Medium Site

in duplicate using Coulometery (UIC, Model 5011 CO2 Coulometer; Dickson and Goyet, 1994).

4.3.5   **Diagenetic modeling**

Fluxes and sedimentary reaction rates of nutrients and DIC were modeled using the one-

dimensional (1-D) general diagenetic equation (Berner 1980):

$$\frac{\partial C}{\partial t} = -\frac{\partial J}{\partial z} + \Sigma R, \qquad\qquad (4.2)$$

where C is the concentration of a solute in porewater (μM for nutrients, mM for DIC), J is the flux of this dissolved component (mmol m^{-2}d^{-1}), ΣR is the sum of rates of all the processes that affect the concentration of the porewater component (mmol m^{-3}d^{-1}), and z is depth (cm; positive into the bed).

In this study, Equation 4.2 is assumed to be in steady state, and becomes

$$\frac{\partial J}{\partial z} = \Sigma R. \qquad\qquad (4.3)$$

Integrating Equation 4.3 over the length of the sediment interval of interest results in

$$J_B - J_T = \int_{z_T}^{z_B} \Sigma R \, dz, \qquad\qquad (4.4)$$

where z_B is the bottom depth (cm) of the sediment interval of interest and z_T is the top depth (cm) of the sediment interval of interest. The length of the sediment interval, dz, is equal to $z_B - z_T$. The terms on the right-hand side of Equation 4.4, the reaction rate (R) of production or consumption for the dissolved constituent over the length of the sediment interval (dz), is the depth-integrated rates (DIR) of production or consumption for the solute of interest (Burdige 2006). Simply stated, the difference between the calculated flux at the top and bottom of a sediment interval in this model equals the sum of the production and/or consumption reactions

116

within that interval. Furthermore, the solute flux at the SWI is balanced by the *DIR* of production

or consumption in the sediment under steady-state conditions.

As discussed in the Introduction, permeable sediments are subject to dynamic, multi-

dimensional advective flows that enhance solute fluxes over the diffusively driven fluxes that

often characterize fine-grained sediments. For this study, vertical solute fluxes were modeled

using an effective dispersion coefficient (see following section), D_E, to account for the

complicated 3-D hydrodynamics in a simplified 1-D model, similar to Berg et al. (1998), Jahnke

et al. (2005a), Savidge et al. (2016), and Wilson et al. (2016). Fick's First Law was used with an

exponentially decaying D_E coefficient to model multidimensional porewater flow in the

permeable sediments at our two sites (Boudreau 1997):

$$J = -\varphi D_E \frac{dC}{dz}, \tag{4.5}$$

where φ is the sediment porosity (unitless), C is the concentration of the solute (μM for

nutrients, mM for DIC), and z is depth (cm; positive into the bed). The model assumes an

exponential decay of porewater flow with depth below the SWI, based on field observations

(Reimers et al. 2004), flume experiments (Huettel et al. 1996), and analytical solutions (Elliott

and Brooks 1997; Qian et al. 2008) that indicate exponential decay of porewater transport within

permeable sediments.

At each site, the mean concentrations from the three sampling dates at each porewater

depth were fit with a smoothing-spline function (Curve Fitting Toolbox, MATLAB) and

assumed to represent the system at steady state (Figure 4.5A). The first derivative (dC/dz) of

the smoothing-spline function was computed with 0.1 cm vertical resolution from the SWI

(depth = 0) to the greatest porewater sampling depth, and was used to calculate vertical solute fluxes using Equation 4.5 (Figure 4.5B). The profiles of modeled solute fluxes were then used to inversely calculate reaction rates for the solutes of interest with 0.1 cm vertical resolution using Equation 4.4 (Berg et al. 1998; Burdige et al. 2008; Lettmann et al. 2012). This produced a profile of R values for 0.1 cm sediment depth intervals (Figure 4.5C).

4.3.5.1   *Enhanced diffusion coefficients*

Both enhanced diffusion coefficients, D_E, and vertical porewater velocities, v_{pw}, were calculated using data from *in-situ* experiments at both sites collected using the miniTchain (mTc; Fram et al. 2014). The miniTchain is a vertical array of high-precision temperature probes that logged the temperature of the sediment-porewater matrix at both sites (see Fram et al. 2014 and Chapter 3 for full descriptions). By recording the propagation rate and strength at which temperature fluctuations of the overlying water column penetrated the sediment, we were able to statistically solve the 1-D heat transport equation (HTE) for thermal front velocities and effective thermal diffusivities using finite differences and regression fits calculated from a time series of temperature profiles in the sediment (See Chapter 3).

Thermal front velocities were then converted to vertical porewater velocities by applying bulk sediment thermal parameters and sediment porosity (Rau et al. 2012):

$$v_{pw} = v \frac{\rho c}{\rho_w c_w \varphi}. \tag{4.6}$$

where v is the thermal front velocity (cm hr^{-1}), $\rho_w c_w$ is the specific volumetric heat capacity of water (J m^{-3} °C[-1]), and ρc is the bulk heat capacity (J m^{-3} °C[-1]; Rau et al. 2012), the latter defined as

$$\rho c = \varphi \rho_w c_w + (1 - \varphi)\rho_S c_S, \qquad (4.7)$$

where $\rho_s c_s$ is the specific volumetric heat capacity of the solids (J m^{-3} °C^{-1}; Buntebarth and

Schopper 1998).

The porewater velocities calculated using the miniTchain were then used to calculate D_E

coefficients, which are the sums of the enhanced dispersivity term, D_v (cm^2 s^{-1}), and the

sedimentary molecular diffusion term, D_s (cm^2 s^{-1}; Rau et al. 2012):

$$D_E = D_s + D_v. \qquad (4.8)$$

Various empirical relationships have been proposed to describe enhanced dispersion, D_v,

in terms of advective porewater motion (e.g., Nielsen, van Genuchten 1986; Reimers et al. 2004).

For this study, D_v coefficients were calculated using a unified solute-thermal expression that

describes dispersivity as a function of Péclet number and sediment characteristics (see Chapter 3;

Bons et al. 2013):

$$\frac{D_v}{D_s} = \alpha Pe, \qquad (4.9)$$

where α is the dispersivity coefficient (unitless), and Pe is the Péclet number (unitless) defined

as

$$Pe = \frac{|v_{pw}| \cdot L}{D_s}, \qquad (4.10)$$

where L (cm) is the characteristic length scale (e.g., Bear 1972; de Marsily 1986). The characteristic length scale for this study is the length of the miniTchain array used (see Chapter 3). The transport regime is theoretically considered to be convection/advection dominated over the scale of the characteristic length when $Pe > 1$, and conduction/diffusion dominated when $Pe < 1$.

The dispersivity coefficient, α, in Equation 4.9 was empirically determined from the observed increases in effective thermal diffusivities as a result of thermal front velocities at each of the sites. The relationship between effective thermal diffusivity and thermal front velocity is dependent on the unique sediment characteristics of each site (Lu et al. 2009). Values for α of 0.36 and 0.39 was determined for the sediment at the Fine Site and at the Medium Site, respectively.

A logarithmically decaying D_E profile was modeled over the sediment length of porewater profiles (Jahnke et al. 2005b; Qian et al. 2008; Savidge et al. 2016; Wilson et al. 2016) as:

$$D_E = D_{E_{SWI}} e^{-k \cdot z} \tag{4.11}$$

where $D_{E_{SWI}}$ is the enhanced diffusion coefficient at the SWI (cm^2 s^{-1}), z is the sediment depth (cm), and k is:

$$k = \frac{\ln(2)}{d_{1/2}}, \tag{4.12}$$

where $d_{1/2}$ is the half-depth (cm). According to Darcy's law, variations in the magnitude of the porewater transport, and thus the $d_{1/2}$ parameter, are controlled by sediment permeability and the pressure gradient driving flow at the SWI. Therefore, a $d_{1/2}$ value of 5 cm was assumed and used to model flow at the Fine Site, while a larger $d_{1/2}$ value of 10 cm was used to model flow at the more permeable Medium Site.

The enhanced diffusion coefficient calculated using the miniTchain data, $D_{E_{mTc}}$, was used to model $D_{E_{SWI}}$:

$$D_{E_{SWI}} = D_{E_{mTc}} e^{k \cdot z_{mTc}} \tag{4.13}$$

where z_{mTc} is the average sediment depth of miniTchain measurements (cm). The value of $D_{E_{SWI}}$ was then used in Equation 4.11 to create exponentially decaying values of D_E over the desired sediment depths. Differences in z_{mTc} of the field-calculated v_{pw} and $D_{E_{mTc}}$ values at the two sites resulted from differences in the burial depth of the miniTchain. At the Fine Site, v_{pw} and $D_{E_{mTc}}$ values were calculated from two arrays at ~4 cm below the SWI, and from one array at ~13 cm below the SWI. With the miniTchain buried slightly deeper at the Medium Site, v_{pw} and $D_{E_{mTc}}$ values were calculated from two arrays at ~10 cm below the SWI, and from one array at ~19 cm below the SWI (see Chapter 3). As a result, the average depths of field-calculated $D_{E_{mTc}}$ values were 9 cm at the Fine Site and 15 cm at the Medium Site.

Lastly, values for sedimentary molecular diffusion, D_S, were needed to complete calculations for D_E coefficients, and were calculated as

$$D_s = \frac{D_0}{\theta^2},$$ (4.14)

where D_0 is the free diffusion coefficient in water without the presence of a solid matrix (cm^2 s^{-1}), and θ is the sediment tortuosity (McDuff and Ellis 1979; Berner 1980), which is estimated as:

$$\theta^2 = \varphi F,$$ (4.15)

where F is the formation factor (Manheim 1970; Berner 1980). The formation factor (F) is well approximated for sands (Berner 1980) as

$$F = \varphi^{-2}.$$ (4.16)

Free diffusion coefficients (D_o) for seawater at 25°C were used for inorganic nutrients and DIC; coefficients of 8.46×10^{-6} cm^2 s^{-1}, 19.0×10^{-6} cm^2 s^{-1}, 8.9×10^{-6} cm^2 s^{-1}, and 19.8×10^{-6} cm^2 s^{-1} were used for SRP, NO$_x$, Si and NH$_4^+$, respectively (Li and Gregory 1974; Berelson et al. 2005). The D_o coefficient for DIC is dependent on DIC speciation; however, a pH range of 7.5 – 8.1 was measured in nearby carbonate sediments (Drupp et al. 2016), which would result in DIC speciation of more than ~95% bicarbonate. As a result, the D_o coefficient for DIC was estimated using the D_o coefficient of 11.8×10^{-6} cm^2 s^{-1} for bicarbonate at 25°C (Li and Gregory 1974).

4.3.6   *Porewater inventory calculations*

Depth-integrated sediment-porewater inventories for dissolved constituents were calculated at the Medium Site using the Curve Fitting Toolbox, a part of the MATLAB data processing software. First, porewater concentrations from vertical porewater samples were fit using a smoothing spline and integrated from the SWI to 50 cm below the SWI. Resulting integrations were then corrected for sediment porosity and are reported per m^2 of sediment.

4.4   Results

4.4.1   *Sediment characteristics*

Sediment characteristics for the two sites are summarized in Table 4.1. The upper sediment at the Fine Site was determined to be fine to very fine sand, with a phi value of 2.91 and a phi standard deviation of 1.53, indicating poorly sorted sediment (Folk and Ward 1957). Sediment permeability was determined to be $2.33 \pm 1.6 \times 10^{-1}$, while average porosity was 0.59 ± 0.01. The estimated organic carbon content of the upper sediment at the Fine Site was 0.55 ± 0.20 weight percent carbon, and 0.07 ± 0.01 weight percent nitrogen. In the upper sediment at the Medium Site, the estimated organic carbon content was 0.36 ± 0.20 weight percent carbon, and 0.05 ± 0.01 weight percent nitrogen.

4.4.2   *Porewater profiles*

Dissolved organic carbon (DOC) and organic nitrogen (DON) concentrations and molar DOC:DON ratios from the three porewater sampling dates in 2011 at the Medium Site are shown in Figure 4.6. Mean DOC and DON porewater concentrations were highest at ~5 cm below the SWI. The lowest molar DOC:DON ratios (18.8 ± 7) were observed ~5 cm below the SWI, and increased with depth to a maximum of 127 ± 66 approximately 50 cm below the SWI.

Corresponding dissolved inorganic nutrient and DIC porewater concentrations for the same sampling dates as described above at the Medium Site are shown in Figure 4.7. Measured porewater constituents were generally enhanced relative to bottom-water concentrations. Concentrations of DIC peaked ca. 15-20 cm below the SWI, with a concentration of ~2.24 mM. For the first porewater sampling date at the Medium Site, maximum concentrations of SRP (~2.2 µM) and Si (~10 µM) were observed at ~5 cm below the SWI (Figure 4.7A). For the second and third sampling dates, SRP and Si concentrations peaked around 15-25 cm below the SWI, with concentrations of ~2.2 µM and ~8 µM, respectively (Figure 4.7B and C). The highest NH_4^+ concentrations (~2 or 4.5 µM) were observed ~5 cm below the SWI. Unlike the other inorganic nutrients, concentrations of NO_x did not increase from bottom-water concentrations until deeper than ~5 cm below the SWI, and maximum concentrations of ca. $6 - 10$ µM were reached 30-40 cm below the SWI. Concentrations of dissolved inorganic nutrients and DIC generally decreased with depth below their maxima.

Dissolved inorganic nutrient concentrations in porewater samples collected at the Fine Site on three sampling dates in 2013 are shown in Figure 4.8. The clogging of the porewater sampling needle at 11 cm below the SWI on 13 December 2013 prevented porewater collection from that depth. Additionally, the small volume of porewater recovered from 5 and 9 cm below the SWI on 13 December 2013 precluded analysis of SRP.

Porewater concentrations of SRP and Si at the Fine Site were higher and more variable than at the Medium Site. Fine Site porewater concentrations were all enhanced relative to the concentrations of the overlying bottom water, reaching maxima of ~8 µM for SRP and ~45 µM for Si at depths of 7 and 3 cm below the SWI, respectively. Unlike at the Medium Site, nutrient

concentrations at the Fine Site do not distinctly decrease at depths greater than the porewater maxima.

4.4.3   Porewater velocities and dispersion coefficients

Vertical v_{pw} values were estimated using the miniTchain data from both sites. Mean vertical v_{pw} values at 9 cm below the SWI are shown for the 21-day experiment at the Fine Site in Figure 4.9A. The mean v_{pw} value for the entire deployment was $-0.55 \pm 0.25 \text{ cm hr}^{-1}$, with negative velocities indicating upward flow towards the SWI. The mean $|v_{pw}|$ value at this site for the entire deployment was $0.40 \pm 0.18 \text{ cm hr}^{-1}$. Values of v_{pw} at 15 cm below the SWI for the first 21 days of the 80-day deployment at the Medium Site are shown Figure 4.9B. Mean vertical v_{pw} and $|v_{pw}|$ values at 15 cm below the SWI for the entire deployment were $-0.64 \pm 0.54 \text{ cm hr}^{-1}$ and $0.69 \pm 0.47 \text{ cm hr}^{-1}$, respectively. The 80-day v_{pw} record was truncated in Figure 4.9 to highlight results pertaining to the three porewater sampling dates that are the focus of this study.

For use in our diagenetic models, a steady-state $|v_{pw}|$ value was determined for each site as the mean of the $|v_{pw}|$ values calculated for the three porewater sampling dates. The steady-state $|v_{pw}|$ values were then used to model solute-dependent D_E coefficients (see Section 4.3.5.1) at the two sites. Steady-state $|v_{pw}|$ values of 0.54 cm hr^{-1} and 0.86 cm hr^{-1} were determined for 9 cm below the SWI at the Fine Site and 15 cm below the SWI at the Medium Site. Depths of $|v_{pw}|$ values varied because of the different burial depth of the miniTchain at each site (see Section 4.3.5.1). Note, for the third porewater sampling date at the Fine Site (13 December 2013), a mean $|v_{pw}|$ value from the 21-day deployment was used (Figure 4.9A). This porewater sampling occurred during the last day of the miniTchain deployment, and because miniTchain

data analysis requires a 2-day window (see Chapter 3), no values of v_{pw} could be calculated for this sampling date.

Modeled profiles of the D_E coefficients used in our diagenetic models for the Fine and Medium Sites are shown in Figure 4.10A, and corresponding profiles of modeled $D_E:D_S$ ratios for both sites are shown in Figure 4.10B. At the Fine Site, D_E coefficients for SRP and Si at the SWI were modeled as 308 and 227 times greater than D_S (see Section 4.3.5.1). For the deepest porewater sampling depth (11 cm below the SWI), modeled D_E coefficients for SRP and Si at the Fine Site were 67 and 49 times greater than D_S, respectively. Values for D_E coefficients at the SWI at the Medium Site were larger than at the Fine Site, with D_E coefficients 369, 591, 435, 220 and 230 times greater than D_S for DIC, SRP, Si, NH_4^+ and NO_x, respectively. At the deepest porewater sampling depth at the Medium Site (~50 cm below the SWI), modeled D_E coefficients were 12, 19, 14, and 7 times greater than D_S for DIC, SRP, Si and DIN species (NH_4^+ and NO_x), respectively.

4.4.4 *Nutrient fluxes and reaction rates*

Depth-dependent vertical nutrient flux (J) and reaction rate (R) profiles were modeled under steady-state conditions for each solute at the Medium Site (Figure 4.11) and the Fine Site (Figure 4.12). Solute fluxes at the SWI and solute DIR are summarized in Table 4.2. Error bars on the mean flux and DIR estimates were calculated as the standard deviation of the fluxes or DIR values calculated for each of the three individual porewater sampling dates.

At the Fine Site, the modeled SRP flux at the SWI of -0.36 mmol m^{-2}d^{-1} was ~1.7 times greater than at the Medium Site, while the Fine Site Si flux of about -9 mmol m^{-2}d^{-1} at the SWI was ~11.5 times greater than at the Medium Site. At the Medium Site, the DIC flux was

modeled as -11.5 ± 9.5 mmol m^{-2}d^{-1}, while NH$_4^+$ and NO$_x$ fluxes were -0.35 ± 0.38 and 0.01 ± 0.05 mmol m^{-2}d^{-1}, respectively.

Depth-dependent reaction rates in the sediment were calculated as the production or consumption of the solute required to balance the divergence or convergence of the solute fluxes within a specified depth interval (see Section 4.3.5.). At the Medium Site, diagenetic models revealed production of DIC, SRP, and Si in the upper ~15 cm of the sediment. Rates for DIN species were more complicated, with production of NH$_4^+$ and consumption of NO$_x$ in the top ~10 cm of sediment, and production of NO$_x$ and consumption of NH$_4^+$ occurring below this depth. At the Fine Site, models indicate the production of Si in the upper 4 cm of the sediment, with much smaller Si consumption rates below that depth. Profiles of SRP reaction rates were more varied and alternated between zones of production (0-4 cm and ~6-9 cm below the SWI) and zones of consumption (~4-6 cm and ~9-11 cm below the SWI).

4.5 Discussion

4.5.1 *Relationship between hydrodynamic forcing and porewater transport*

Advective flows in permeable sediments are governed by Darcy's law (e.g., Boudreau 1997; Boudreau and Jorgensen 2001), and expected to increase with both increasing sediment permeability and increasing hydrodynamic forcing. Thus, the weak and relatively constant V_{bed} at the Fine Site ($V_{bed} = 0.03 \pm 0.02$ m s^{-1}) resulted in weak and relatively constant values of $|v_{pw}|$, and corresponding D_E coefficients, over the 21-day deployment (Figure 4.9). There was no significant correlation between V_{bed} and $|v_{pw}|$ at the Fine Site (R^2 = 0.02; Figure 4.13). As expected from the greater permeability and hydrodynamic flows that characterized the Medium Site, larger $|v_{pw}|$ values and, therefore, larger D_E coefficients were determined at this site than at the Fine Site (Figure 4.9). However, despite greater permeability and stronger, more variable

hydrodynamic conditions ($V_{bed} = 0.20 \pm 0.04$ m s^{-1}; $H_{sig} = 0.83 \pm 0.14$ m), $|v_{pw}|$ values and corresponding D_E coefficients were only weakly correlated with H_{sig} (R$^2 = 0.22$) and V_{bed} (R$^2 = 0.16$; Figure 4.13). The weak relationship between porewater transport and water-column hydrodynamics determined in this study confirms previous findings at the Medium Site of weak relationships between porewater flow and hydrodynamic forcing (Hebert et al. 2007). Furthermore, Burdige et al. (2008) were also unable to discern any patterns linking water-column hydrodynamics to calculated advective flow parameters in permeable sediments in the Bahamas.

In our study, several factors may have contributed to the poor relationships between D_E and water-column hydrodynamics at the two sites. The combination of lower sediment permeability and consistently weak flows at the Fine Site likely resulted in no discernable relationship between porewater velocities and water-column hydrodynamics over the 21-day deployment. Additionally, porewater transport at the Fine Site may have occurred due to bioturbating organisms, which were observed at the site but not quantified in this study (Chapter 2). Porewater transport associated with bioturbation would not be correlated with water-column hydrodynamics and may have negated any weak link between hydrodynamics and porewater transport at the site.

Also, as detailed in Chapter 3, the statistical approach used to estimate porewater velocities from miniTchain data uses a least-squares fit over a two-day window to statistically solve for advective and diffusive transport coefficients with 95% confidence intervals. A moving two-day window was chosen to ensure a statistically robust fit, while attempting to capture any changes in water-column hydrodynamics that may be driving porewater flows. However, the two-day time interval may not have been short enough to capture temporal changes in the hydrodynamics at the sites. Effects of shorter time intervals were also tested in the analysis of the

temperature-depth data, but resulted in the same overall trends in porewater velocities with larger error-bar estimates (data not shown). For example, using a one-day instead of two-day window in the analysis increased error bars on the estimates about 75% without changing the overall trends or magnitude of the porewater velocities.

The burial depth of the miniTchain may also have negatively impacted any correlation between porewater velocities and water-column hydrodynamics at the Medium Site. Permeable sediments are characterized by complex, multi-dimensional flow that decreases in strength deeper into the sediment (e.g., Huettel et al. 1996; Reimers et al. 2004). While the miniTchain at the Fine Site was buried as close to the SWI as possible (top thermistor 1 cm below the SWI), a deeper burial depth at the Medium Site (top thermistor 7 cm below the SWI) was needed to avoid exposure of the miniTchain due to sand ripple migration (Fram et al. 2014). It is possible that the deeper burial depth at the Medium Site weakened the potential relationship between porewater transport and the overlying water-column hydrodynamics, given that $|v_{pw}|$ decreases with depth.

Additionally, unlike the relatively flat sediment at the Fine Site, small disorganized sand ripples characterized the sediment surface of the Medium Site. In laboratory flume studies using permeable sediments, the presence of sand ripples results in distinct spatial patterns of porewater flows (see Chapter 2 and references within); therefore, variation between sand ripple crest and trough in the sediment above the miniTchain was expected to influence flow patterns. A stereo camera system was deployed to capture the changing SWI during experiments to determine if direction or strength of vertical porewater velocities was driven by location of the miniTchain below a crest or a trough. However, complications arose in the collection and processing of the images of the rapidly changing SWI (see Fram et al. 2014 for details). Briefly, lasers were used

to indicate structures on the SWI, but the lasers were difficult to see during daylight conditions. Additionally, the position of the cameras was suspected to have shifted during the deployment. As a result, it is not possible to tell if the miniTchain was located below a crest or a trough throughout most of the deployment, and the potential influence of varying sediment topography on porewater flows calculated in this study could not be assessed.

The number of variables that may have contributed to the weak relationship between measured water-column hydrodynamics and porewater transport in our study highlights the complexity of flow in permeable sediments. The complex flow regimes of these environments can be further complicated by the addition of larger-scale circulation processes, such as internal reef circulation (e.g., Tribble et al. 1990) and submarine groundwater discharge (Moore et al. 2002). The large sand patch at the Medium Site consists of carbonate reef sand deposited on lithified reef structures, creating a complicated spur and groove topography (Figure 4.1). The porosity of these reef frameworks, despite being consolidated structures, has been observed to rival the ~0.5 porosity measured in permeable sediments (Tribble et al. 1990). However, the permeability of reef frameworks is not homogenous, with flow predominately through high permeability zones such as cavities and rubble layers in the reef (Parnell 2011). Flow through these types of conduits may be responsible for the previously observed inconsistent presence of DO ~20 to 50 cm below the SWI at the Medium Site (Fogaren 2010; Figure 4.14A). Additionally, it is possible that the observed net porewater flow from the sediment to the water column (Chapter 3) results from larger circulation within the reef framework driven by a combination of wave setup, tides, regional currents, groundwater flow, etc. These larger circulation processes need to be quantified to determine their effect on flow in permeable sediments in relatively complex porous frameworks such as coral reefs.

4.5.2 *Modeling advective transport in permeable sediments*

Other nearshore studies have used exponentially decaying porewater transport to represent the complex 3-D porewater flows of permeable sediments in simpler 1-D models. Jahnke et al. (2005) used an exponentially decaying porewater transport parameter, paired with measured opal dissolution rates from sediment core incubations, to recreate observed Si porewater profiles in permeable sediments on the South Atlantic Bight (SAB). In their diagenetic models, porewater transport was modeled using an exponentially decaying D_E coefficient. The results from this approach were compared with results that used an exponentially decaying nonlocal exchange (NLE) parameter to represent advective transport between porewater and the overlying bottom water (e.g., Boudreau 1997). Both of their modeling approaches required a $d_{1/2}$ of 2 cm (see Section 4.3.5.1) to recreate observed porewater profiles. More recently, exponentially decaying D_E coefficients were used to explain observed changes in the vertical structure of temperature-depth profiles in the SAB (Savidge et al. 2016; Wilson et al. 2016). However, they found that an exponentially decaying D_E coefficient with a $d_{1/2}$ of 8 cm was needed to best model the enhanced porewater transport they observed over the top ~40 cm of sediment.

In their study of carbonate dissolution rates in permeable sediments in the Bahamas, Burdige et al. (2008) modeled advective transport to decay exponentially using a NLE parameter in their diagenetic models. They used stoichiometrically predicted DO, DIC and total alkalinity reactions, in conjunction with measured *DIRs* for these solutes, to determine a mean $d_{1/2}$ value of 9 cm (range of $1.9 - 35.4$ cm) for their study sites; however, it should be noted that this mean $d_{1/2}$ value was calculated for sediment that included various degrees of seagrass cover. At their

site without seagrass cover, $d_{1/2}$ values of 13.7 and 1.9 cm were determined for consecutive sampling years.

Although these studies all incorporated exponentially decaying porewater transport in 1-D diagenetic models, there were differences in the $d_{1/2}$ values used to model the advective transport decay. According to Darcy's Law, differences in the magnitude of flow, and thus values of $d_{1/2}$, are controlled by the permeability of the sediment and the pressure gradient driving flow at the SWI. Therefore, differences in the $d_{1/2}$ value in these studies should reflect sediment characteristics and hydrodynamic conditions at the sites. However, Burdige et al. (2008) did not find any correlation between hydrodynamic conditions and $d_{1/2}$ values at their sites, again highlighting the complexity of flow in these environments.

In our study, the $d_{1/2}$ values of 5 cm at the Fine Site and 10 cm at the Medium Site are consistent with the $d_{1/2}$ values from the other diagenetic models (described above) that incorporate exponentially decaying advective transport. Additionally, in the same large sand patch at the Medium Site as our study, Hebert et al. (2007) used an *in-situ* fluorescein dye experiment to estimate porewater transport. They measured transport rates of $0 - 5 \text{ cm hr}^{-1}$ at ~15 cm below the SWI, with maximum D_E coefficients 2-3 orders of magnitude greater than that of sedimentary molecular diffusion. This agrees well with our calculated solute D_E coefficients ~$80 - 210$ times greater than D_S at 15 cm below the SWI, calculated at the Medium Site using a mean steady-state porewater flow of 0.86 cm hr^{-1} (Figure 4.10).

4.5.3 *Nutrient and DIC fluxes and sedimentary reaction rates*

Depth-dependent fluxes (J) and sedimentary reaction rates (R) were calculated at the Medium (Figure 4.11) and the Fine Site (Figure 4.12) using field-constrained enhanced

diffusion-reaction models; solute fluxes at the SWI (J_{SWI}) and depth-integrated rates (*DIR*) of production and consumption for solutes over the length of the models are reported in Table 4.2. In 1-D diagenetic models under steady-state conditions, J_{SWI} is balanced by the *DIR* for the solute in the sediment because fluxes at the bottom of the model are typically negligible (Burdige 2006). Therefore, discrepancies between values of J_{SWI} and *DIR* can indicate that the diagenetic model does not include the entire geochemically relevant zone for the solute of interest, and that zone may need to be extended deeper in the sediment. At the Medium Site, *DIR* values roughly balanced J_{SWI}, suggesting that the depth of our model encapsulates most of the processes affecting the measured solutes at the site. However, the relatively large difference between estimates of J_{SWI} and *DIR* for SRP observed at the Fine Site suggests that the 11-cm depth did not cover the entire geochemically relevant area of the sediment SRP. This is not surprising given the redox-sensitive and particle-reactive nature of P (Ruttenberg and Berner 1993; Ruttenberg et al. 2014), which can lead to changes in SRP inventories post-remineralization.

At the Medium Site, modeled values of *R* for DIC, SRP and Si were very strongly correlated (DIC-SRP $R^2 = 0.97$, DIC-Si $R^2 = 0.93$, Si-SRP $R^2 = 0.96$). These reaction rates were also greatest in the upper sediment, suggesting that the remineralization of sedimentary organic matter is the dominant process controlling DIC, SRP and Si inventories. Conversely, SRP and Si porewater reaction rates at the Fine Site were very weakly correlated (SRP-Si $R^2 = 0.15$), indicating changes in regenerated Si and/or SRP inventories post-remineralization. Profiles of Si production rates in the uppermost sediment at the Fine Site suggest porewater inventories result from the remineralization of sedimentary organic matter associated with biogenic Si (see Section 4.5.5). However, the models produced an erratic profile for SRP production and consumption rates in the sediment, implying that abiotic processes such as sorption/desorption and mineral

formation (Ruttenberg and Berner 1993; Ruttenberg et al. 2014) may be affecting SRP inventories at the Fine Site. The dynamics of porewater DIN speciation at the Medium Site are complicated and may reflect extensive post-remineralization alteration, as below in Section 4.5.4.2.

For this study, reported fluxes at the SWI for the two sites assume that nutrient and carbon fluxes are transported to/from the overlying water column without being consumed at the SWI. This may not be a valid assumption given that these sediments occur in shallow areas where appreciable levels of photosynthetically available radiation (PAR) can reach the surficial sediment, allowing epi-benthic and/or endo-benthic photosynthesis to occur. Studies on the South Atlantic Bight revealed that benthic primary production (BPP) can influence benthic exchange rates, even reversing fluxes of DO and nutrients at the SWI (Marinelli et al. 1998; Jahnke et al. 2000). Therefore, it is important to note that our models predict fluxes at the SWI but cannot confirm the fate of these constituents. Additional measurements (e.g., benthic chambers, eddy-covariance) are needed in conjunction with sedimentary reaction rate measurements to assess the effects of BPP on nutrient and carbon dynamics at our sites.

Conversely, fluxes calculated using benthic flux chambers and eddy-covariance techniques may not accurately reflect sedimentary remineralization rates, highlighting the need for a combination of methodological approaches to better understand the dynamics of these environments, and to isolate the relative importance of each component. As a result, it is important to understand the assumptions of the approach used when comparing fluxes and sedimentary remineralization rates from different studies. A summary of results from different field-based approaches used to estimate carbon and nutrient fluxes, and corresponding

134

sedimentary reaction rates in permeable sediments are summarized in Table 4.3. Relevant methodological details and assumptions are also included in Table 4.3.

Given the number of site-specific variables (i.e., different measurement techniques, organic matter loadings, hydrodynamic conditions, variations in PAR), our flux and *DIR* results are in reasonable agreement with other estimates from the SAB, the German Bight (GB) and field sites near Lee Stocking Island (LSI) in the Bahamas. This study and others indicate that nutrient or carbon fluxes from the sediment to the water column are substantial. It is interesting to note that our model results indicate small or non-existent NO_x fluxes from the water column to the sediment at the Medium Site. The complicated dynamics of DIN species at the Medium Site may result from the poorly understood flow dynamics (see Section 4.5.1) and the high rates of denitrification suspected to occur in the sediment (see Section 4.5.4.2). Nutrient SWI fluxes estimated for the Fine Site in this study are slightly larger than estimates from other sites. However, as previously mentioned, our models do not confirm the actual transport of solutes from the sediment to the water column.

The potential strength of combining different measurement approaches can be illustrated by combining our field-constrained enhanced diffusion-reaction model results at the Fine Site with eddy-covariance measurements for DO during 13-17 May 2016 by Dr. M. Huettel. Although not occurring at the same time as the experiments in this study, the processes controlling nutrient cycling at the site are expected to have been approximately the same during the eddy-covariance measurements. DO fluxes measured during daylight hours are assumed to reflect net oxygen consumption/production resulting from a combination of remineralization and BPP, while nighttime DO measurements should provide sedimentary oxygen consumption rates due solely to remineralization processes. Over the course of the eddy-covariance deployment, the

sediments were determined to be a source of DO to the water column during the day ($-112 \pm$ 9 mmol m^{-2}d^{-1}; n = 2), and a sink for DO during the night (25 ± 6 mmol m^{-2}d^{-1}; n = 2; Huettel, pers. comm.), similar to trends observed by Marinelli et al. (1998). Thus, BPP may be an important aspect of nutrient cycling in these sediments that was not constrained using our modeling approach.

Additionally, nighttime sedimentary oxygen consumption rates paired with stochiometric nutrient molar ratios can be used to estimate remineralization rates in the sediment at the Fine Site. Assuming a locally measured DO:P molar ratio of $-103:1$ (Laws N:P molar ratio for Mamala Bay (Laws et al. 1984)) or a Redfield DO:P molar ratio of $-138:1$ (Redfield et al. 1963), sedimentary respiration rates of 25 mmol m^{-2}d^{-1} (nighttime eddy-covariance measurements) are associated with SRP fluxes of -0.18 and -0.24 mmol m^{-2}d^{-1}, respectively. These are in reasonable agreement with, but lower than, SRP fluxes at the SWI of -0.36 mmol m^{-2}d^{-1} estimated using our modeling approach. Thus, although challenging to make, a combination of field and modeling techniques is needed to better understand the different processes (i.e., benthic fluxes, rates of BPP, and sediment remineralization rates) that control nutrient cycling in these environments.

4.5.4   *Nitrogen cycling in permeable sediments*

As organic matter undergoes remineralization in sediments, dissolved inorganic nitrogen (DIN) in its reduced form, NH_4^+, is released to the porewater (Boudreau and Jorgensen 2001). In fine-grained anoxic sediments, this process generally results in the buildup of NH_4^+ in the porewater with depth, eventually leveling off at a maximum concentration (e.g., Burdige 2006). However, in the presence of dissolved oxygen (DO), NH_4^+ undergoes a two-step nitrification process, first oxidizing NH_4^+ to nitrite (NO_2^-) and then nitrate (NO_3^-) (e.g., Froelich et al. 1979;

Devol 2015). Thus, in fine-grained sediments with ample organic matter input, NO_3^- is typically present only in the oxygenated uppermost sediment layer. Moreover, organic matter remineralization after DO has been consumed continues via denitrification, resulting in a decrease of NO_3^- concentrations and, ultimately, the production of N_2 gas, resulting in a net N removal from the system (Devol 2015).

4.5.4.1   *Nitrogen speciation as an indicator of sediment oxygenation*

Profiles of DO that correspond to measured DIC and nutrient profiles are not available at the Medium Site for this study. Therefore, we use the ratio of the concentrations of DIN in the reduced form, NH_4^+, versus the oxidized form, NO_x ($NO_3^- + NO_2^-$) (Tribble et al. 1990; Falter and Sansone 2000a; Sansone et al. 2017) to estimate the relative degree of oxygenation of the sediments (Figure 4.14B). The vertical distribution of DIN species at the Medium Site was expected to be similar to that of fine-grained sediments: the presence of NO_x in the porewater of only the oxygenated upper sediment, and increasing NH_4^+ concentrations below the oxygen penetration depth. However, NH_4^+ concentrations at the Medium Site peak slightly in the upper sediment (~5 cm below the SWI) and concentrations of NO_x are found deeper in the sediment (Figure 4.14C). Elevated concentrations of NH_4^+ and a lack of NO_x in the upper sediment indicates the absence of DO at this depth, at least at the microenvironment scale (e.g., Sansone and Chanton 1993; Falter and Sansone 2000b). Conversely, the presence of NO_x and lack of NH_4^+ from ca. 7 to 50 cm below the SWI suggests the presence of DO at these depths.

Thus, the vertical DIN speciation at the Medium Site indicates a seemingly contradictory situation: both a DO upper-penetration depth of less than ~5 cm, and the presence of DO deeper in the sediment. However, DO profiles previously collected at the Medium Site are consistent with this and indicated the decrease of DO in the upper ~10 cm of the sediment, as well as the

presence of DO deeper in the sediments (Figure 4.14A; Fogaren et al. 2013). For the previously

collected data, the shallowest DO porewater samples were ~10 cm below the SWI; therefore, we

did not have the vertical resolution necessary to capture the potential DO disappearance close to

the SWI, as suggested by the DIN profiles (Figure 4.14C). However, high-resolution

voltammetric profiles of DO in the upper sediment (Sansone et al. 2008) at the Medium Site on

April 19, 2011 revealed that DO disappeared by ~5 cm below the SWI (Figure 4.14A). This

observed lack of DO at ~5 cm below the SWI is consistent with the observed presence of NH_4^+

and absence of NO_x at this depth in the current study (Figure 4.14C).

The absence of DO in the upper sediment at the Medium Site may result from greater

organic matter input and higher remineralization rates at this depth than deeper in the sediment.

This is consistent with the observed peaks in porewater DOC and DON concentrations at this

depth (Figure 4.6), peaks in remineralization end-products (Figure 4.7), modeled

remineralization rates in the upper sediment (Figure 4.11), and the traditional paradigm for

organic matter input to sedimentary environments (e.g., Burdige 2006). Conversely, lower rates

of DIC, SRP and Si remineralization below ~15 cm at the Medium Site (Figure 4.11) may be due

to organic matter limitation. In sediments with ample organic-matter input, the remineralization

of organic matter typically occurs in the following thermodynamically predictable order: aerobic

respiration, denitrification, manganese reduction, iron reduction, sulfate reduction and

methanogenesis (e.g., Froelich et al. 1979; Emerson and Hedges 2003). The presence of the two

most thermodynamically favorable terminal electron acceptors, DO and NOx, below ~20 cm

suggests that remineralization at these depths may be limited by the rate of labile organic matter

delivery. Additionally, the presence of a relatively more refractory dissolved organic matter pool

(higher molar DOC:DON ratios, Figure 4.6C) deeper in the sediment suggests that less labile organic matter is undergoing remineralization at these depths (e.g., Burdige 2006).

The vertical DO structure observed in the sediment at the Medium Site somewhat resembles the vertical DO structure of the open-ocean water column (i.e., DO and organic matter are delivered from above; remineralization occurs via aerobic respiration, which results in an oxygen minimum zone (OMZ) where the ratio of organic matter to DO delivery is greatest; and below the OMZ, DO is laterally injected to the system at a greater rate than organic matter is delivered (e.g., Libes 2009)). It is possible that the similar DO structure at the Medium Site develops as dissolved constituents, such as DO, are transported to the deeper sediment through the adjacent reef framework, while particulate organic matter is filtered out and retained in the upper sediment. A sedimentary OMZ would then develop in the upper sediment where the rate of organic matter delivery is greater than the rate of DO delivery.

4.5.4.2   *Denitrification in permeable sediments*

Regardless of DIN speciation, porewater concentrations of DIN at the Medium Site are lower than predicted using N:P stoichiometric ratios (Figure 4.15A). As organic matter undergoes remineralization, inorganic nutrients are generally released to the porewater in the stoichiometric ratios at which they were incorporated in the source organism (e.g., Redfield et al. 1963). The locally measured N:P molar ratio of 10.9:1 determined by Laws et al. (1984) for phytoplankton for Mamala Bay, Oahu is indicated by the dotted line in Figure 4.15A, and the Redfield ratio for N:P of 16:1 (Redfield et al. 1963) is indicated with a dashed line. Nearly all of the DIN:P data in Figure 4.15A fall below the Laws and Redfield ratios, indicating preferential N loss with respect to P.

Sedimentary inventories of remineralized dissolved inorganic nutrients can be altered by biotic and abiotic processes after remineralization; therefore, differences in observed and stoichiometrically predicted nutrient inventories can reveal post-remineralization alterations. Both the Laws and Redfield N:P ratios for porewater samples indicate that the sediment at the Medium Site is either a sink for N or a source of P. Given the particle-reactive nature of P (e.g., Ruttenberg et al. 2014), it is unlikely that the sediments are a source of dissolved P.

Previous studies indicate that appreciable amounts of denitrification may occur in permeable shelf environments (Tribble et al. 1990; Santos et al. 2012a; Devol 2015). For example, Santos et al. (2012a) measured denitrification rates in carbonate sands using sediment columns subject to weak, intermediate, and strong advection rates. The highest denitrification rates occurred in sediments subject to intermediate advection rates, and this was attributed to the increased prevalence of microenvironments with steep DO gradients under these flow conditions (Rao et al. 2007; Santos et al. 2012a). From these experiments, the authors estimated that ~75% of the DIN produced from remineralization in such environments is lost to subsequent denitrification.

Stoichiometric relationships were used to estimate the amount of DIN lost from the sediment at the Medium Site. Porewater SRP profiles (Figure 4.16A) were first multiplied by the Laws or Redfield N:P molar ratios to create stoichiometrically predicted DIN profiles (dashed and dotted profiles in Figure 4.16B). Depth-integrated DIN inventories (see Section 4.3.6) were then calculated for the predicted Laws ratio profile, the predicted Redfield ratio profile, and the field-measured DIN profile. The "missing" nitrogen, N^*, was calculated in percent as:

$$N_P^* = \frac{DIN_{N:P\ inventory} - DIN_{measured\ inventory}}{DIN_{N:P\ inventory}} \times 100\%,\qquad(4.17)$$

where $DIN_{N:P\ inventory}$ is the depth-integrated DIN inventory calculated using the Laws- or Redfield-predicted profiles, and $DIN_{measured\ inventory}$ is the depth-integrated DIN inventory calculated using measured porewater concentrations. This calculation uses similar to the sedimentary adaptation (Sansone et al. 2017) of the water-column N^*concept developed by Gruber and Sarmiento (1997). Positive values of N_P^* indicate net DIN loss from the system, and negative values indicate net production of DIN in the system. For the three porewater sampling dates, the use of the Laws ratio in Equation 4.17 suggests that 58 ± 3 % of the remineralized DIN was lost, whereas using the Redfield ratio suggests 71 ± 2 % of the remineralized DIN was lost from the sediment.

Porewater volume limitations did not allow for DIN analysis at the Fine Site. However, as part of a simultaneous experiment (Chapter 2) in which porewater samples were collected on 11 December 2013 from 5 cm below the SWI, concentrations of total dissolved N (TDN) and Si were well correlated ($R^2 = 0.72$, n = 10). The correlation between TDN and Si, presumably from the remineralization of organic matter associated with biogenic Si (see Section 4.5.5), may reflect less denitrification at the Fine Site than at the Medium Site.

4.5.5   *Biogenic silica cycling in permeable sediments*

Linear DIC-nutrient relationships have been observed in porewaters of nearby carbonate sediments (Tribble et al. 1990; Fogaren et al. 2013; Sansone et al. 2017), and may be attributed to sedimentary recycling of organic matter, including that associated with the biogenic Si in organisms such as diatoms and siliceous sponges. Concentrations of Si at the Medium Site were weakly correlated with DIC concentrations ($R^2 = 0.29$, n = 21; data not shown), although they were strongly correlated with SRP concentrations (Figure 4.15B; $R^2 = 0.74$, n = 21). These correlations suggest that sedimentary dissolved Si production at this site is also associated with

organic matter remineralization. However, the weaker DIC-SRP relationship at this site suggests that the inventory of regenerated DIC may be subsequently changed by carbonate dissolution and/or production (e.g., Tribble et al. 1990; Drupp et al. 2016).

At the Fine Site, dissolved Si was also correlated with dissolved SRP (Figure 4.15B; $R^2 =$ 0.51, n = 14), suggesting that the Si at this site is also derived from remineralization of organic matter associated with biogenic Si. This was also suggested in a simultaneous experiment (Chapter 2) in which porewater samples (n = 10) collected on 11 December 2013 from 5 cm below the SWI revealed a very strong Si-P correlation ($R^2 = 0.89$). The weaker Si-P correlation observed during the current study may have resulted from the larger range of sample depths (3-11 cm), which typically result in more variable redox conditions, and subsequent increased sorption and desorption of particle-reactive P on sediment surfaces (e.g., Keil and Hedges 1993).

Although, direct measurements of the amount of organic matter in sediments were not made in this study, stochiometric Si ratios of porewater can be used to estimate the relative amount of siliceous to non-siliceous organic matter undergoing remineralization in the sediment via a two-endmember mixing curve. Locally measured molar ratios of organic matter sources that include Si measurements are unavailable; however, the Redfield ratio concept has been extended to planktonic diatoms to yield a C:Si ratio of ~7.7:1 and a Si:P ratio of ~15:1 (Brzezinski 1985). For this study, the amount of Si-associated organic matter undergoing remineralization was assessed only using dissolved Si:P ratios, given the weaker DIC:Si relationship observed at the Medium Site and the lack of DIC data at the Fine Site.

At the Fine Site, Si:P molar ratios (15.4 ± 10.0, n = 15) are scattered around the stoichiometrically predicted ~15:1 Si:P molar ratio for planktonic diatoms (dashed line in Figure 4.15B), with the scatter likely due to the post-remineralization altering of P inventories

(discussed above). This reaffirms stochiometric estimations from a simultaneous experiment that the majority of the organic matter remineralized (Si:P molar ratio = $14.6 \pm 2.1, n = 10$) at this site is associated with planktonic diatoms (Chapter 2). However, at the Medium Site, a Si:P molar ratio of ~5.4:1 is observed (Figure 4.15), indicating that only about a third of the organic matter at this site may be associated with planktonic diatoms. The different Si:P molar ratios at the Fine and Medium Site suggest that different sources of organic matter are being remineralized at the two sites. However, additional field-based measurements are needed to characterize organic matter sources undergoing remineralization at both sites to better constrain stochiometric calculations.

4.6   Summary and future work

Steady-state 1-D enhanced diffusion-reaction porewater models were constrained using *in-situ* porewater transport measurements to estimate depth-dependent solute fluxes and remineralization rates in permeable sediments. Porewater transport rates in this study were determined to have a weak or no relationship with hydrodynamic parameters, suggesting that unforeseen and unquantified hydrodynamic processes (e.g., wave setup, tides, regional currents, groundwater flow, etc.) may be driving flow in such environments. At the Medium Site, these larger-scale processes were speculated to be responsible for the observed anoxic porewater layer in the upper sediment that is vertically stratified between two oxic layers. It is unknown how common this type of vertical redox structure is in permeable sediments of carbonate coral-reef frameworks; therefore, further sampling is needed to determine the prevalence and cause of this redox structure before we can determine its general effects on organic matter remineralization in such environments.

DIC and nutrient fluxes calculated at the SWI using our models agreed reasonably well with other field-based approaches for measuring fluxes in permeable sediments of the South Atlantic Bight, the German Bight and the Bahamas. However, when comparing flux estimates and sedimentary remineralization rates between studies, it is necessary to understand the assumptions and limitations of the approaches used. For instance, while the diagenetic models in this study calculated fluxes at the SWI, they cannot confirm the transport and fate of the remineralized constituents. Conversely, flux measurements made using benthic chambers may not accurately reflect sedimentary remineralization rates in environments with benthic primary production. The strength of combining different field-based methodological approaches to better understand the dynamics of these environments, and to isolate the relative importance of the different processes, was illustrated at the Fine Site. Eddy-covariance techniques for DO indicated that benthic primary production, a process not detectable using our models, may play a significant role in the cycling of nutrients and carbon at the site. Thus, methodological approaches capable of quantifying rates of benthic primary production should be included in future field-based approaches at sites with PAR-impacted sediments. Additionally, future modeling efforts would benefit from site-specific organic matter characterization to better constrain the processes responsible for the alteration of regenerated nutrients post-remineralization.

4.7 References

Bear, J. 1972. Dynamics of fluids in porous media., American Elsevier Pub. Co.

Berelson, W. M., M. Prokopenko, F. J. Sansone, a. W. Graham, J. McManus, and J. M. Bernhard. 2005. Anaerobic diagenesis of silica and carbon in continental margin sediments: Discrete zones of TCO2 production. Geochim. Cosmochim. Acta **69**: 4611–4629. doi:10.1016/j.gca.2005.05.011

Berg, P., and K. J. McGlathery. 2001. A high-resolution pore water sampler for sandy sediments. Limnol. Oceanogr. **46**: 203–210. doi:10.4319/lo.2001.46.1.0203

Berg, P., N. Risgaard-Petersen, and S. Rysgaard. 1998. Interpretation of measured concentration profiles in sediment pore water. Limnol. Oceanogr. **43**: 1500–1510. doi:10.4319/lo.1998.43.7.1500

Berg, P., H. Røy, F. Janssen, V. Meyer, B. B. Jørgensen, M. Huettel, and D. De Beer. 2003. Oxygen uptake by aquatic sediments measured with a novel non-invasive eddy-correlation technique. Mar. Ecol. Prog. Ser. **261**: 75–83. doi:10.3354/meps261075

Berner, R. A. 1980. Early Diagenesis: A Theoretical Approach, Princeton University Press.

Bons, P. D., B. P. Van Milligen, and P. Blum. 2013. A general unified expression for solute and heat dispersion in homogeneous porous media. Water Resour. Res. **49**: 6166–6178. doi:10.1002/wrcr.20488

Boudreau, B. P. 1997. Diagenetic models and their implementation. Modelling transport and reactions in aquatic sediments,.

Boudreau, B. P., M. Huettel, S. Forster, and others. 2001. Permeable marine sediments: Overturning an old paradigm. Eos (Washington. DC). **82**: 133–136. doi:10.1029/EO082i011p00133-01

Boudreau, B. P., and B. B. Jorgensen. 2001. The Benthic Boiundary Layer: Transport Processes and Biogeochemistry, B.P. Boudreau and B.B. Jorgensen [eds.]. Oxford University Press.

Breitzke, M. 2000. Acoustic and elastic characterization of marine sediments by analysis, modeling, and inversion of ultrasonic P wave transmission seismograms. J. Geophys. Res. **105**: 21,411-21,430. doi:http://dx.doi.org/10.1029/2000JB900153; doi:10.102

Brzezinski, M. A. 1985. The Si:C:N ratio of marine diatoms: interspecific variability and the effect of some environmental variables. J. Phycol. **21**: 347–357. doi:10.1111/j.0022-3646.1985.00347.x

Buntebarth, G., and J. R. Schopper. 1998. Experimental and theoretical investigations on the influence of fluids, solids and interactions between them on thermal properties of porous rocks. Phys. Chem. Earth **23**: 1141–1146. doi:10.1016/S0079-1946(98)00142-6

Burdige, D. J. 2006. Geochemistry of Marine Sediments, Princeton University Press.

Burdige, D. J., R. C. Zimmerman, and X. Hu. 2008. Rates of carbonate dissolution in permeable sediments estimated from pore-water profiles: The role of sea grasses. Limnol. Oceanogr. **53**: 549–565. doi:10.4319/lo.2008.53.2.0549

Campbell, W. H., P. Song, and G. G. Barbier. 2006. Nitrate reductase for nitrate analysis in water. Environ. Chem. Lett. **4**: 69–73. doi:10.1007/s10311-006-0035-4

Devol, A. H. 2015. Denitrification, anammox, and N2 production in marine sediments. Ann. Rev. Mar. Sci. **7**: 403–23. doi:10.1146/annurev-marine-010213-135040

Dickson, A. G., C. L. Sabine, and J. R. Christian. 2007. Guide to Best Practice for Ocean CO2 Measurements. PICES Spec. Publ. **3**: 191.

Dickson, A., and C. Goyet. 1994. Handbook of methods for the analysis of the various parameters of the carbon dioxide system in sea water.

Drupp, P. S., E. H. De Carlo, and F. T. Mackenzie. 2016. Porewater CO2-carbonic acid system chemistry in permeable carbonate reef sands. Mar. Chem. **185**: 48–64. doi:10.1016/j.marchem.2016.04.004

Elliott, H., and N. H. Brooks. 1997. Transfer of nonsorbing solutes to a streambed with bed forms: Theory. **33**: 123–136.

Emerson, S., and J. Hedges. 2003. Sediment diagenesis and benthic flux, p. 293–319. *In* Treatise on Geochemistry.

Emery, and Thomson. 2004. Data Analysis Methods in Physical Oceanography, 2nd ed. Elsevier.

Falter, J. L., and F. J. Sansone. 2000a. Shallow pore water sampling in reef sediments. Coral Reefs **19**: 93–97.

Falter, J. L., and F. J. Sansone. 2000b. Hydraulic control of pore water geochemistry within the oxic-suboxic zone of a permeable sediment. Limnol. Oceanogr. **45**: 550–557.

Fletcher, C. H., E. E. Grossman, B. M. Richmond, and A. E. Gibbs. 2002. Atlas of Natural Hazards in the Hawaii Coastal Zone. I-2761. U.S. Geological Survey.

Fogaren, K. E. 2010. Short-time Scale and Seasonal Variability of Porewater Constituents in a Permeable Nearshore Sediment. University of Hawaii at Manoa.

Fogaren, K. E., F. J. Sansone, and E. H. De Carlo. 2013. Porewater temporal variability in a wave-impacted permeable nearshore sediment. Mar. Chem. **149**: 74–84. doi:10.1016/j.marchem.2012.12.005

Folk, R. R. L., and W. W. C. Ward. 1957. Brazos River Bar: A study in the significance of grain size parameters. SEPM J. Sediment. Res. **27**: 3–26. doi:10.1306/74D70646-2B21-11D7-

Fram, J. P., G. R. Pawlak, F. J. Sansone, B. T. Glazer, and A. K. Hannides. 2014. OCEANOGRAPHY : METHODS Miniature thermistor chain for determining surficial sediment porewater advection. 155–165. doi:10.4319/lom.2014.12.155

Froelich, P. N., G. P. Klinkhammer, M. L. Bender, N. A. Luedtke, G. R. Heath, D. Cullen, and P. Dauphin. 1979. Early oxidation of organic matter in pelagic sediments of the eastern equatorial Atlantic: suboxic diagenesis. Geochim. Cosmochim. Acta 43: 1075–1090.

Gordon, D. G. 1969. Examination of methods of particulate organic carbon analysis. Deep Sea Res. Oceanogr. Abstr. 16: 661–665. doi:10.1016/0011-7471(69)90066-7

Grasshoff, K., M. Ehrhardt, and K. Kremling. 1983. Methods of Seawater Analysis. Second, Revised and Extended Edition, 3rd ed. Wiley-VCH.

Grigg, R. W. 1995. Coral reefs in an urban embayment in Hawaii: a complex case history controlled by natural and anthropogenic stress. Coral Reefs 14: 253–266.

Gruber, N., and J. L. Sarmiento. 1997. Global patterns of marine nitrogen fixation and denitrification. Global Biogeochem. Cycles 11: 235–266. doi:10.1029/97GB00077

Hall, S. J. 2002. The continental shelf benthic ecosystem: current status, agents for change and future prospects. Environ. Conserv. 29: 350–374. doi:10.1017/S0376892902000243

Hannides, A. K. 2008. Organic matter cycling and nutrient dynamics in marine sediments. University of Hawaii at Manoa.

Hebert, A. B., F. J. Sansone, and G. R. Pawlak. 2007. Tracer dispersal in sandy sediment porewater under enhanced physical forcing. Cont. Shelf Res. 27: 2278–2287. doi:10.1016/j.csr.2007.05.016

Huettel, M., P. Berg, and J. E. Kostka. 2014. Benthic exchange and biogeochemical cycling in permeable sediments. Ann. Rev. Mar. Sci. 6: 23–51. doi:10.1146/annurev-marine-051413-012706

Huettel, M., and A. Rusch. 2000. Transport and degradation of phytoplankton in permeable sediment. Limnol. Oceanogr. 45: 534–549. doi:10.4319/lo.2000.45.3.0534

Huettel, M., W. Ziebis, S. Forester, and G. W. Luther III. 1998a. Advective transport affecting metal and nutrient distributions and interfacial fluxes in permeable sediments. Geochim. Cosmochim. Acta 62: 613–631.

Huettel, M., W. Ziebis, S. Forester, G. W. Luther III, S. Forster, G. W. Luther III, and G. W. Luther. 1998b. Advective transport affecting metal and nutrient distributions and interfacial fluxes in permeable sediments. Geochim. Cosmochim. Acta 62: 613–631. doi:10.1016/S0016-7037(97)00371-2

Huettel, M., W. Ziebis, and S. Forster. 1996. Flow-induced uptake of particulate matter in permeable sediments. Limnol. Oceanogr. **41**: 309–322.

Jahnke, R. A. A., J. Nelson, R. L. Marinelli, and J. E. Eckman. 2000. Benthic flux of biogenic elements on the Southeastern US continental shelf: influence of pore water advective transport and benthic microalgae. Cont. Shelf Res. **20**: 109–127.

Jahnke, R. A., M. Richards, J. Nelson, C. Robertson, A. Rao, and D. Jahnke. 2005. Organic matter remineralization and porewater exchange rates in permeable South Atlantic Bight continental shelf sediments. Cont. Shelf Res. **25**: 1433–1453. doi:10.1016/j.csr.2005.04.002

Janssen, F., M. Huettel, and U. Witte. 2005. Pore-water advection and solute fluxes in permeable marine sediments (II): Benthic respiration at three sandy sites with different permeabilities (German Bight, North Sea). Limnol. Oceanogr. **50**: 768–778. doi:10.4319/lo.2005.50.3.0768

Keil, R. G., and J. I. Hedges. 1993. Sorption of organic matter to mineral surfaces and the preservation of organic matter in coastal marine sediments. Chem. Geol. **107**: 385–388. doi:10.1016/0009-2541(93)90215-5

Kérouel, R., and A. Aminot. 1997. Fluorometric determination of ammonia in sea and estuarine waters by direct segmented flow analysis. Mar. Chem. **57**: 265–275.

Klute, A., and C. Dirksen. 1986. Methods of Soil Analysis: Part 1—Physical and Mineralogical Methods, Soil Science Society of America, American Society of Agronomy.

Laws, E. A., D. G. Redalje, L. W. Haas, P. K. Bienfang, R. W. Eppley, W. G. Harrison, D. M. Karl, and J. Marra. 1984. High phytoplankton growth and production rates in oligotrophic Hawaiian coastal waters. Limnol. Oceanogr. **29**: 1161–1169.

Lettmann, K. A., N. Riedinger, R. Ramlau, N. Knab, M. E. Böttcher, A. Khalili, J. O. Wolff, and B. B. Jørgensen. 2012. Estimation of biogeochemical rates from concentration profiles: A novel inverse method. Estuar. Coast. Shelf Sci. **100**: 26–37. doi:10.1016/j.ecss.2011.01.012

Li, Y.-H., and S. Gregory. 1974. Diffusion of ions in sea water and in deep-sea sediments. Geochim. Cosmochim. Acta **38**: 703–714. doi:10.1016/0016-7037(74)90145-8

Libes, S. 2009. Introduction to Marine Biogeochemistry, 2nd Editio. Academic Press.

Lu, X., T. Ren, and Y. Gong. 2009. Experimental investigation of thermal dispersion in saturated soils with one-dimensional water flow. Soil Sci. Soc. Am. J. **73**: 1912–1920. doi:10.2136/sssaj2008.0251

Manheim, F. T. 1970. The diffusion of ions in unconsolidated sediments. Earth Planet. Sci. Lett. **9**: 307–309. doi:10.1016/0012-821X(70)90123-8

Marinelli, R. L., R. A. A. Jahnke, D. B. Craven, J. Nelson, and J. E. Eckman. 1998. Sediment nutrient dynamics on the South Atlantic Bight continental shelf. Limnol. Oceanogr. **43**:

1305–1320.

de Marsily, G. 1986. Quantitative hydrogeology: groundwater hydrology for engineers, Academic Press.

McDuff, R. E., and R. A. Ellis. 1979. Determining diffusion coefficients in marine sediments; a laboratory study of the validity of resistivity techniques. Am. J. Sci. **279**: 666–675. doi:10.2475/ajs.279.6.666

McManus, J. 1988. Grain size determination and interpretation, p. 63–85. *In* M. Tucker [ed.], Techniques in Sedimentology. Oxford (Blackwell).

Meyer-Reil, L. A. 1986. Spatial and temporal distribution of bacterial populations in marine shallow water surface sediments , p. 141–160. *In* P. Lasserre and J.M. Martin [eds.], Biogeochemical processes at the land-sea boundry. Elsevier/North-Holland Publishing Co.

Moberly, R. J., and T. Chamberlain. 1964. Hawaiian beach systems. Hawaii Inst. Geophys. Rep. HIG **64**.

Moore, W. S., J. Krest, G. Taylor, E. Roggenstein, S. Joye, and R. Lee. 2002. Thermal evidence of water exchange through a coastal aquifer: Implications for nutrient fluxes. Geophys. Res. Lett. **29**: 44–49. doi:10.1029/2002GL014923

Nielsen, van Genuchten, B. 1986. Water Flow ans Solute Transport Processes in the ZNS. Water Resour. Res. **22**: 89S–108S.

Parnell, K. E. 2011. Internal Circulation, p. 1205. *In* D. Hopley [ed.], Encyclopedia of modern coral reefs: structure, form and process. Springer.

Pawlak, G., E. H. De Carlo, J. P. Fram, and others. 2009. Development, deployment, and operation of Kilo Nalu nearshore cabled observatory. Ocean. 2009-Europe 1–10. doi:10.1109/OCEANSE.2009.5278149

Precht, E., and M. Huettel. 2004. Rapid wave-driven advective pore water exchange in a permeable coastal sediment. J. Sea Res. **51**: 93–107. doi:DOI 10.1016/j.seares.2003.07.003

Qian, Q., V. R. Voller, and H. G. Stefan. 2008. A vertical dispersion model for solute exchange induced by underflow and periodic hyporheic flow in a stream gravel bed. Water Resour. Res. **44**: 1–17. doi:10.1029/2007WR006366

Rao, A. M. F., M. J. McCarthy, W. S. Gardner, and R. a. Jahnke. 2007. Respiration and denitrification in permeable continental shelf deposits on the South Atlantic Bight: Rates of carbon and nitrogen cycling from sediment column experiments. Cont. Shelf Res. **27**: 1801–1819. doi:10.1016/j.csr.2007.03.001

Rau, G. C., M. S. Andersen, and R. I. Acworth. 2012. Experimental investigation of the thermal dispersivity term and its significance in the heat transport equation for flow in sediments. Water Resour. Res. **48**: 1–21. doi:10.1029/2011WR011038

Redfield, A., B. Ketchum, and F. Richards. 1963. The influence of organisms on the composition of seawater, p. 26–77. *In* M. Hill [ed.], The Sea. Interscience.

Reimers, C. E., H. a. Stecher, G. L. Taghon, and others. 2004. In situ measurements of advective solute transport in permeable shelf sands. Cont. Shelf Res. **24**: 183–201. doi:10.1016/j.csr.2003.10.005

Riedl, R. J., N. Huang, and R. Maohan. 1972. The subtidal pump: a mechanism of interstitial water exchange by wave action. Mar. Biol. **13**: 210–221.

Ringuet, S., L. Sassano, and Z. I. Johnson. 2011. A suite of microplate reader-based colorimetric methods to quantify ammonium, nitrate, orthophosphate and silicate concentrations for aquatic nutrient monitoring. J. Environ. Monit. **13**: 370–6. doi:10.1039/c0em00290a

Rocha, C. 2008. Sandy sediments as active biogeochemical reactors: compound cycling in the fast lane. Aquat. Microb. Ecol. **53**: 119–127.

Rusch, A., M. Huettel, C. Wild, and C. E. Reimers. 2006. Benthic oxygen consumption and organic matter turnover in organic-poor, permeable shelf sands. Aquat. Geochemistry **12**: 1–19. doi:10.1007/s10498-005-0784-x

Ruttenberg, K. C., and R. A. Berner. 1993. Authigenic apatite formation and burial in sediments from non-upwelling, continental margin environments. Geochim. Cosmochim. Acta **57**: 991–1007.

Ruttenberg, K. C., G. M. Filippelli, K. C. Ruttenberg, G. M. Filippelli, and K. C. Ruttenberg. 2014. The Global Phosphorus Cycle, p. 499–588. *In* H. H.D. and K.K. Turekian [eds.], Treatise on Geochemistry. Elsevier Ltd.

Sansone, F., and J. Chanton. 1993. Methane cycling in coral reef frameworks. Trends Microb. Ecol. **6**: 157–162.

Sansone, F. J., G. Pawlak, T. P. Stanton, and others. 2008. Kilo Nalu physical/biogeochemical dynamics above and within permeable sediments. Oceanography **21**: 173–178.

Sansone, F. J., H. L. Spalding, and C. M. Smith. 2017. Sediment Biogeochemistry of Mesophotic Meadows of Calcifying Macroalgae. Aquat. Geochemistry **23**: 141–164. doi:10.1007/s10498-017-9315-9

Santos, I. R., B. D. Eyre, and R. N. Glud. 2012a. Influence of porewater advection on denitrification in carbonate sands: Evidence from repacked sediment column experiments. Geochim. Cosmochim. Acta **96**: 247–258. doi:10.1016/j.gca.2012.08.018

Santos, I. R., B. D. Eyre, and M. Huettel. 2012b. The driving forces of porewater and groundwater flow in permeable coastal sediments: A review. Estuar. Coast. Shelf Sci. **98**: 1–15. doi:10.1016/j.ecss.2011.10.024

Savidge, W. B., A. Wilson, and G. Woodward. 2016. Using a Thermal Proxy to Examine Sediment–Water Exchange in Mid-Continental Shelf Sandy Sediments. Aquat. Geochemistry **22**: 419–441. doi:10.1007/s10498-016-9295-1

Tribble, G. W., F. J. Sansone, and S. V Smith. 1990. Stoichiometric modeling of carbon diagenesis within a coral reef framework. Geochim. Cosmochim. Acta **54**: 2439–2449.

Webb, J. E., and J. Theodor. 1968. Irrigation of submerged marine sands through wave action. Nature **220**: 682–683.

Wilson, A. M., G. L. Woodward, and W. B. Savidge. 2016. Using heat as a tracer to estimate the depth of rapid porewater advection below the sediment-water interface. J. Hydrol. **538**: 743–753. doi:10.1016/j.jhydrol.2016.04.047

Wright, J., A. Colling, D. Park, and Open University. Oceanography Course Team. 1999. Waves, tides, and shallow-water processes, Butterworth-Heinemann, in association with the Open University.

Ziebis, W., M. Huettel, and S. Forster. 1996. Impact of biogenic sediment topography on oxygen fluxes in permeable seabeds. Mar. Ecol. Prog. Ser. **140**: 227–237. doi:10.3354/meps140227

Table 4.1 Summary of water-column and sediment characteristics for study sites.

	PARAMETER	SITE LOCATION	
		Fine Site	Medium Site
	Location	Makai Research Pier	Kilo Nalu Observatory
	Latitude	21°19'9.16" N	21°17'18.96" N
	Longitude	157°40'8.23" W	157°51'53.90" W
	Water column depth (m)	3.1	12
	Distance from shore (m)	115	385
Sediment	Sand size (Wentworth)	very fine - fine	fine - medium
	Mean grain size (μm)	187 ± 0.03*	223 ± 0.02
	Fines (< 63 μm; wt. %)	10%	< 1%
	Sorting	poorly sorted	well sorted
	Permeability (m^2)	$2.3 \pm 1.6 \times 10^{-12}$*	$4.7 \pm 1.1 \times 10^{-11}$**
	Porosity	0.59 ± 0.01*	0.49***
	CaCO$_3$ content (wt. %)	90.6 ± 0.4	93.7 ± 0.004
	OC content (wt. % C)	0.55 ± 0.20	0.36 ± 0.20
	TN content (wt. % N)	0.05 ± 0.01	0.07 ± 0.01

*A.K. Hannides, personal communication
**Hannides 2008
***Hebert et al. 2007

Table 4.2: Inorganic nutrient and DIC fluxes at the SWI (J_{SWI}) and depth-integrated reactions (*DIR*) for solutes the Fine and Medium Sites. Values of *DIR* are calculated according to Equation 4.4 from the SWI to the deepest porewater sampling depth at each site (see text). Negative fluxes are upward and positive fluxes are downward. Positive values of *DIR* indicate net production and negative values indicate net consumption.

Site	Solute	J_{SWI} (mmol m^{-2}d^{-1})	*DIR* (mmol m^{-2}d^{-1})
Fine	SRP	-0.36 ± 0.33	0.45 ± 0.28
	Si	-9.1 ± 3.5	9.0 ± 3.2
Medium	DIC	-11.5 ± 9.5	11.7 ± 9.9
	SRP	-0.21 ± 0.15	0.21 ± 0.15
	Si	-0.78 ± 1.0	0.79 ± 1.0
	NH$_4^+$	-0.35 ± 0.38	0.35 ± 0.38
	NO$_x$	0.01 ± 0.05	-0.01 ± 0.05

Table 4.3 Comparison of DIC and nutrient fluxes across the SWI. Negative fluxes are upward. Sediment type is denoted as carbonate (C) or silicate (S), and grainsize as fine (F), medium (M), or coarse (C). NLE = non-local exchange parameter (see text).

| LOCATION	SEDIMENT		J_{SWI} (mmol m^{-2} d^{-1}), mean ± SD					METHOD OF MEASUREMENT			NOTES	REF.
	Type	Grain size	DIC	SRP	Si	NH$_4^+$	NO$_x$	Fluxes	Reaction Rates	Porewater Transport		
South Atlantic Bight (SAB)	S	F-M	-	-	−0.95 ± 1.82	−0.16 ± 0.44	-	stirred benthic chambers	non-stirred whole core incubations	inverse NLE porewater model	light and dark chambers	Marinelli et al. 1998
			−5.28 ± 0.06	-	−0.10 ± 0.06	−0.48 ± 0.36	-	steady-state diagenetic model	stirred whole core incubations	inverse D$_E$ and NLE PW models	winter < 23°C	Jahnke et al. 2005
			−17.7 ± 0.35	-	−0.62 ± 0.37	−2.45 ± 0.90	-				summer > 23 °C	
German Bight (GB)	S	F	-	−0.07 ± 0.16	−2.54 ± 1.67	−1.89 ± 1.49	−0.35 ± 0.60	stirred benthic chambers	-	-	-	Janseen et al. 2005
		M	-	−0.02 ± 0.05	−1.57 ± 2.25	−0.41 ± 1.10	−0.57 ± 0.76					
		C	-	−0.03 ± 0.09	−1.22 ± 1.44	−0.07 ± 1.30	−1.04 ± 0.94					
Bahamas (LSI)	C	F-C	−1.2 ± 0.85	-	-	-	-	steady-state diagenetic model	inverse porewater model	stoichiometrically constrained NLE model	seagrass-free sand site	Burdige et al. 2008
Hawaii	C	F	-	−0.36 ± 0.33	−9.05 ± 3.45	-	-	steady-state diagenetic model	inverse porewater model	field-constrained D$_E$ model	-	This study
		M	−11.5 ± 9.5	−0.21 ± 0.15	−0.78 ± 1.0	−0.35 ± 0.38	0.01 ± 0.06					
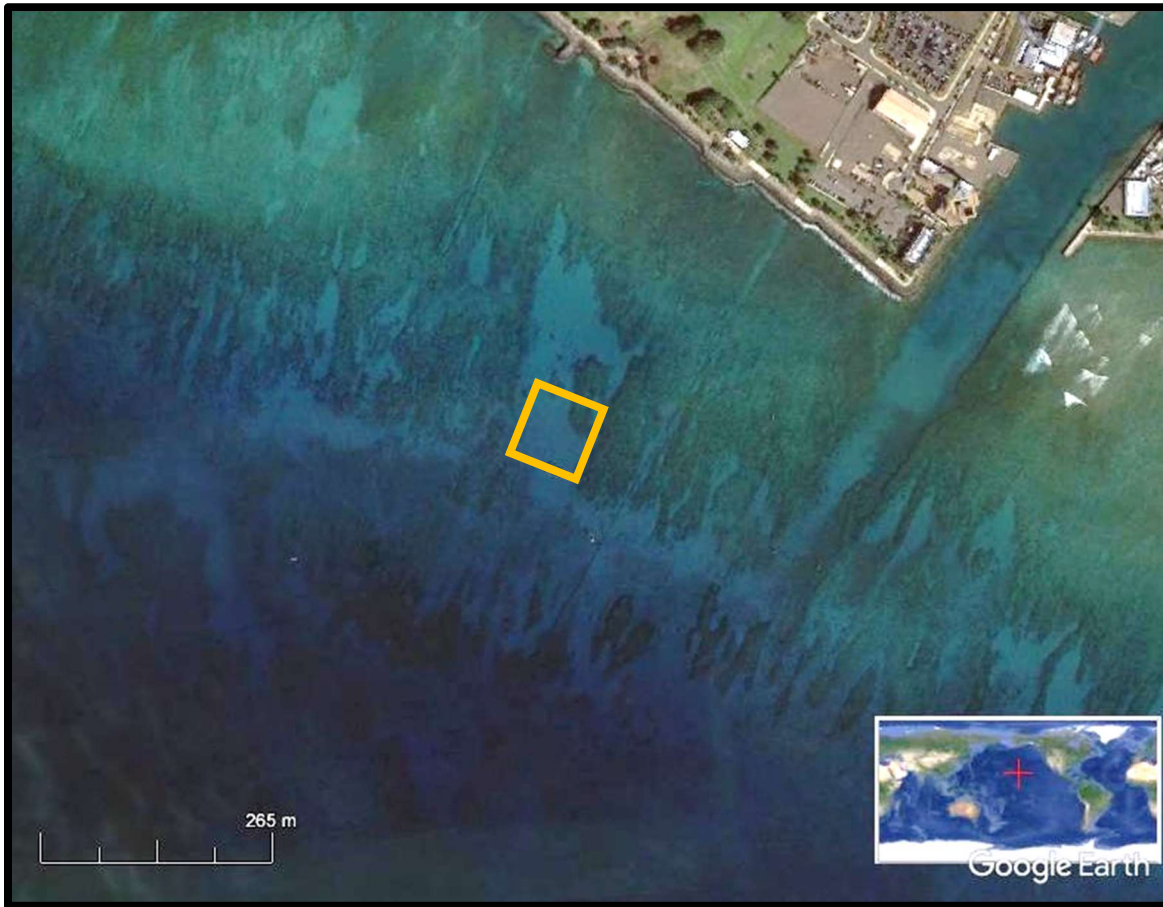
Figure 4.1: Satellite image of the Medium Site, located at Kilo Nalu Nearshore Observatory in Mamala Bay on the south shore of Oahu, Hawaii (Google Earth). The yellow rectangle indicates the study area.

Figure 4.2: Google Earth satellite image of the Fine Site, located at Makai Research Pier on the eastern shore of Oahu, Hawaii. The yellow rectangle indicates the study area.
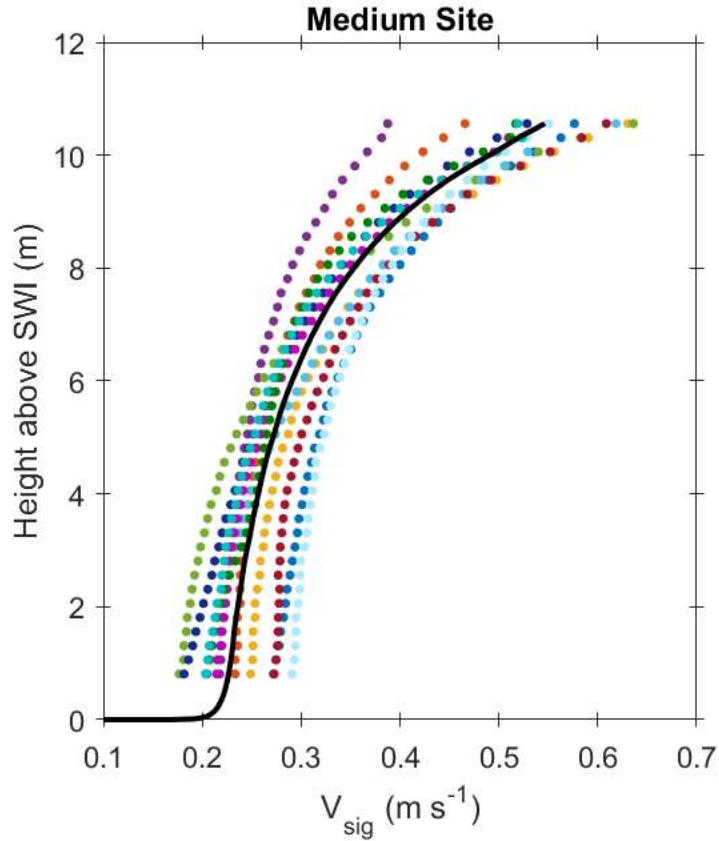
Figure 4.3: Vertical profiles of V_{sig} calculated for ten randomly selected dates over the 80-day experiment at the Medium Site. Colored lines are individual profiles of mean V_{sig} calculated for the three-hour interval, with a vertical resolution of 0.25 m for the measurements spanning $0.81 -$ 10.56 m above the SWI. The black line is the mean V_{sig} (n = 10), extrapolated to the SWI using Equation 4.1 (see text).
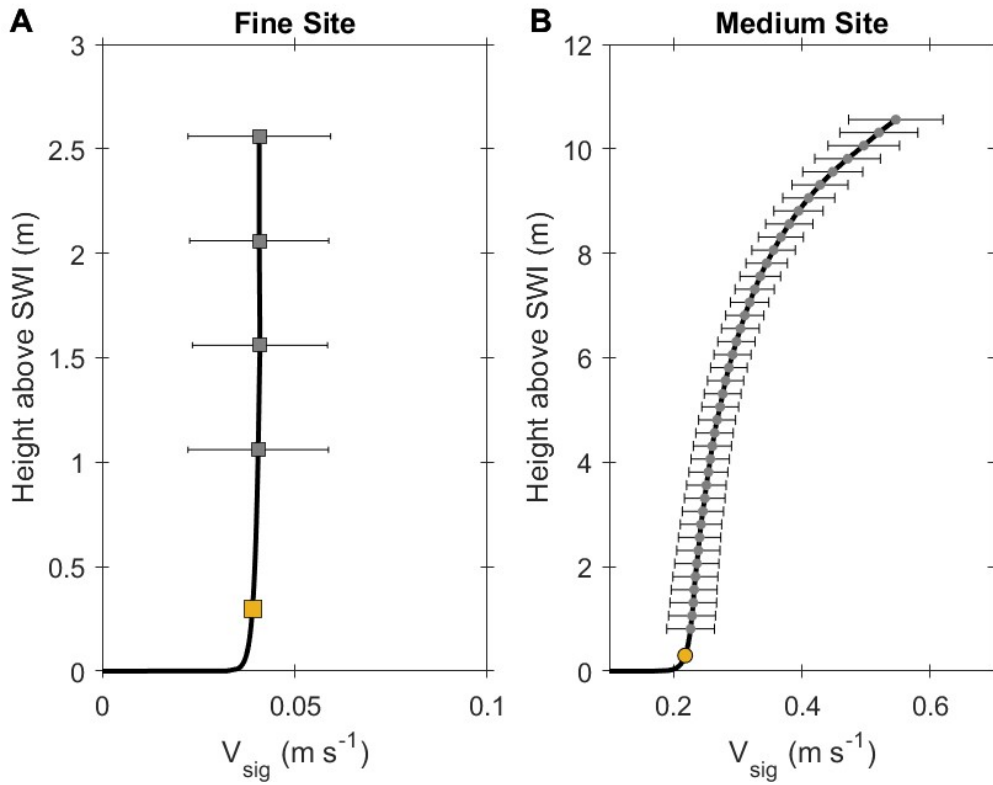
Figure 4.4: Black lines are mean V_{sig} values measured at (A) the Fine Site over 21-day deployment, and (B) the Medium Site using 10-randomly chosen profiles over the 80-day deployment (presented in Figure 4.3). Grey symbols are mean V_{sig} values from ADCP measurements, with error bars equal to 1 standard deviation. Values of V_{bed} (yellow symbols) are calculated for 0.3 m above the SWI using Equation 4.1 (see text). Note differences in axis scales.
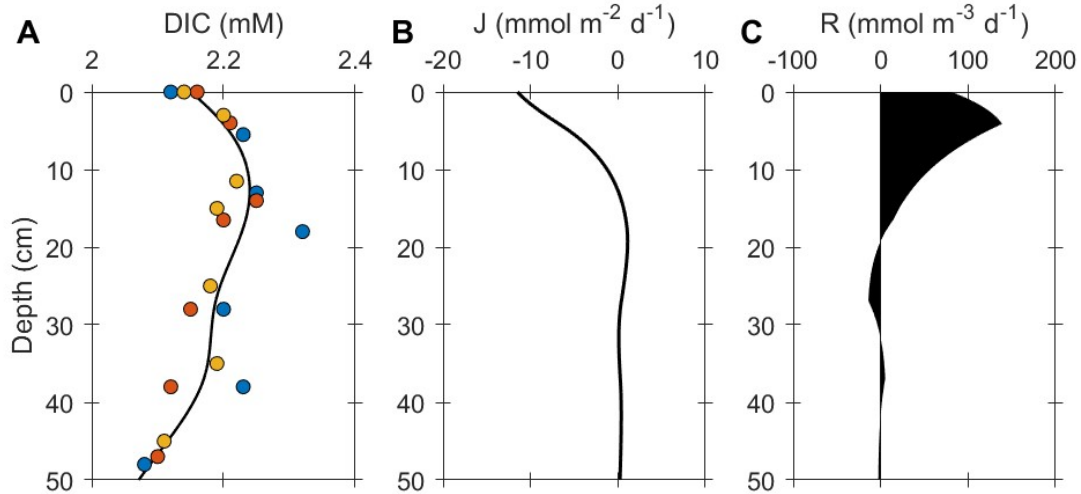
Figure 4.5: (A) Steady-state porewater profile for DIC at the Medium Site constructed from discrete porewater samples collected on 28 March 2011 (blue), 6 April 2011 (red), and 15 April 2011 (yellow). A smoothing-spline function was used to fit the data (black line). (B) Vertical profile of fluxes calculated using Fick's First Law, with a vertical resolution of 0.1 cm (see text). Negative fluxes move solutes upwards towards the water column and positive fluxes transport solutes downward into the sediment. (C) Vertical profile of the reaction rates (R) necessary to balance the divergence or convergence of the flux in Panel B (see text). Positive R values indicate net production of DIC, and negative R values indicate a net consumption of DIC.
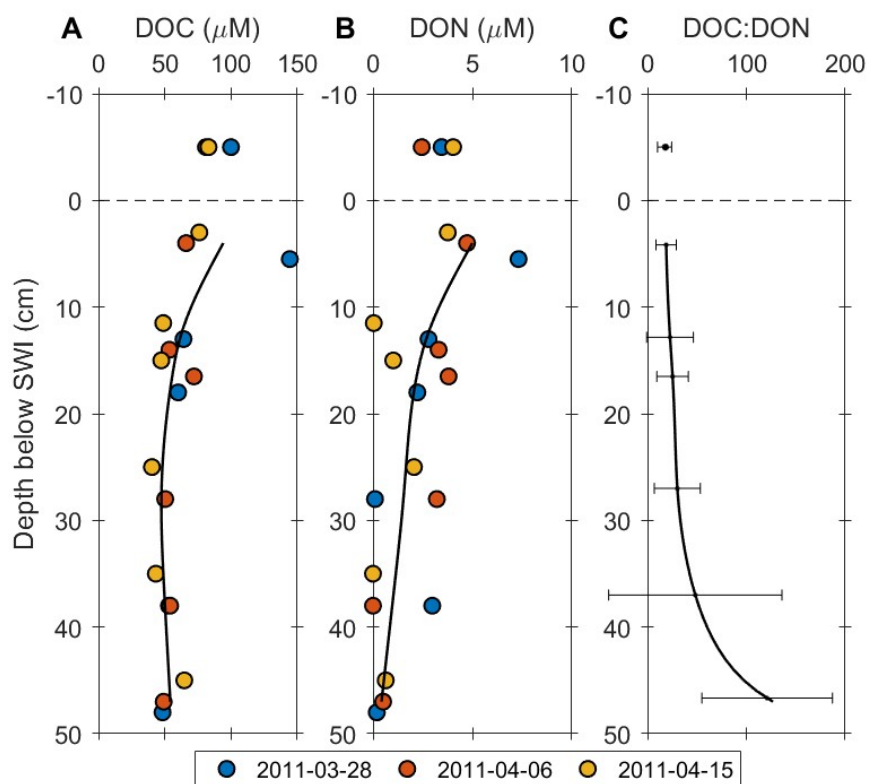
Figure 4.6: (A and B) DOC and DON profiles for all porewater sampling dates (n = 3) at the Medium Site; the black lines are the smoothing-spline function fit to mean porewater concentrations of DOC or DON at each depth. (C) The black line is the DOC:DON molar ratio (±1 standard deviation at discrete porewater sample depths), calculated as the ratio of the DOC:DON concentrations. The dashed horizontal line represents the SWI in all panels.
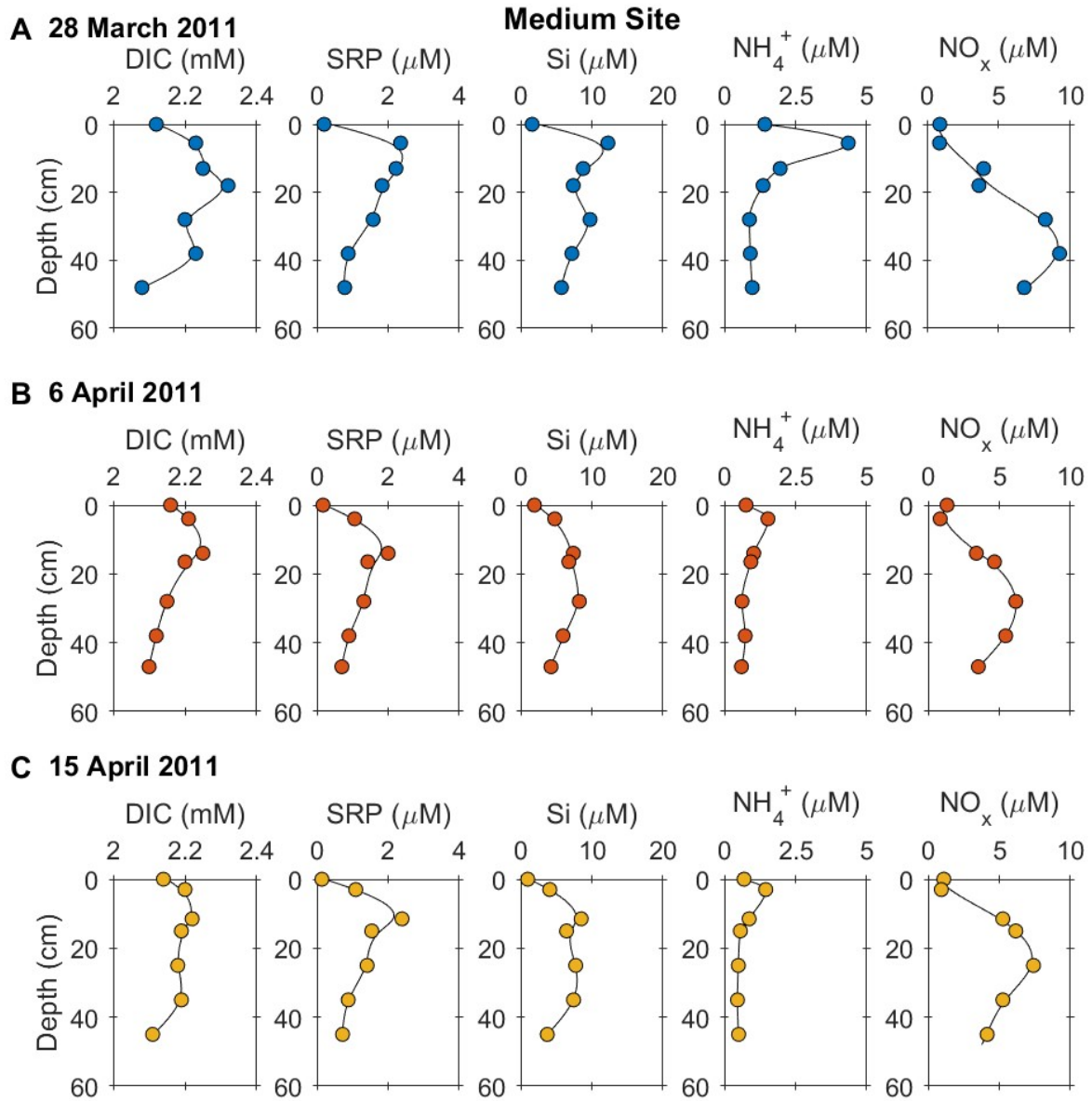
Figure 4.7: Porewater profiles of DIC, SRP, Si, NH_4^+ and NO_x at the Medium Site for (A) 28 March 2011, (B) 6 April 2011, and (C) 15 April 2011. For this and all subsequent porewater figures, values plotted at zero depth represent bottom-water samples collected ~5 cm above the SWI.
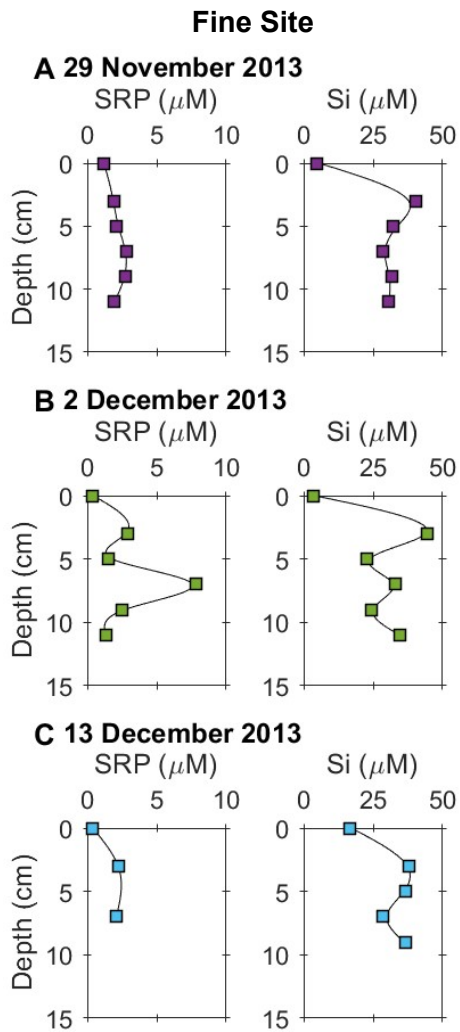
Figure 4.8: Porewater profiles of SRP and Si at the Fine Site on (A) 26 November 2013,
(B) 2 December 2013, and (C) 13 December 2013
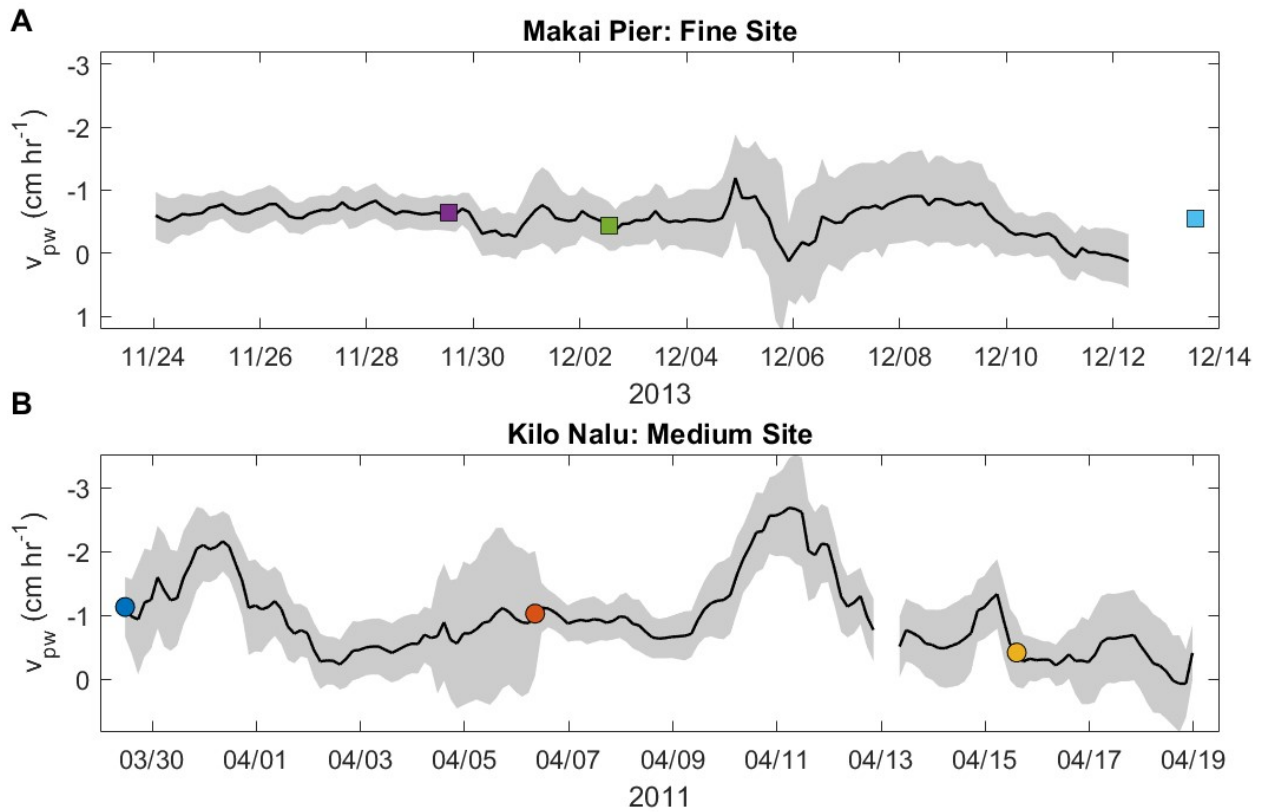
Figure 4.9: (A) v_{pw} measurements calculated for 9 cm below the SWI using the miniTchain at the Fine Site. Squares indicate porewater sampling dates. The mean v_{pw} value of -0.54 cm hr^{-1} for the entire record is used for the 13 December 2013 sampling date (cyan square; see text). (B) First 21 days of v_{pw} measurements calculated for 15 cm below the SWI from the 80-day miniTchain deployment at the Medium Site; the record is truncated to show details pertaining to the porewater sampling dates, indicated with circles.
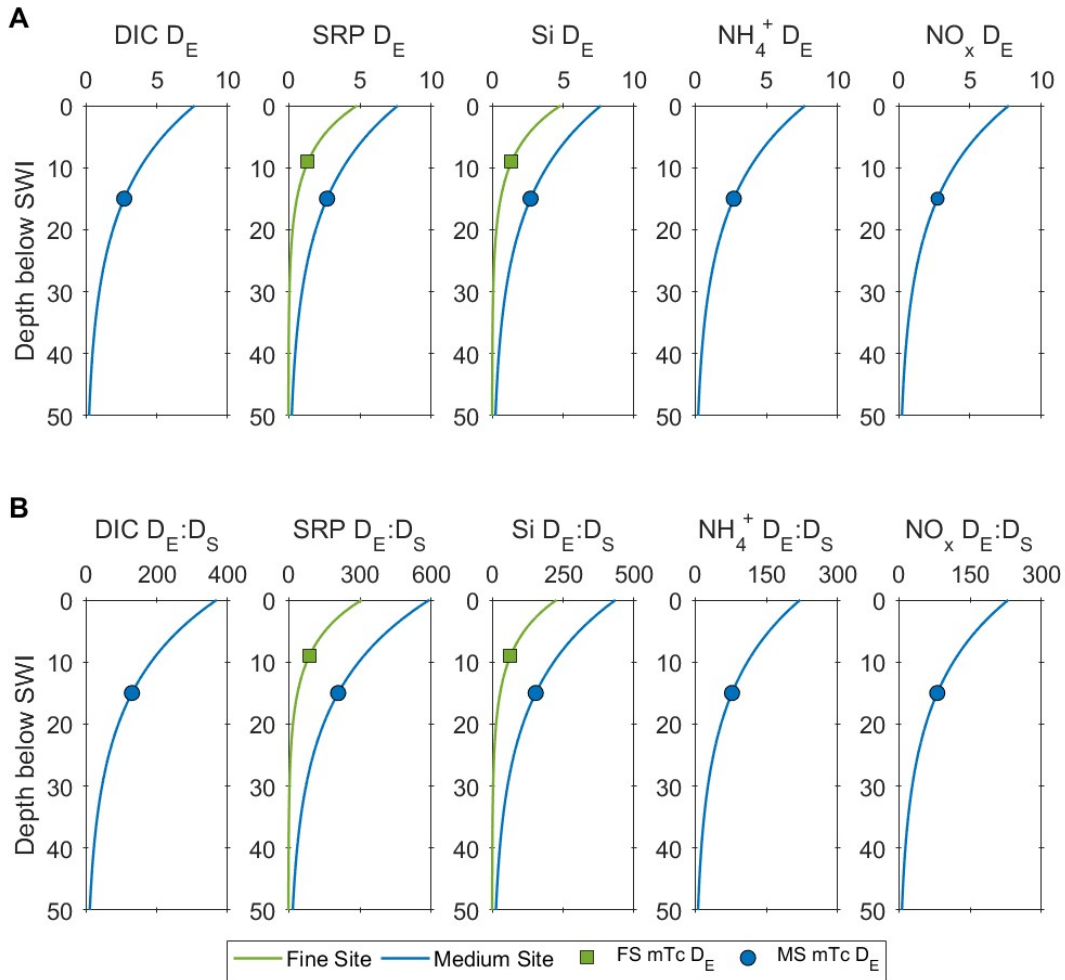
Figure 4.10: (A) Profiles of D_E for DIC, SRP, Si, NH_4^+ and NO_x at the Medium Site, and SRP and Si at the Fine Site. (B) Profiles of the $D_E : D_S$ ratios for each solute at the Fine Site and at the Medium Site. The green square (Fine Site) and the blue circle (Medium Site) are the mean $D_{E\,mTc}$ coefficients determined *in-situ* from the miniTchain (see text).

Medium Site

A. DIC (mM), J (mmol m^{-2} d^{-1}), R (mmol m^{-3} d^{-1})

B. SRP (μM), J (mmol m^{-2} d^{-1}), R (mmol m^{-3} d^{-1})

C. Si (μM), J (mmol m^{-2} d^{-1}), R (mmol m^{-3} d^{-1})

165
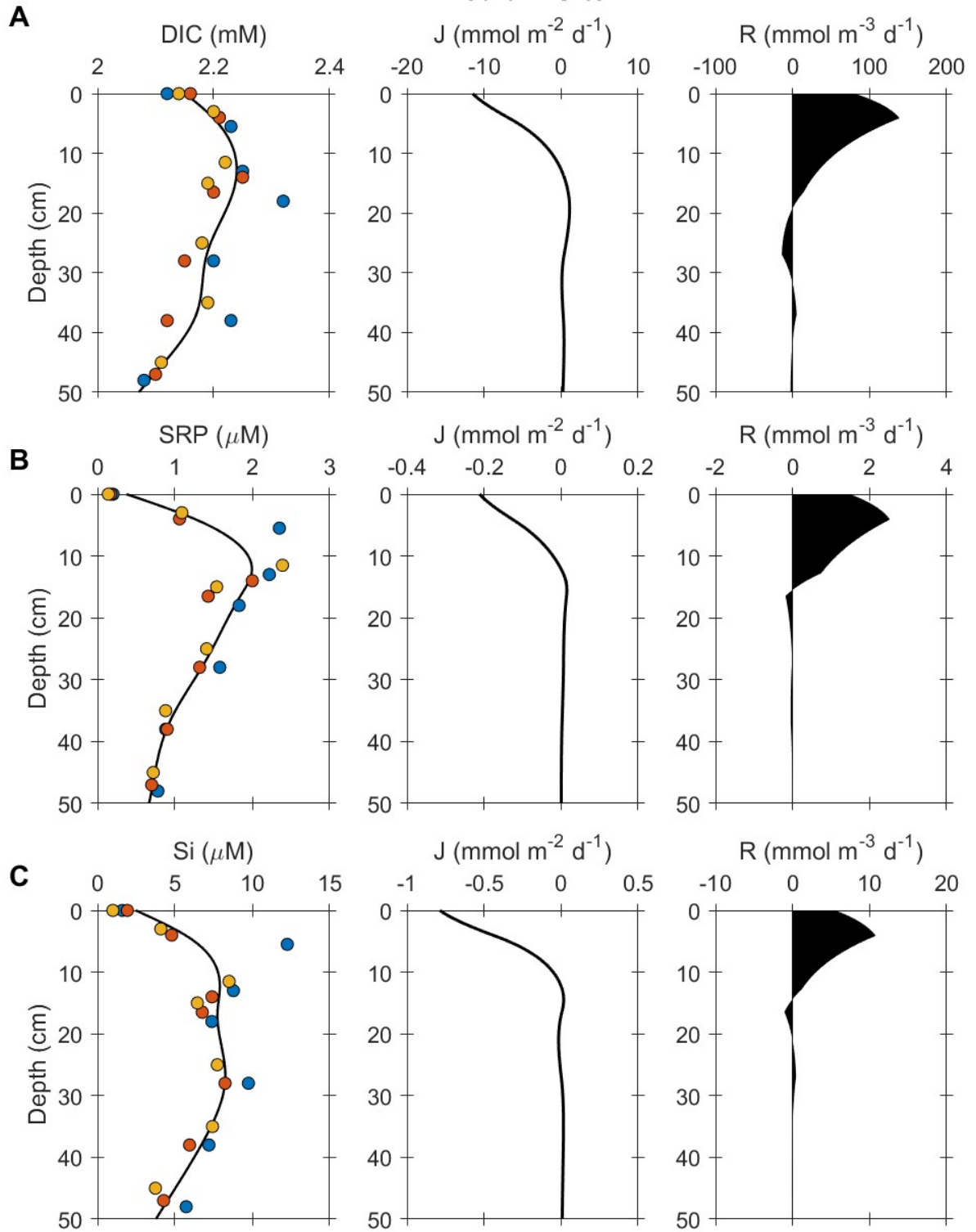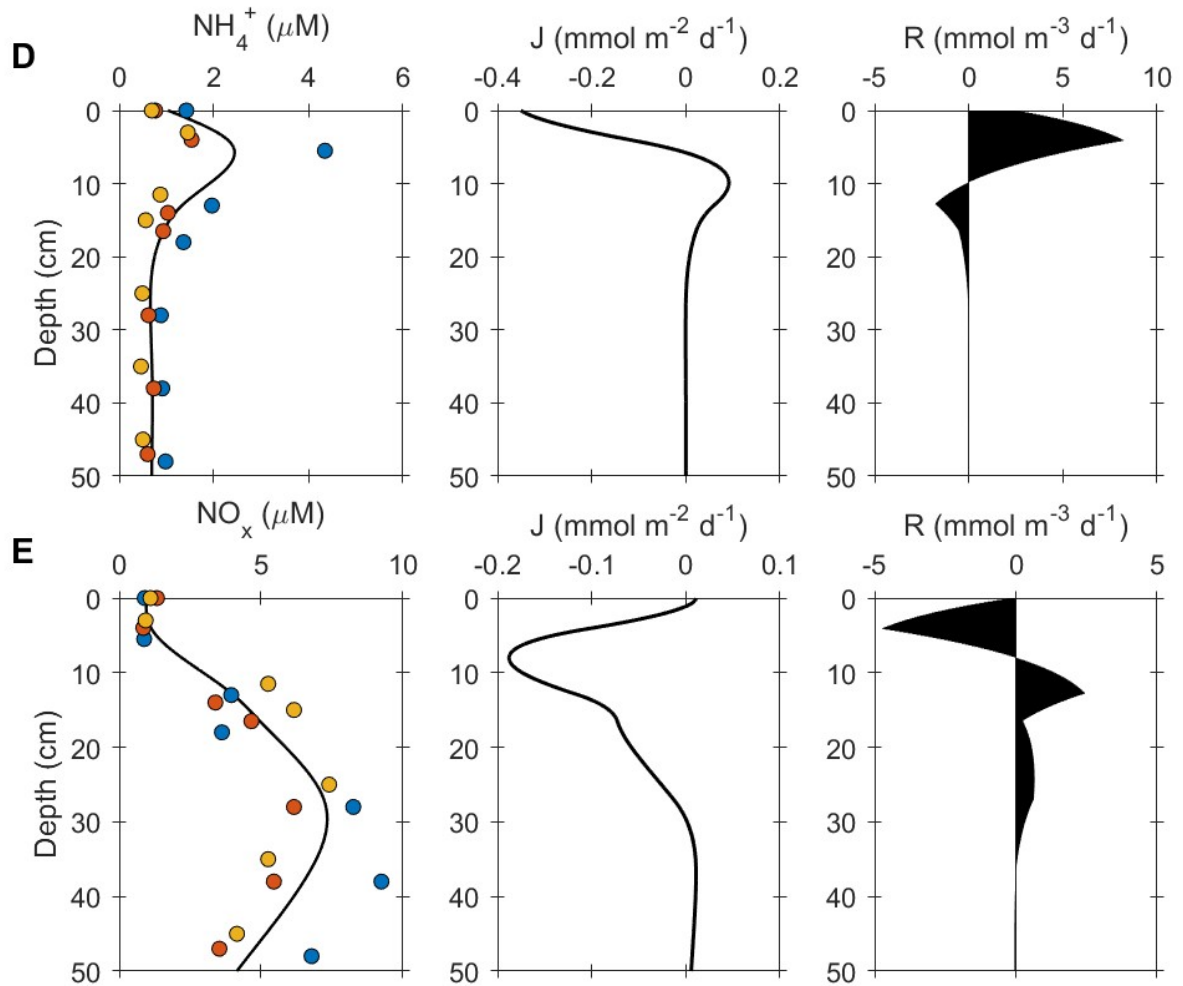
Figure 4.11: Steady-state porewater, flux (J), and reaction rate (R) profiles at the Medium Site for (A) DIC, (B) SRP, (C) Si, (D) NH_4^+ and (E) NO_x. Colored circles indicate porewater sample dates of 28 March 2011 (blue), 6 April 2011 (red), or 15 April 2011 (yellow). Negative fluxes move solutes upwards towards the water column, and positive fluxes transport solutes downwards into the sediment. Positive R values indicate net production of the solute, and negative R values indicate a net consumption of the solute.

Figure 4.12: Steady-state porewater, flux (J), and reaction rate (*R*) profiles at the Fine Site for (A) SRP and (B) Si. Colored squares indicate porewater samples collected on 29 November 2013 (purple), 2 December 2013 (green), and 13 December 2013 (cyan). Negative fluxes move solutes upwards towards the water column, and positive fluxes transport solutes downwards into the sediment. Positive R values indicate net production of the solute, and negative R values indicate a net consumption of the solute.

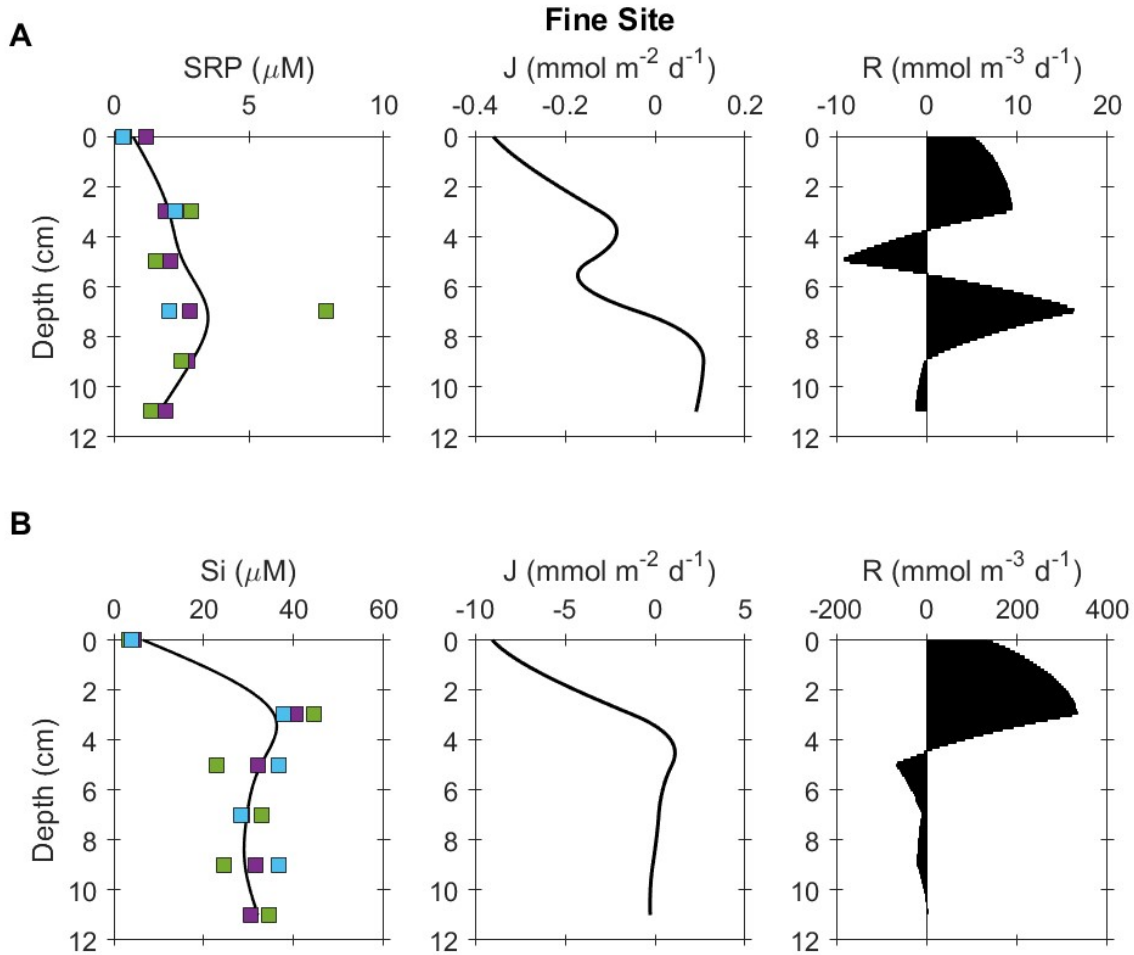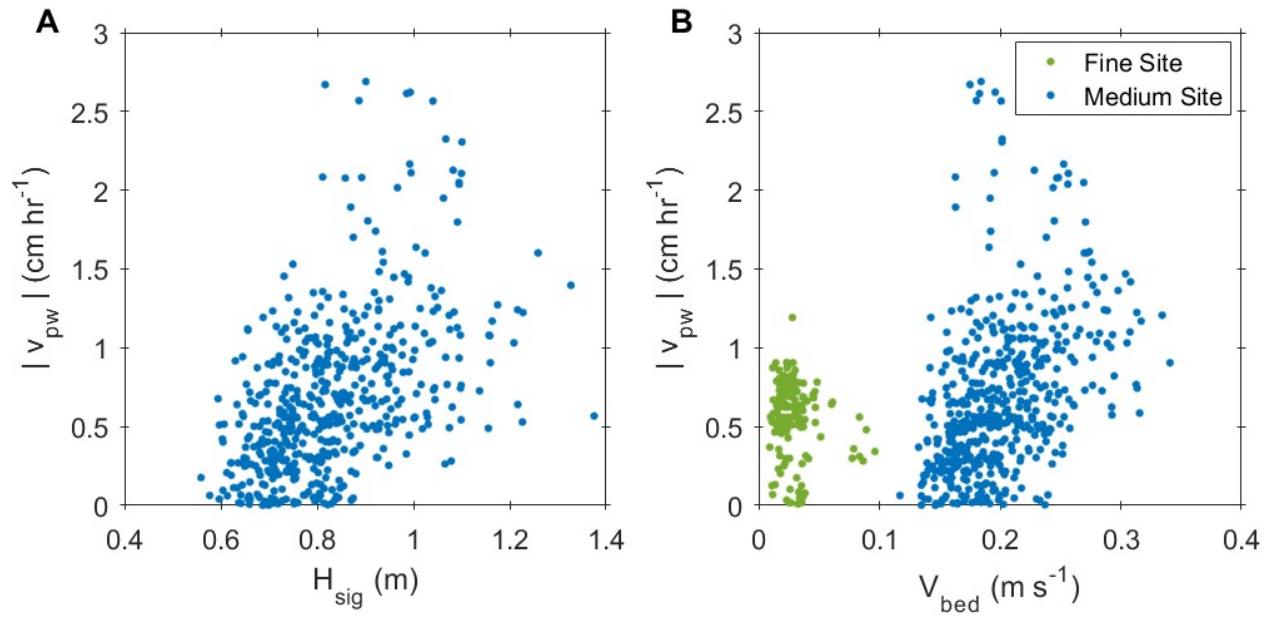**Figure 4.13:** (A) v_{pw} versus H_{sig} at the Medium Site ($R^2 = 0.24$). (B) v_{pw} versus V_{bed} at the Fine Site ($R^2 = 0.02$) and Medium Site ($R^2 = 0.18$). Each dot represents a three-hour mean of *in-situ* porewater or hydrodynamic measurements.
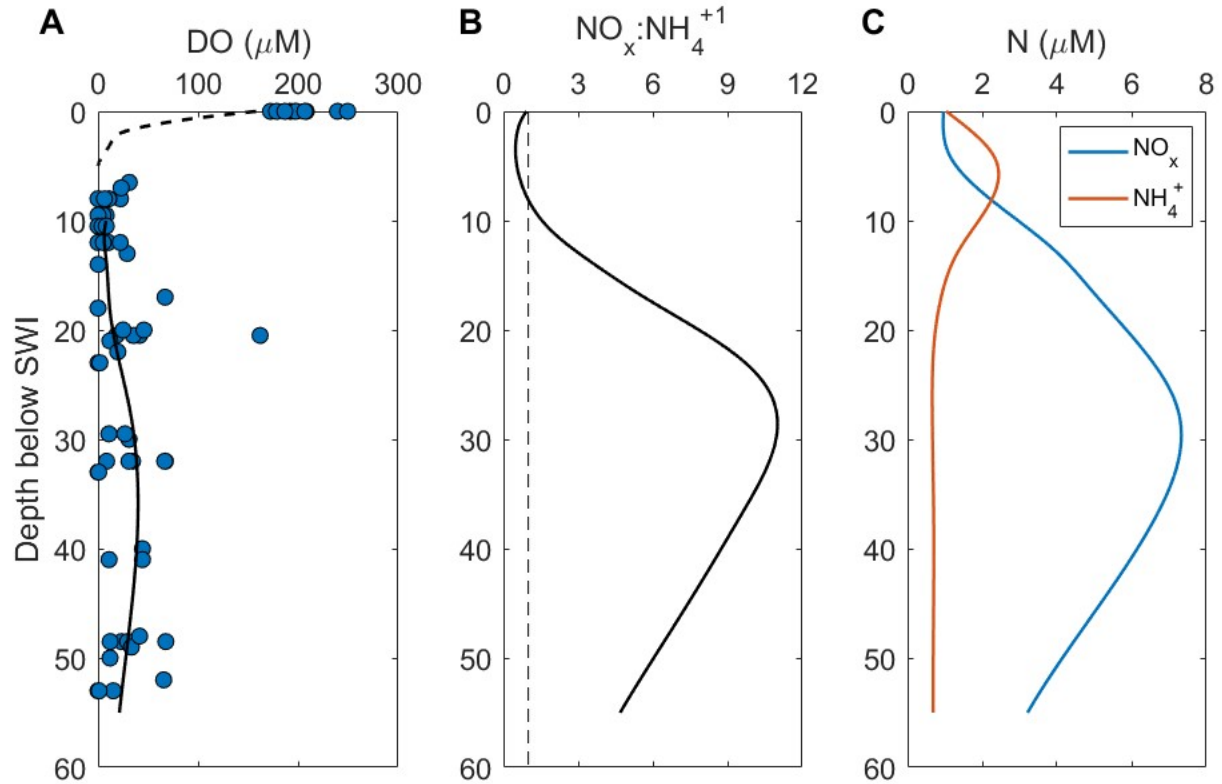
Figure 4.14: (A) DO samples (blue circles) previously collected at the Medium Site from July to December 2008 during background conditions (Fogaren et al. 2013). Samples collected at ~5 cm above the SWI are plotted at a depth of 0 cm. The black line represents the mean DO profile calculated using a smoothing-spline function for mean DO concentrations at each porewater sampling depth. The dashed line indicates the mean DO profile from high-resolution voltammetry profiles (n = 3) on 19 April 2011. (B) The black line is the ratio of $NO_x:NH_4^+$ steady-state profiles shown in Panel C; the vertical dashed line indicates a $NO_x:NH_4^+$ ratio of 1. (C) Steady-state profiles of NO_x and NH_4^+ calculated using a smoothing-spline function for mean concentrations from the three porewater sampling dates in 2013 (data presented in Figure 4.11).
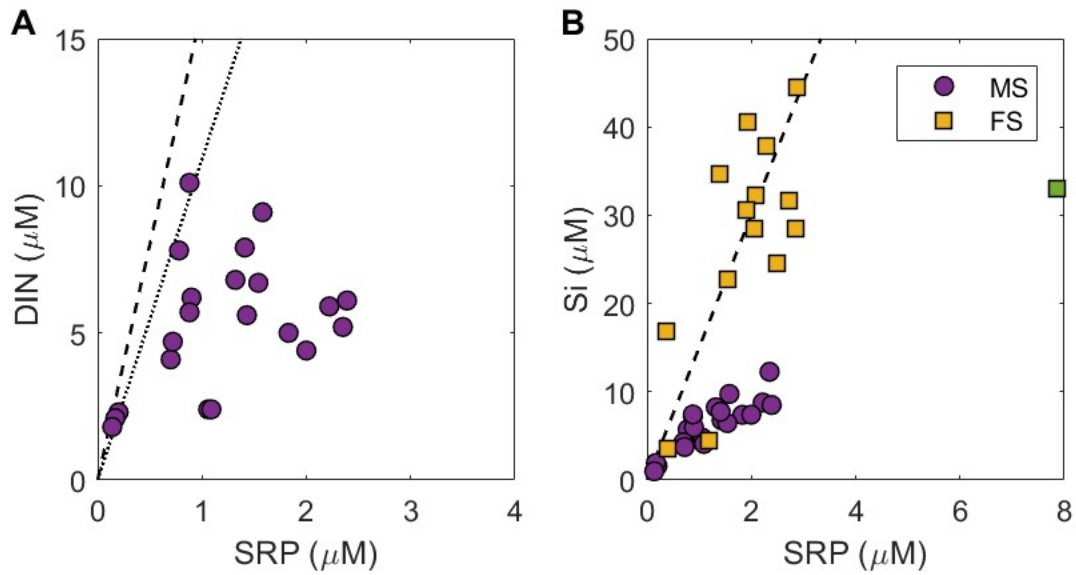
Figure 4.15: Nutrient-nutrient plots for porewater and overlying bottom water for (A) DIN and SRP at the Medium Site (MS; $R^2 = 0.14$) and (B) Si and SRP at the Medium Site ($R^2 = 0.74$) and the Fine Site (FS; $R^2 = 0.51$). Dashed lines indicate Redfield ratios for N:P (16:1) and Si:P (15:1), and the dotted line indicates a Laws ratio for N:P (10.9:1, see text). Note the outlying green square was not included in the Si-SRP correlation for the Fine Site.
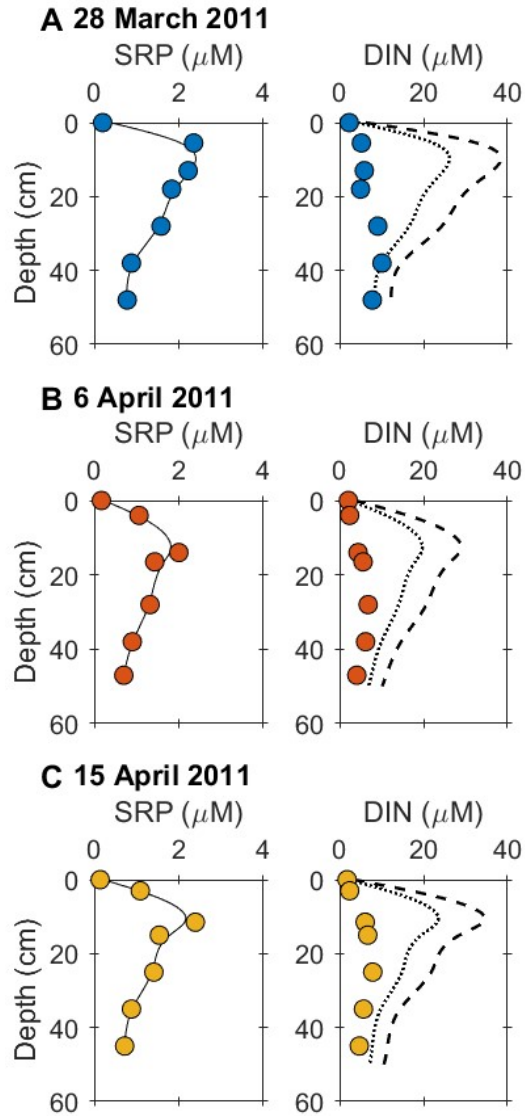
Figure 4.16: Stoichiometrically predicted DIN profiles calculated from SRP profiles using an initial organic matter N:P molar ratio of 10.9 (Laws; dotted profile) or a N:P molar ratio of 16 (Redfield; dashed profile) for the Medium Site on (A) 28 March 2011, (B) 6 April 2011, and (C) 15 April 2011. Circles represent measured porewater concentrations of SRP or DIN (NH_4^+ + NO_x).

Chapter 5: Conclusions

5.1   Summary of Results

This dissertation used a combination of discrete porewater sampling techniques, field-based porewater transport measurements, and steady-state diagenetic models to investigate the processes controlling the spatial distribution, remineralization rates, and flux of dissolved nutrients and carbon in permeable sediments. Advective flows appear to affect nutrient and carbon distributions to various degrees in the permeable sediments at the Fine, Medium and Coarse Sites, and depend largely on the sediment characteristics and hydrodynamic conditions at each site.

The fine-scale variability of dissolved nutrients in rippled permeable sediments was investigated using two field-based approaches to determine if the distinct spatial distribution of dissolved nutrients observed in laboratory flume studies (e.g., Precht et al. 2004; Huettel et al. 2014) could be observed *in-situ* in a fine or coarse sand. Dissolved nutrients varied laterally at both the Fine and Coarse Sites, but due to different nutrient-regulating processes. A greater degree of fine-scale nutrient variability was observed in porewater at the Coarse Site than at the Fine Site. Advective porewater flows appear to be the process primarily responsible for the dissolved nutrient structure at the Coarse Site, as nutrient variability was systematically related to topographic position along the sand ripple field. This distinct fine-scale spatial variability had not been previously observed in the field. Although the dominant nutrient-regulating process appeared to be advective porewater flow at the Coarse Site, regenerated nutrient inventories were also influenced by post-remineralization nutrient-regulating processes such as denitrification and P sorption/desorption. Conversely, no statistical difference in nutrient concentrations with sand-ripple location was observed at the Fine Site. These results suggest that the dominant nutrient-

173

regulating process in the upper sediment at the Coarse Site is advective porewater circulation, and other nutrient-regulating processes (e.g., organic matter deposition, bioturbation, oscillating redox conditions, benthic photosynthesis/respiration) control nutrient distribution at the Fine Site.

With the biogeochemistry of permeable sediment environments tightly coupled with enhanced transport between the porewater and the overlying bottom water, one of the current methodological challenges in working with permeable sediments is making *in-situ* porewater transport measurements without disrupting the hydrodynamics of the sediment. In this dissertation, the rate of vertical porewater flow at the Fine and Medium Sites was estimated *in-situ* using transient heat as a natural tracer. A method was developed using a statistical solution to the 1-D heat transport model to estimate vertical front velocities and effective thermal diffusivities from unfiltered temperature time series from an array of buried thermistors. Vertical porewater velocities were then obtained after applying known sediment thermal parameters. The method was successfully assessed using donated freshwater streambed datasets and a nearshore marine dataset collected at the Medium Site. Unlike previously developed temperature-based methods, the developed method uses unfiltered data, which allows for application of the method in environments with temperature signals comprised of multiple frequency components, such as in coastal marine sediments. Additionally, the use of unfiltered temperature data allowed for the calculation of porewater velocities during time periods when the dominant, usually diurnal, signal was weak.

The *in-situ* measurement of solute fluxes and remineralization rates in permeable sediments is also methodologically challenging. In this dissertation, porewater profiles and field-constrained transport rates were used in steady-state 1-D enhanced diffusion-reaction diagenetic

porewater models to calculate depth-dependent vertical fluxes for dissolved nutrients and carbon in permeable sediments at the Fine and Medium Sites. Profiles of depth-dependent solute production and consumption processes were then inversely calculated as the divergence or convergence of the solute fluxes. Resultant solute fluxes at the sediment water interface were found to agree reasonably well with other field-based permeable sediment flux measurements. Stoichiometrically predicted nutrient relationships were used to investigate potential geochemical processes responsible for the alteration of porewater nutrient inventories following organic matter remineralization. The stoichiometric models suggest the removal of the majority of regenerated dissolved nitrogen at the Medium Site, likely due to denitrification. Conversely, denitrification did not appear to be a significant nutrient-regulating process at the Fine Site. The majority of organic matter remineralized at the Fine Site was associated with biogenic silica, likely derived from planktonic diatoms. At the Medium Site, in contrast, it was estimated that only a third of the organic matter being remineralized was associated with biogenic silica.

The weak or non-existent relationships between hydrodynamic parameters and porewater transport measured in this dissertation, consistent with previous findings in permeable sediment environments (Hebert et al. 2007; Burdige et al. 2008), indicate that we do not fully understand all mechanisms driving advective flows in these environments. Unquantified, larger-scale circulation processes (e.g., wave setup, tides, regional currents, groundwater flow, reef-framework scale flow, etc.) were suspected of playing a significant role in the observed nutrient and redox structure at depth at the Medium Site, and are expected to influence nutrient and carbon cycling in these sediments.

Results presented in this dissertation highlight the complicated dynamics of permeable sediment environments in which carbon and nutrient distributions are driven by advective flows

175

and are altered by biogeochemical processes post-remineralization. Vertical and horizontal distributions of dissolved constituents appear to result from the interplay between biogeochemical processes and hydrodynamic conditions that vary on different spatial and temporal scales. As a result, extensive field-based measurements are needed to isolate the relative influence of individual nutrient-regulating processes in different permeable sediment environments. Field-based measurements can then be incorporated into diagenetic models to better constrain the importance of permeable sediments in coastal and global nutrient and carbon budgets.

5.2 References

Burdige, D. J., R. C. Zimmerman, and X. Hu. 2008. Rates of carbonate dissolution in permeable sediments estimated from pore-water profiles: The role of sea grasses. Limnol. Oceanogr. **53**: 549–565. doi:10.4319/lo.2008.53.2.0549

Hebert, A. B., F. J. Sansone, and G. R. Pawlak. 2007. Tracer dispersal in sandy sediment porewater under enhanced physical forcing. Cont. Shelf Res. **27**: 2278–2287. doi:10.1016/j.csr.2007.05.016

Huettel, M., P. Berg, and J. E. Kostka. 2014. Benthic exchange and biogeochemical cycling in permeable sediments. Ann. Rev. Mar. Sci. **6**: 23–51. doi:10.1146/annurev-marine-051413-012706

Precht, E., U. Franke, L. Polerecky, and M. Huettel. 2004. Oxygen dynamics in permeable sediments with wave-driven pore water exchange. Limnol. Oceanogr. **49**: 693–705. doi:10.4319/lo.2004.49.3.0693

Appendix A Statistics for the Crest-Trough Experiments

Samples or inventories are grouped into crest or trough for each nutrient, and labeled according to sample depth or as the calculated vertical nutrient inventory (Inv.). Nutrient inventories are calculated per m^2; see Section 2.3.5 for nutrient inventory calculations. For bottom water (BW) samples, n = 3. CV = coefficient of variation; CV_C = CV for crest; CV_T = CV for trough; CV_C:CV_T representing the ratio of the relative variability between crests and troughs for each sample depth or the calculated nutrient inventory. Statistically significant p-values (p < 0.05) for crests versus troughs and their corresponding depth or inventory are in bold.

Site	Nutrient	Depth	Concentration						Variability	
			All (n = 20)		**Crests** (n = 10)		**Troughs** (n = 10)			
			Mean ± STD (µM)	CV (%)	Mean ± STD (µM)	CV_C (%)	Mean ± STD (µM)	CV_T (%)	$CV_C{:}CV_T$	*p-value*
Fine Site	Si	BW	2.63 ± 0.07	2.5	--	--	--	--	--	--
		3 cm	39.5 ± 12.0	30.4	45.3 ± 14.1	31.2	34.2 ± 6.78	19.8	1.6	0.051
		6 cm	32.9 ± 6.01	18.3	34.4 ± 8.08	23.5	31.5 ± 2.52	8	2.9	0.300
		9 cm	29.2 ± 4.54	12.1	28.3 ± 4.25	15.0	30.0 ± 2.60	8.7	1.7	0.294
		Inv.	1661 ± 313	18.9	1796 ± 372	21.9	1526 ± 168	11	2.0	0.051
	SRP	BW	0.20 ± 0.04	17.5	--	--	--	--	--	--
		3 cm	0.88 ± 0.25	28.3	0.94 ± 0.29	30.5	0.83 ± 0.21	25.5	1.2	0.382
		6 cm	0.86 ± 0.28	32.7	0.98 ± 0.33	33.3	0.74 ± 0.17	23.1	1.4	0.057
		9 cm	0.89 ± 0.22	24.5	0.80 ± 0.23	28.6	0.98 ± 0.17	17.4	1.6	0.054
		Inv.	42.0 ± 8.67	20.7	44.7 ± 9.16	21.6	39.2 ± 7.59	19.4	1.1	0.157
Coarse Site	Si	BW	1.5 ± 0.06	4.0	--	--	--	--	--	--
		5.5 cm	2.38 ± 1.93	81.1	0.79 ± 0.28	35.6	3.96 ± 1.47	37.2	1.0	**2.82E-06**
		11 cm	5.45 ± 2.87	52.6	4.03 ± 1.42	35.3	6.87 ± 3.29	47.9	0.7	**0.022**
		16 cm	5.84 ± 3.76	64.3	4.94 ± 2.18	44.1	6.74 ± 4.82	71.6	0.6	0.297
		Inv.	297.0 ± 154.0	51.8	200.1 ± 48.5	24.2	393.8 ± 163.9	41.6	0.6	**2.10E-03**
	SRP	BW	0.17 ± 0.03	19.3	--	--	--	--	--	--
		5.5 cm	0.66 ± 0.56	85.4	0.26 ± 0.33	128	1.05 ± 0.45	42.9	3.0	**2.96E-04**
		11 cm	1.11 ± 0.39	34.7	1.13 ± 0.42	37.4	1.09 ± 0.36	33.4	1.1	0.807
		16 cm	1.15 ± 0.66	57.1	1.07 ± 0.47	43.9	1.23 ± 0.82	66.8	0.7	0.600
		Inv.	64.4 ± 25.3	39.4	52.5 ± 18.9	36.1	76.3 ± 26.1	34.2	1.1	**0.032**
	NO_x	BW	0.24 ± 0.07	30.0	--	--	--	--	--	--
		5.5 cm	2.18 ± 2.58	118	0.83 ± 2.46	298	3.54 ± 1.97	55.5	5.4	**0.014**
		11 cm	3.94 ± 2.28	58.0	4.50 ± 0.76	16.9	3.37 ± 3.12	92.4	0.2	0.281
		16 cm	3.06 ± 2.32	76.0	2.97 ± 1.96	66.0	3.15 ± 2.75	87.3	0.8	0.869
		Inv.	211.7 ± 115.5	54.6	185.9 ± 102.7	55.3	237.4 ± 127.0	53.5	1.0	0.332

Appendix B Freshwater datasets

Freshwater datasets for individual temperature profiles (TPs) at Boyer and Nine Mile Creeks in 2009 and 2010. **Top panels:** sediment temperature-depth time series collected at indicated creek. Thermistors are vertically stacked and denoted as z1 thru z5 at burial depths of 5, 10, 15, 20, and 25 cm below the SWI. **Second and third panels:** time series of vertical front velocities (v) and effective thermal diffusivities (D) computed for 15 cm below the SWI using VFLUX2 program (VF, dashed line) and the statistical solution to the heat equation (HE, solid line). Errors for the statistical solution are indicated with shaded areas and represent 95% confidence intervals. **Bottom panels:** Comparison of time series of observed dT/dt and modeled dT/dt computed using the statistical solution (see Chapter 3), with the coefficient of determination (R^2). Freshwater datasets were provided by R.P. Gordon.

Boyer TP03

Boyer TP04

Boyer TP05

Boyer TP06

Boyer TP07

Boyer TP08

Boyer TP09

Boyer TP10

Boyer TP11

Boyer TP12

Boyer TP13

Nine Mile 2009 TP04

Nine Mile 2009 TP05

Nine Mile 2009 TP08

Nine Mile 2009 TP09

Nine Mile 2009 TP10

Nine Mile 2010 TP01

Nine Mile 2010 TP02

Nine Mile 2010 TP03

Nine Mile 2010 TP04

Nine Mile 2010 TP05

Nine Mile 2010 TP06

Nine Mile 2010 TP07

Nine Mile 2010 TP08

Nine Mile 2010 TP09

Nine Mile 2010 TP10

Nine Mile 2010 TP11

Nine Mile 2010 TP12